

**Use of Parametric Finite Element Models to Investigate Effects of Occupant
Characteristics on Lower-Extremity Injuries in Frontal Crashes**

by

Katelyn Frances Klein

A dissertation submitted in partial fulfillment
of the requirements for the degree of
Doctor of Philosophy
(Biomedical Engineering)
in the University of Michigan
2015

Doctoral Committee:

Research Associate Professor Jonathan D. Rupp, Co-Chair
Research Professor Lawrence W. Schneider, Co-Chair
Research Professor James A. Ashton-Miller
Associate Research Scientist Jingwen Hu
Professor Gregory M. Hulbert
Professor Karl J. Jepsen

Acknowledgements

I would first like thank my advisor, Dr. Jonathan Rupp, for his mentorship and support over the past five years. I am forever grateful for all the comments and suggestions on improving my abilities as a researcher. I would also like to thank my Co-Chair, Dr. Larry Schneider for his guidance and input. In addition, I want to thank my committee members, Dr. Jingwen Hu, Dr. James Ashton-Miller, Dr. Gregory Hulbert, and Dr. Karl Jepsen, for their input as it has improved the quality and application of this dissertation.

I would like to acknowledge the assistance of all members of UMTRI's Biosciences group, particularly Dr. Jingwen Hu and Dr. Matthew Reed, as their help has been incredibly useful through all phases of this work. In addition, I want to sincerely thank Daniel, Lauren, Jangwoon, Eunjoo, and Kyle (of the 5+1) for all of the great conversations, support, and fun lunches that helped me survive the last part of the dissertation writing process. I also want to thank all of the students who helped with the countless hours of digitizing geometry.

Finally I want to thank my family and friends for all of their support and love. The visits and video chats will always be remembered. To Mom, Dad, Amanda, and Trevor, I could not have made it through this process without you.

The work reported in this thesis was funded by the National Highway Traffic Safety Administration under contract DTNH22-10-H-00288 and the National Science Foundation under award number 1300815.

Table of Contents

Acknowledgements	ii
List of Figures.....	v
List of Tables	ix
List of Appendices.....	xi
Abstract.....	xii
Chapter I Introduction	1
The Lower-Extremity Injury Problem in Frontal Crashes	1
Previous Research on the Effects of Occupant Characteristics on the Occurrence of Lower-Extremity Injuries in Frontal Crashes	2
Approaches to Characterizing the Influence of Occupant Characteristics on Lower-Extremity Injury in Frontal Crashes	6
Previous Efforts to Develop Human Finite Element Models with Varying Geometry	7
The Need for a New Parametric Finite Element Model	14
Research Objectives.....	14
Research Overview	14
Chapter II Development and Validation of the Statistical Models	17
Introduction.....	17
Methods Overview	17
Femur Model Methods.....	19
Femur Model Results	28

Tibia Model Methods.....	36
Tibia Model Results	40
Pelvis Model Methods	43
Pelvis Model Results.....	46
Discussion.....	49
Chapter III Development and Validation of the Parametric Finite Element Models	54
Introduction.....	54
Methods.....	55
Results.....	59
Discussion.....	62
Chapter IV Application of the Parametric Whole-body Models.....	65
Introduction.....	65
Methods.....	65
Results.....	78
Discussion.....	92
Chapter V Summary and Discussion	97
Summary.....	97
Limitations	99
Benefits of Parametric Models.....	104
Future Work	108
Chapter VI Conclusions	111
Appendices.....	112
References	134

List of Figures

Figure 1-1. Lower extremities region definitions.	2
Figure 1-2. Risk of AIS 3+ LX injuries in frontal crashes for males and females with increasing BMI (a) and increasing age (b) adjusted to account for the of effects other significant predictors.....	3
Figure 1-3. Flowchart for development, validation and application of the parametric FE lower-extremity and whole-body models.	16
Figure 2-1. Flowchart for the steps used to develop the statistical femur, tibia, and pelvis geometry models.....	19
Figure 2-2. Distributions of subject characteristics for the femur data.....	20
Figure 2-3. The fifty-nine landmark locations on the femur.	21
Figure 2-4. Example of the morphing and fitting processes for a template femur FE mesh onto an extracted bone surface geometry.....	22
Figure 2-5. Cortical thickness calculation algorithm.....	23
Figure 2-6. Femur length defined as the distance along the long axis of the femur (determined from anatomic landmark locations in the landmarking process) between the most superior point on the femoral head and most inferior point on the femoral condyles.	26
Figure 2-7. The five area locations (1-5) along the shaft of the femur and the one neck location (0) used for area measurements and the definitions of total bone area and cortical bone area.	28
Figure 2-8. The effects of age, BMI, femur length, and gender on femur geometry predicted by the parametric models.	30

Figure 2-9. Distribution of mean and 95th percentile absolute errors in nodal coordinate locations (left two columns) and cortical thickness values at nodal locations (right two columns) between the actual femur data and predicted geometries.	31
Figure 2-10. Cortical bone cross-sectional areas at five locations along the shafts of the PMHS femurs and the errors in the predicted shaft cross-sectional areas.	32
Figure 2-11. Midshaft cross-sectional areas of the 13 PMHS femurs and the predicted femur models.	33
Figure 2-12. Distribution of femur cross-sectional areas by sex and location level.	33
Figure 2-13. Distributions of subject characteristics for the tibia data.	37
Figure 2-14. The seventy-six landmark locations on the tibia.	38
Figure 2-15. Tibia length defined as the Euclidean distance the most anterior point on the tibial tuberosity and the most inferior point on the medial malleolus.	39
Figure 2-16. The effects of age, BMI, tibia length, and gender on tibia geometry predicted by the parametric models.	42
Figure 2-17. Distribution of mean and 95th percentile absolute errors in nodal coordinate locations (left two columns) and cortical thickness values at nodal locations (right two columns) between the actual tibia data and predicted geometries.	43
Figure 2-18. Distributions of subject characteristics for the pelvis data.	44
Figure 2-19. The locations of the forty-seven landmarks on the pelvis.	45
Figure 2-20. Bispinous breadth defined as the distance between the anterior superior iliac spines on the left and right side of the pelvis.	46
Figure 2-21. The effects of age, BMI, bispinous breadth, and gender on pelvis geometry predicted by the parametric models.	47
Figure 2-22. Distribution of mean and 95th percentile absolute errors in nodal coordinate locations between the actual pelvis data and predicted geometries.	48
Figure 2-23. Example of the comparison between observed and predicted landmarks for a single subject from a separate set of data.	49
Figure 3-1. Ivarsson et al. (Ivarsson et al. 2009) test set-up with combined bending and axial compression due to the impactor and moving gussets.	57
Figure 3-2. Example of impactor force history from an experimental result compared to impactor force results from a simulation with the parametric model.	60

Figure 3-3. Comparison between the peak impactor forces (left) and slope values (right) for the experimental values and values predicted by the parametric models.	61
Figure 4-1. Flowchart of the process for developing a whole-body model with target geometry and material properties from statistical geometry and material models and a template mesh.	67
Figure 4-2. Femur length defined as the Euclidean distance between the center of the femoral head and the midpoint of the femoral epicondyles.....	68
Figure 4-3. Examples of small, midsize, and large male body surface shapes predicted by the external body surface shape model.	69
Figure 4-4. Femur and tibia length determined from landmark locations predicted by the external body surface shape model.	69
Figure 4-5. Landmarks used to position the pelvis, femur, and tibia.....	70
Figure 4-6. Example of process for positioning the predicted bones inside the external surface using SVD.	70
Figure 4-7. Morphed trabecular bone inside the right femur.....	71
Figure 4-8. Three segments for right leg.	71
Figure 4-9. An example of the morphed whole-body model.....	72
Figure 4-10. Female and male morphed whole-body model examples.	72
Figure 4-11. Simulation set-up.	74
Figure 4-12. Seatbelt fit determined from ASIS landmark.	76
Figure 4-13. Seatbelt fit determined from ASIS landmarks and thorax landmark.	77
Figure 4-14. Distributions of normalized strains for the right femur with BMI (top left), the pelvis with age (top right), the left femur with BMI (bottom left), and the left femur with age (bottom right).	82
Figure 4-15a. Change in distributions of principal strain with BMI for the right femur..	83
Figure 4-15b. Change in distributions of principal strain with BMI for the left femur....	83
Figure 4-15c. Change in distributions of principal strain with age for the left femur.....	84
Figure 4-15d. Change in distributions of principal strain with age for the pelvis.....	84
Figure 4-16. Distributions of forces for the male simulations.....	86
Figure 4-17. Distributions of normalized strains for the right tibia with BMI (top left), the left tibia with stature (top right), and the left femur with age (bottom left).....	88

Figure 4-18a. Change in distributions of principal strain with BMI for the right tibia....	88
Figure 4-18b. Change in distributions of principal strain with stature for the left tibia...	89
Figure 4-18c. Change in distributions of principal strain with age for the left femur.....	89
Figure 4-19. Distributions of forces for the female simulations.....	91
Figure 4-20. The effects of age on femur geometry predicted by the male femur models.....	93
Figure 5-1. Distributions of percent differences between peak impactor forces (left) and slopes (right) for the experimentally measured test results and the values for parametric, scaled, midsize, specimen-specific, and yield stress fit results.....	106
Figure D-1. Impactor force histories for the parametric model simulations compared to the experimentally measured results.....	120
Figure H-2. Time histories of impactor forces for the parametric model simulations, scaled THUMS 4, midsize THUMS 4, specimen-specific, and specimen-specific with yield stress fit simulations compared to the experimentally measured test results.....	133

List of Tables

Table 1-1. An overview of recent human whole-body FE models, their sizes, and their LX applications	12
Table 2-1. <i>p</i> -values of predictors in the female and male femur external geometry models	29
Table 2-2. <i>p</i> -values of predictors in the female and male femur thickness models	29
Table 2-3. Cortical cross-sectional bone area model data	35
Table 2-4. Total cross-sectional bone area model data	35
Table 2-5. Significance levels of predictors in the cortical bone mixed models	36
Table 2-6. Significance levels of predictors in the total bone mixed models	36
Table 2-7. <i>p</i> -values of predictors in the female and male tibia external geometry models	40
Table 2-8. <i>p</i> -values of predictors in the female and male tibia thickness models	41
Table 2-9. <i>p</i> -values of predictors in the female and male external geometry models	47
Table 3-1. Linear mixed models analysis results for male experimental and model predicted results	61
Table 4-1. Subject characteristics used for simulations	74
Table 4-2. Female mesh quality results after the morphing process	79
Table 4-3. Male mesh quality after the morphing process	80
Table 4-4. Male model normalized strain results	81
Table 4-5. Coefficient values for each parameter for the male linear multivariate regression equations determined for the right femur, left femur, and pelvis	81
Table 4-6. Male model force results	85
Table 4-7. Female model normalized strain results	87

Table 4-8. Coefficient values for each parameter for the female linear multivariate regression equations determined for the right tibia, left tibia, and left femur	87
Table 4-9. Female model force results.....	90
Table B-1. Subject characteristics from Ivarsson et al. (2009) data	114
Table C-2. Percent differences between impactor forces for experimentally measured and parametric simulations at time of failure	115
Table C-3. Percent differences between slope values for experimentally measured and parametric simulations from time of contact until time of failure	116
Table E-4. Examples of male morphed models	121
Table E-5. Examples of female morphed models	123
Table F-6. List of subject characteristics	125
Table G-7. Percent differences between peak impactor forces for experimentally measured test results and parametric, scaled, midsize, specimen-specific, and specimen-specific with yield stress fit femur simulations at time of failure.....	126
Table G-8. Absolute percent differences between peak impactor forces for experimentally measured test results and parametric, scaled, midsize, specimen-specific, and specimen-specific with yield stress fit femur simulations at time of failure.....	127
Table G-9. Percent differences between slope values for experimentally measured test results and parametric, scaled, midsize, specimen-specific, and specimen-specific with yield stress fit femur simulations from time of contact until time of failure	128
Table G-10. Absolute percent differences between slope values for experimentally measured test results and parametric, scaled, midsize, specimen-specific, and specimen-specific with yield stress fit femur simulations from time of contact until time of failure	129

List of Appendices

Appendix A.....	112
Appendix B.....	114
Appendix C.....	115
Appendix D.....	117
Appendix E.....	121
Appendix F.....	125
Appendix G.....	126
Appendix H.....	130

Abstract

The lower extremities are the most frequently injured body region in frontal crashes, accounting for 36% of all injuries associated with a moderate and greater threat-to-life sustained by front-seat occupants (Kuppa and Fessahaie 2003). To explore the biomechanical reasons for the effects of age, sex, and body mass index (BMI) on lower-extremity (LX) injuries in frontal crashes, parametric FE models are needed. Male and female finite element (FE) models that have skeletal geometry, external body shape, and seated posture that are parametric with occupant characteristics were developed and validated. These parametric models are based on statistical models that predict LX geometry and material properties as functions of occupant characteristics and used mesh morphing techniques to morph a template whole-body model.

Statistical models of femur, tibia, and pelvis surface geometry and femur and tibia cross-sectional geometry were developed by (1) morphing and fitting template FE meshes onto bone geometries extracted from CT data, (2) applying principal component analysis to the resulting nodal coordinates and then (3) performing regression on principal component (PC) scores to develop models that describe how these scores, and in turn, lower-extremity geometry, vary with occupant age, stature, and BMI. Because each statistical model is based on a template mesh, the geometries predicted by these models are the nodal coordinates of a FE mesh.

FE models of the femur, tibia, and pelvis that have mesh geometry that is parametric with occupant characteristics were developed by linking the statistical models to meshes of similar bones from a baseline FE human model from Toyota's THUMS 4 model. The parametric FE femur models were validated by simulating combined compression and

bending tests of the femoral shaft from a previous study and comparing impactor force histories from the experiments to simulation results. Impactor forces from simulations, on average, matched well to experimental values at the time of failure with an average error of 5% across the 25 validation simulations. In addition, the simulations were able to match the trends seen in the experimental dataset. This was determined by fitting the same statistical model to the experimental and simulation data and comparing model predictions. The femur tests were used for validation because sufficient information was available to effectively characterize specimen geometry and because the applied force histories were available for all tests. Datasets with a similar level of detail on geometry, response, and specimen demographics are not available for the tibia, pelvis, and whole lower extremities. Therefore, validation of the parametric model could not be performed for these components.

Parametric FE whole-body models were developed using the parametric FE pelvis, femur, and tibia models with an external body surface shape model previously developed at UMTRI that predicts shape using age, sex, BMI, and stature. The pelvis, femur, and tibia models were positioned inside the external surface model using landmarks predicted by the external body surface shape model. The bone models and the external surface model were used to morph a template whole-body FE mesh to develop the whole-body models. Frontal-crash simulations of drivers of different sexes, ages, statures, and BMIs were performed with the whole-body models to begin assessing the relative contributions of age, sex, and BMI on the risk of LX injury. Results of these simulations are generally consistent with field data and indicate that increases in age and BMI cause increases in strains and forces in the lower extremities. These results agree with the hypotheses that elderly and higher BMI occupants are at increased risk for lower-extremity injuries. In addition, the results indicated that women have higher strain values in the right femur, right tibia, and pelvis than men, agreeing with the hypothesis that women are at increased risk for LX injury. However the effects appear to differ between left and right sides of the body, likely because of asymmetric lower-extremity posture.

Chapter I

Introduction

THE LOWER-EXTREMITY INJURY PROBLEM IN FRONTAL CRASHES

Over the past decades the numbers of fatalities and severe injuries to the head, thorax, and abdomen in frontal motor-vehicle crashes have decreased due to significant increases in seatbelt usage and frontal-impact airbags in passenger vehicles, as well as improvements to vehicle structures. Although rates of lower-extremity (LX) injuries have also decreased, the rates of their decrease have been disproportionately lower than those of other body regions (Moran et al. 2003). As a result, the lower extremities are now the most frequently injured body region in frontal crashes, accounting for 36% of all Abbreviated Injury Scale (AIS) 2+ injuries (i.e., injuries associated with a moderate and higher threat-to-life) sustained by front-seat occupants (Kuppa and Fessahaie 2003).

As shown in Figure 1-1, the lower extremities are commonly divided into the three regions of 1) the knee-thigh-hip (KTH), where the hip includes the pelvic bone, 2) the leg, and 3) the foot-ankle. LX soft-tissue injuries in motor-vehicle crashes are almost always associated with LX skeletal fractures; therefore, LX injury prevention efforts have focused on preventing skeletal injuries (Varellis et al. 2004). About half of all LX injuries are to the KTH complex and the other half is to the leg and foot-ankle complex (Kuppa and Fessahaie 2003).

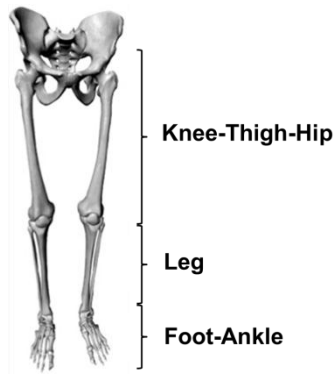


Figure 1-1. Lower extremities region definitions.

LX injuries often significantly impact the lives of patients, their families, and society in general. These impacts are manifested in reduced mobility which may limit or prevent return to work, affect behavioral functioning, and require rehabilitative efforts for treatment (Scarboro et al. 2005). Psychosocial factors such as depression can impede recovery. In addition, pain, decreased mobility, and increased dependence may affect lifestyle and the ability to return to baseline functioning.

LX injuries can also be costly for patients and their families due to hospital, professional, and rehabilitation costs associated with the injuries (Read et al. 2004). The average annual comprehensive cost of LX injuries for airbag-equipped vehicles has been estimated using the nonfatal injury unit cost based on the year 2000 dollar value in Economic Impact of Motor Vehicles Crashes (Blincoe et al. 2002). The comprehensive cost includes the economic cost as well as an estimated cost of pain and suffering and loss in quality of life. The total annual cost of LX injuries is \$7.6 billion (Kuppa and Fessahaie 2003).

PREVIOUS RESEARCH ON THE EFFECTS OF OCCUPANT CHARACTERISTICS ON THE OCCURRENCE OF LOWER-EXTREMITY INJURIES IN FRONTAL CRASHES

Analyses of crash-injury databases, such as the probability sample of crashes contained in the National Automotive Sampling System-Crashworthiness Data System (NASS-CDS),

demonstrate that occupant characteristics, including age, sex, and body mass index (BMI), affect the risk of AIS 3+ LX injuries in frontal motor-vehicle crashes (Carter et al. 2014; Moran et al. 2003; Ridella et al. 2012; Rupp and Flannagan 2011). Lower-extremity AIS 3+ injuries include a displaced or comminuted fracture of the pelvis, tibia, or patella and any fracture of the femur. Crash-injury database analyses have found that, when controlling for the effects of other significant predictors like crash severity and seatbelt use, the risk of AIS 3+ LX injuries in frontal crashes increases with age, is higher for women than men, and increases with increasing BMI. Figures 1-2a and 1-2b show plots of statistical models developed by Rupp and Flannagan (2011) that illustrate the effects of age and BMI on LX injuries for men and women in frontal crashes with severities similar to those produced in regulatory compliance tests conducted by the National Highway Traffic Safety Administration (NHTSA).

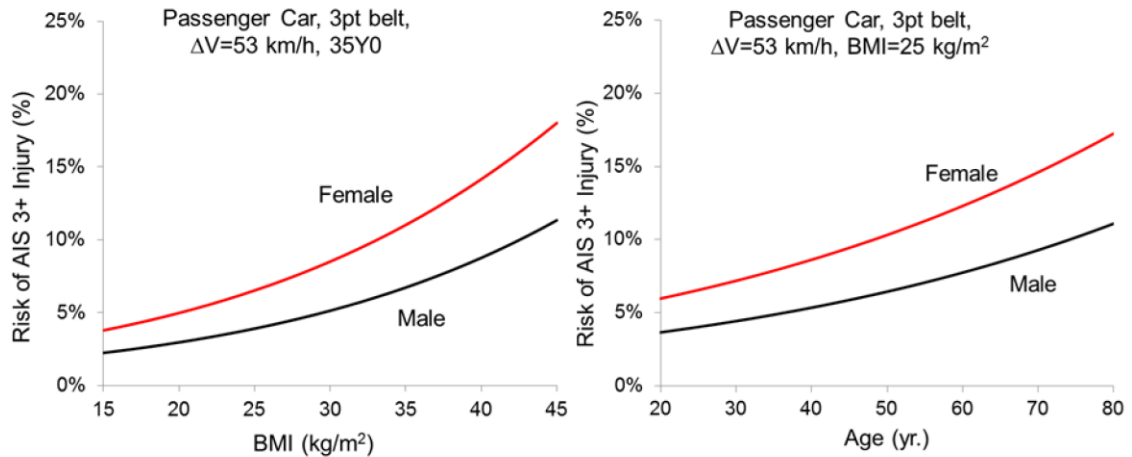


Figure 1-2. Risk of AIS 3+ LX injuries in frontal crashes for males and females with increasing BMI (a) and increasing age (b) adjusted to account for the effects of other significant predictors.

Analyses of NASS-CDS and outcome-sampled databases, such as the Crash Injury Research and Engineering Network database, suggest that the effects of age, BMI, and sex on LX injuries are different for different parts of the lower extremities. Rupp and Flannagan (2011) found that age has larger effects for injuries to the KTH complex than for the foot-ankle. Crash-investigation studies have also found that women sustain more foot-ankle injuries than men and that men sustain more knee-thigh-hip injuries than

women (Chong et al. 2007; Dischinger et al. 1995; Rudd 2009; Wang et al. 2004). However, there is disagreement as to whether these differences are caused by differences in stature or sex, with shorter people (mostly women) sustaining more foot-ankle injuries and taller people (mostly men) sustaining more KTH injuries.

Multiple biomechanical explanations for the age, BMI, and sex effects on LX injury risk have been hypothesized. Based on the results of computational modeling, Turkovich (2010) hypothesized that the increase in LX injury risk with BMI is caused by increased forward excursion of the knees for higher BMI occupants caused by increased amounts of adipose tissue over the anterior superior iliac spines (ASIS), which are the parts of the pelvis that the vehicle lap-belt restraint is intended to load in a frontal crash. This finding is confirmed by a limited number of frontal-crash tests performed with obese and non-obese cadavers, in which the hips and knees of obese cadavers moved further forward than non-obese cadavers (Kent et al. 2010). In addition, the increase in mass with a larger BMI may also cause the increase the impact force.

In addition to increasing BMI increasing the amounts of adipose tissue over the ASIS, higher BMI has also been associated with lap-belt positions that are farther above the ASIS (Reed et al. 2012). Such belt positions are likely to prevent the lap belt from applying effective restraint forces to the pelvis in a frontal crash and thereby increase the forward movement of the knees as well as the forces applied to the knees as a result of knee bolster impact (Reed et al. 2012). These higher knee impact forces are associated with an increased likelihood of both KTH and below-knee injuries (Rupp et al. 2008).

The effects of BMI on the risk of LX injury may also be different for men than for women because of differences in body fat distribution with sex. Specifically, the tendencies for women to carry more fat in their hips and men to carry more fat in their abdomens, coupled with the hypothesized reasons for the BMI effect discussed above, suggest that the BMI effect may be more pronounced for men than for women.

Differences in LX injury risk and injury patterns with occupant sex may also be caused by differences in the size and shape of LX bones between men and women. Men have a larger bone size, on average, than women, consistent with their larger body size (Riggs et al. 2004). Bone shape also differs between men and women. For example, the differences in pelvic-bone anatomy and shape between men and women could explain differences in the risk of some LX injuries. In a study of pelvic CT scans, Wang et al. (2004) found that the female acetabulum (hip socket) tends to face more forward and thereby engage a greater proportion of the surface area of the femoral head in a given posture during frontal-impact loading through the KTH complex than the male acetabulum. This factor could make the male hip joint more susceptible to injury during a frontal crash, while the higher-tolerance female hip joint may increase the possibility of a knee or thigh injury (Wang et al. 2004).

Differences in male and female seated position and posture when driving a motor vehicle may also explain the differences in LX injury risk. For example, women drivers are more likely than men to drive with the seat moved forward, and men tend to sit with more leg splay (i.e., angled outward) than women (Schneider et al. 1983 and Reed 1998). These differences in position and posture could affect LX injuries during frontal crashes because of differences in the direction of KTH loading and the pre-impact distance between the knees and the knee bolster.

Changes in cortical bone material properties and bone cross-sectional geometry with age and sex also contribute to the effects of occupant characteristics on LX injuries. Age affects bone material properties and cross-sectional geometry such that increasing age results in decreasing bone mineral density and the thickness of cortical bone (Kent et al. 2005). In addition, the fracture toughness of cortical bone decreases with aging due to changes in the microstructure of bone (Nalla et al. 2004). These changes in bone material properties and geometry with age decrease the amount of force necessary to fracture a bone, which increases the risk for LX injuries with increasing age (Beason et al. 2003; Moran et al. 2003). Occupant sex also has an effect on changes in bone material properties and geometry in that older women have increased bone porosity and decreased

bone mineral density, and therefore a greater fracture risk than older men (Riggs et al. 2004).

APPROACHES TO CHARACTERIZING THE INFLUENCE OF OCCUPANT CHARACTERISTICS ON LOWER-EXTREMITY INJURY IN FRONTAL CRASHES

Developing vehicle restraint systems that will reduce the risk of LX injuries for the elderly, women, and high-BMI occupants requires an understanding of the biomechanical factors that explain how and why age, sex, and BMI affect the likelihood, location, and severity of LX injuries in frontal crashes. Approaches used to consider the effects of occupant characteristics on injury in crashes during the development and/or evaluation of new restraint technologies include physical testing with anthropomorphic test devices (ATDs) or crash test dummies of different sizes, impact testing with cadavers, and/or simulations with finite element (FE) models of humans and ATDs (e.g., Kent et al. 2003; Kimpara et al. 2010; Loyd et al. 2012).

Testing with ATDs involves physically reconstructing frontal crashes using the three available sizes of adult crash test dummies, including the midsize male (approximately 50th percentile in both stature and weight), the small female (approximately 5th percentile in both stature and weight), and the large male (approximately 95th percentile in both stature and weight based on 1974 U.S. census data) and weighting these tests so that results from each represent segments of the crash-involved population. However, testing with ATDs is inadequate to study the effects of occupant sex, age, and BMI because current ATDs do not accurately represent most of the factors that can affect LX injury risk, such as variability in skeletal geometry, compressible soft tissue over the pelvis and abdomen, bone material properties, and body shape and posture.

Frontal-impact testing with human cadavers of varying age, sex, and BMI could be used to characterize age, sex, and BMI effects on LX injury. However, a large number of cadavers and tests would be required to appropriately estimate the effects associated with

age, sex, and BMI on LX injuries. Further, obtaining suitable cadavers and cadaveric material would be difficult because almost all cadavers available for injury biomechanics research are elderly and often have multiple co-morbid conditions. As a result, the available cadavers do not appropriately represent the younger (and living) crash-involved population.

Finite element modeling, however, has the potential to study the effects associated with occupant age, sex, and BMI on LX injuries at a reasonable cost. In particular, simulations with a set of validated computational human FE models with geometry and material characteristics that appropriately represent the distributions of age, sex, and BMI in the adult occupant population could be used to identify the biomechanical basis for the effects of occupant characteristics on LX injuries. However, such a set of validated FE models is not currently available.

PREVIOUS EFFORTS TO DEVELOP HUMAN FINITE ELEMENT MODELS WITH VARYING GEOMETRY

Previous whole body and lower-extremity component FE models only represent an occupant who is midsize in stature and weight or an occupant who is the same size as adult crash test dummies (Iwamoto et al. 2002; Kim et al. 2005; Robin 2001; Ruan et al. 2008; Silvestri and Ray 2009; Torigian 2011; van Rooij et al. 2004; Vavalle et al. 2014). Almost all FE models of adults have the same size and shape specifications as adult crash test dummies (i.e. the midsize male, small female, and large male) because of the desire to compare predictions between human FE models and crash test dummy models (Hu et al. 2012). As a result, these FE models are limited in the same way that adult crash test dummies are limited. The models are not able to capture the variability in body size and shape with occupant characteristics at a level that is sufficient to isolate the effects of these parameters on LX injury.

One approach to investigating the effects of occupant characteristics on injury involves performing simulations with validated finite element models with occupant geometry that

has been modified using simple linear scaling either with a single scale factor or different scale factors for different axes (Kimpara et al. 2005). However, such methods are limited by the linearity assumptions and the limited data on which scale factors are based (Hu et al. 2012). Specifically, most scaling methods are based on a ratio of single length values, with stature being the most common. Such an approach may be inappropriate if shape varies with size or other characteristics, such as BMI and age. However, the effects of this assumption on model predictions have not been well characterized. Further, linear scaling on either a whole body or a regional level is likely to result in models that do not accurately represent the geometry of portions of the population that are most vulnerable (e.g., osteoporotic women with thinner cortical bone relative to younger women).

Some FE models have been developed that have bones with parametric geometry to use primarily for exploring the effects of patient-specific skeletal geometry on surgical planning, implant biomechanics, and to predict the risk of femur fracture in falls. These models use patient images such as CT scans to determine geometry of relevant anatomy, which allows inter-subject variability in bone geometry and bone quality to be taken into account in pre-surgery planning (Bryan et al. 2009). However, the bone models are limited in application because they are patient-specific and used for implant biomechanics instead of injury biomechanics. In addition, these models are parameterized with variables such as femur dimensions, and not parameterized with subject characteristics, such as BMI, that are known to be important for vehicle crash safety assessment, and do not cover the needed range of population characteristics since the studies primarily focus on the older population that needs implants (Bryan et al. 2010; Bryan et al. 2009; Kurazume et al. 2009; Nicolella and Bredbenner 2012).

Human FE models with detailed skeletal geometry, external body surface geometry, and soft tissue geometry that are parametric with subject descriptors, such as stature, have been developed to incorporate population variability into crash simulations and overcome the limitations associated with traditional scaling methods. These models are made parametric through linkages to statistical models that predict the locations of landmarks on bones as functions of subject descriptors. Landmark-based mesh morphing techniques

such as Kriging or radial basis functions are used to morph FE meshes to fit the predicted landmark locations while maintaining mesh quality (Hu et al. 2012).

A body region FE model with geometry that is parametric with occupant characteristics has been developed for the ribcage. Gayzik et al. (2008) developed a statistical model that characterizes age-related changes in human rib shape using Procrustes alignment and regression analysis. Generalized Procrustes Analysis or Procrustes alignment is a method used to study shape differences in populations and can be applied to landmark-based data to reduce the complexity of the overall structure while still reflecting the shape variation. Landmark locations on the ribcage were extracted from CT scans to describe the form of each ribcage. Generalized Procrustes Analysis was used to analyze the shape differences between subjects, and regression analysis was used to determine predictive models of landmark location as a function of age. These models were linked to a template FE model and used in simulations to demonstrate that age affected thoracic response.

Another body region FE model with geometry that is parametric with occupant characteristics has been developed for the pediatric head. Li et al. (2011) developed a statistical model to characterize the effects of cranium geometry and material properties on pediatric head impact response for use in development of a pediatric head FE model. Landmark locations were extracted from CT scans of pediatric craniums, and a combination of principal component analysis (PCA) and regression analysis was used to develop a statistical model characterizing changes in cranium geometry with age for 0-3-month-old children. PCA is a statistical technique used for data compression and organization in many research fields, such as facial feature recognition, ergonomics, and crash dummy design (Reed and Parkinson 2008). The dimensionality of a data set consisting of a large number of interrelated variables can be reduced while retaining as much as possible of the variation present in the data set (Jolliffe 2002). Radial basis functions (RBFs) were used to morph the geometry of a baseline child head FE model into models with geometries representing 0-3-month-old heads. RBFs are widely used in diverse fields, including image processing, meteorology, and medical MRI data operation for morphing data and include several function options such as equations based on thin

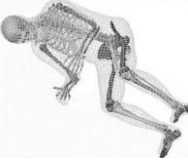
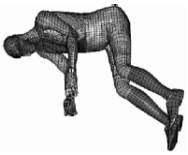



plate splines (Carr et al. 2001 and Bennink et al. 2007). The morphed FE models were validated and demonstrated that the statistical model of cranium geometry produced realistic cranium size and shape and had mesh quality comparable to the baseline model.

A few other parametric models have been developed for the pelvis, liver, clavicle, and ribcage (Besnault et al. 1998; Gayzik et al. 2008; Lu et al. 2013; Lu and Untaroiu 2013). Shi et al. (2014) developed a statistical ribcage geometry model accounting for variations in age, sex, stature, and BMI that can serve as a geometric basis for developing a parametric human thorax finite element model for quantifying effects from different human attributes on thoracic injury risks. In addition, Shi et al. (2015) developed a whole-body FE model with external surface geometry and ribcage skeletal geometry that could be simultaneously varied with BMI based on the predictions of statistical geometry models and used this model to explore how obesity affects occupant responses in frontal crashes.

Most current whole-body FE models are not parametric. Table 1-1 lists some of the more recent available human whole-body FE models, the sizes they represent, and their LX applications. The H-model is an older FE model that only represents a 50th percentile male and 5th percentile female. The THUMS model was first developed in 2002 and has been updated with newer versions to represent a 5th percentile female and a 50th and 95th percentile male in seated and standing postures. Ford Motor Company developed a FE model that only represents a 50th percentile male to study whole-body responses in frontal and side impacts. Wayne State University developed a whole-body model based on their body region component models, but the model only represents a 50th percentile male and uses a dummy model's lower extremities for limited LX applications. The Global Human Body Models Consortium (GHBMC) was formed in 2006 "to consolidate individual research and development activities in human body modeling into a single global effort to advance crash safety technology" and the model is now available for free academic use (Torigian 2011; Yaeger and Flores 2013). GHBMC has been morphed to represent a 95th percentile seated male, but a parametric version of GHBMC is not yet available (Vavalle et al. 2014).

The HUMOS2 project developed one of the first existing parametric whole-body FE models. This model is described in Table 1-1 and uses parametric anthropometry to scale a mid-size male FE model (Veizin and Verreist 2005). However, this specific model has some limitations. The HUMOS2 is based only on a small number of whole-body skeletal landmark locations from mostly young, non-obese subjects and does not capture variability in cross-sectional geometry. This model and all other subject-specific models do not consider variability in external body geometry with occupant characteristics, which is important to study when modeling high-BMI occupants and may be important in studying older occupant response. These subject-specific models are still limited in their applications, and they do not account for cross-sectional geometry and material property changes in the population.

Table 1-1. An overview of recent human whole-body FE models, their sizes, and their LX applications

First Author/Year	Choi 1999	Iwamoto 2002	Ruan 2003	Shah 2004	Formed in 2006	Veizin 2007
Model Name	H-model	Total Human Model for Safety (THUMS), Version 4-2010	Ford Human Body Finite Element Model	WSU Whole-body Human Finite Element Model	Global Human Body Models Consortium (GHBMC)	Human Model for Safety 2 (HUMOS2)
Software	PAM-CRASH	LS-DYNA	LS-DYNA	LS-DYNA	LS-DYNA, PAM-CRASH, Radioss	Radioss, PAM-CRASH
Size	50 th %tile male and 5 th %tile female	5 th %tile female, 50 th %tile male, 95 th %tile male	50 th %tile male	50 th %tile male	5 th %tile and 50 th %tile female, 50 th %tile male, 95 th %tile male	5 th %tile female, 50 th %tile male, 95 th %tile male, scale to others
Posture	Seated	Seated and Standing	Seated	Seated	Seated and Standing	Seated and Standing
Figure						
Geometry	Visible Human Project	CT scans	Visible Human Project	Viewpoint Datalabs, Visible Human Project	MRI, UMRI, CT, External anthropometry	External anthropometry, X-Ray
Elements	Not stated	1.8 million elements	119,000 elements	126,536 elements	1.74 million elements	Not stated
Validation	Multiple tests for each body region	Multiple tests for each body region	Frontal and side pendulum impacts in various speeds, Belt loading, Frontal rigid bar impact	Chest left oblique pendulum impact, Chest frontal pendulum impact, Abdomen right oblique pendulum impact, Lower abdomen bar impact, Whole-body drop test, Mid-abdomen lap belt loading and surrogate airbag loading	Multiple tests for each body region	Frontal impact cadaver sled tests
LX Applications	Knee-hip and foot-ankle in frontal crashes	Pelvis and LX in frontal impact and pedestrian impacts	Pelvis and LX in frontal and side impacts	None- LX represented by Hybrid III LX	None so far	Pelvis and LX in side impact and pedestrian impacts

Conventional validation of human-body FE models is generally performed with midsize or scaled models with their results compared to response corridors determined from experiments with post-mortem human surrogates (PMHS). The goal is to obtain responses that fit within the bounds of corridors developed from the PMHS test data that are normalized to a reference size. This is the same approach used for validating anthropomorphic test devices (Maltese et al. 2002).

Previous parametric FE models of humans have either not been revalidated when their geometry is varied (i.e., it is assumed that if the model is valid at one size, age, and sex it is valid at all sizes and ages and for both sexes) or models are validated by comparing their predicted responses to corridors describing the variability in experimental responses that have been adjusted to represent target model size using mass-scaling techniques (e.g., Eppinger et al. 1984; Vavalle et al. 2014; Yoganandan et al. 2014). The primary reason for this latter approach is that experimental data on human impact response, geometry, and material properties that are needed to assess model fidelity over the ranges of ages and body sizes present in the adult vehicle occupant population are rare. For example, the only study with sufficient information for revalidation of a lower-extremity model is the work done by Ivarsson et al. (2009). However, mass-scaled corridors may not be appropriate for validation of models with parametric geometry because the underlying methodology assumes that members of the population have the same shape but different size as well as the same modulus of elasticity.

Hu et al. (2012) proposed a paradigm for parametric model validation in which well-validated baseline FE models are morphed to represent the geometries of whole post mortem human subjects (PMHS) or PMHS components from previous studies using reported information on the age, stature, BMI, and sex of the associated PMHS. Simulations are then performed with these parametric models using the corresponding loading conditions applied to each PMHS or component in the previous studies. The validity of the parametric model is then assessed by comparing individual model predictions to associated experimental responses and assessing how well the model matches responses across the entire dataset and how well the model matches any trends in

responses in the dataset. Material properties that are parametric with occupant characteristics may also be incorporated into the Hu et al. (2012) validation process.

THE NEED FOR A NEW PARAMETRIC FINITE ELEMENT MODEL

As indicated above, there are several hypothesized reasons for the effects of occupant characteristics on LX injury, including variations in LX skeletal geometry and material properties, pre-crash posture of the lower extremities, and body size, mass, and external shape with sex, age, and/or BMI. These variations affect LX injury occurrence and the directions and magnitudes of loading to the lower extremities in frontal crashes. The relative contributions of these hypothesized reasons for the effects of age, sex, and BMI on LX injury in frontal crashes can best be assessed using a parametric FE model. This FE model needs to have skeletal geometry, external surface geometry, posture, and material properties that are parametric with occupant characteristics. However, such a model does not currently exist.

RESEARCH OBJECTIVES

The objectives of this research were to investigate the effects of age, sex, and BMI on variations in LX geometry, material properties, body size, and body shape and to begin understanding the effects of these variations on lower-extremity injury risk. This was accomplished by developing, validating, and performing simulations with male and female human-body finite element models that have geometry and material properties that are parametric with, age, BMI, and stature.

RESEARCH OVERVIEW

The research project involves the four steps described below:

- (1) Extract LX skeletal geometries from CT scans of male and female patients with a wide range of ages, statures, and BMIs and perform statistical analyses of the CT data to develop models that describe the variance in skeletal geometry for the femur, tibia, and pelvis with subject characteristics.
- (2) Link the statistical models to a baseline FE mesh of the human occupant from Toyota's THUMS 4 model, resulting in a FE mesh with geometry and material properties that are parameterized with subject characteristics.
- (3) Validate the ability of the femur model (as an example of methods for all lower-extremity bones) to reproduce the responses of subjects with different geometry insofar as possible given the available data.
- (1) Perform frontal-crash simulations of drivers of different sexes, ages, statures, and BMIs to begin exploring the extent to which variations in LX geometry, material properties, body size, and body shape with sex, age, and BMI explain the observed effects of these parameters on LX injuries in frontal crashes.

Figure 1-3 outlines the methods for developing, validating, and using the parametric FE lower-extremity and whole-body models. These models rely on geometric information obtained from other models including a model that predicts driver body surface shape previously developed by UMTRI and statistical models describing how LX bone geometry varies with age, sex, stature, and BMI. The work to develop these bone geometry models is described in Chapter II and involves extracting LX skeletal geometries from a CT scan database and performing statistical analyses to develop the femur, tibia, and pelvis geometry models using mesh morphing and PCAR methods. The development of the parametric FE LX models and the validation of the FE femur model as an example of component level validation are described in Chapter III. The development of the whole-body parametric FE model by combining the component level models with the existing body surface shape model and the application of the whole-body model are described in Chapter IV. Chapters V and VI include discussion and conclusions of this research, respectively.

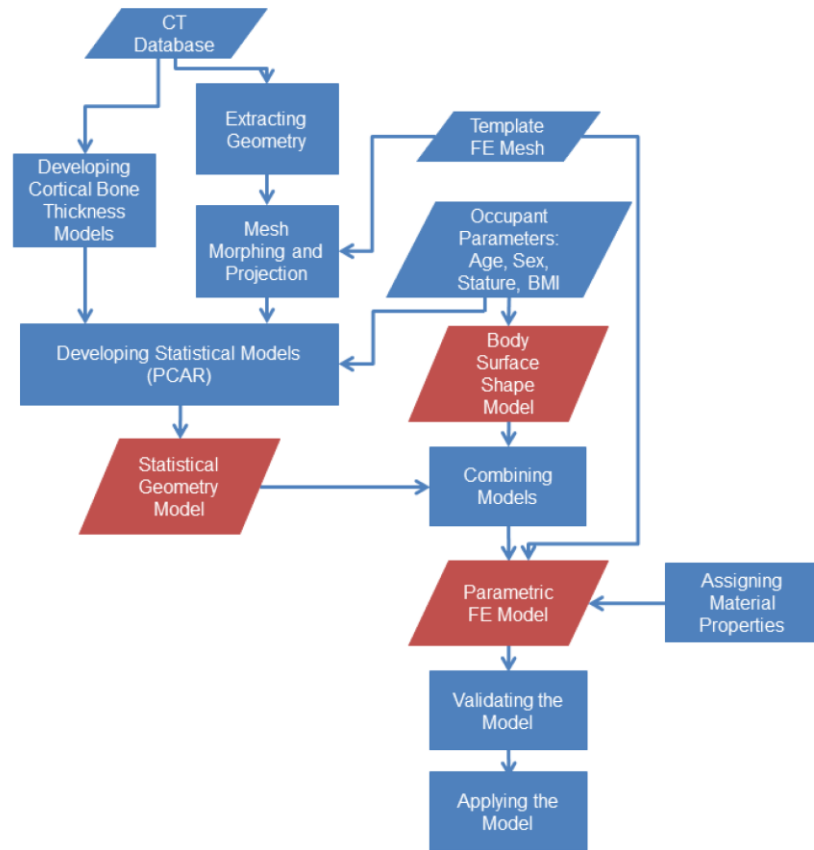


Figure 1-3. Flowchart for development, validation and application of the parametric FE lower-extremity and whole-body models.

Chapter II

Development and Validation of the Statistical Models

INTRODUCTION

Finite element models, and in particular FE models that have geometry and material properties that are parameterized with respect to occupant characteristics are the most efficient method for investigating the reasons for the effects of occupant characteristics on lower-extremity injury risk. However, most current FE human models represent occupants who are one of the three adult size categories for which crash test dummies are available, i.e., the midsize male, small female, and large male (Hu et al. 2012). Previous studies demonstrate that skeletal geometry is an important factor in determining the response and tolerance during potentially injurious loading. Therefore, this chapter describes the methods used to develop and validate statistical models of male and female femur, tibia, and pelvis shape that describe variations in bone geometry with age, BMI, and either bone length (femur and tibia) or bispinous breadth (pelvis). Statistical models for the other lower-extremity bones (patella, fibula, and foot) were not used in this work. Instead, the patella, fibula, and feet are morphed in relation to the external body surface geometry and the femur and tibia models when the whole-body model is developed, as is described in Chapter IV. Parametric models for the femur, tibia, and pelvis only are sufficient for the lower-extremity model because these are the bones that are most relevant in frontal crash loading.

METHODS OVERVIEW

The steps for developing the statistical femur, tibia, and pelvis geometry models are shown in Figure 2-1. The process for developing these models involved extracting geometry from clinical CT scans, fitting template FE meshes to the surface geometries of each patient, and then programmatically determining thickness at each nodal location for the femur and tibia. Principal component analysis and regression (PCAR) analysis was then performed on the geometry nodal coordinates for all bones and thickness for the femur and tibia, and linear regression models were developed to predict geometry as functions of age, BMI, and either bone length (femur and tibia) or bispinous breadth (pelvis) for men and women. The geometry models were validated by comparing bones predicted by the models to the bones from the underlying data set. In addition, the femur models were further validated by comparing model predictions to extracted geometry from a different set of cadaver femurs (Ivarsson et al. 2009). The validity of the tibia and pelvis geometry models was also investigated by comparing the observed landmarks from a small set of different data to the landmarks predicted by the geometry models. This set of data comes from clinical CT scans, but it was not used in the development of the statistical models. A linear mixed models (LMM) analysis was performed for the femur to investigate whether interactions between model predictors could be ignored. The methods for development of the PCAR models facilitate their use as parts of a parametric lower-extremity model.

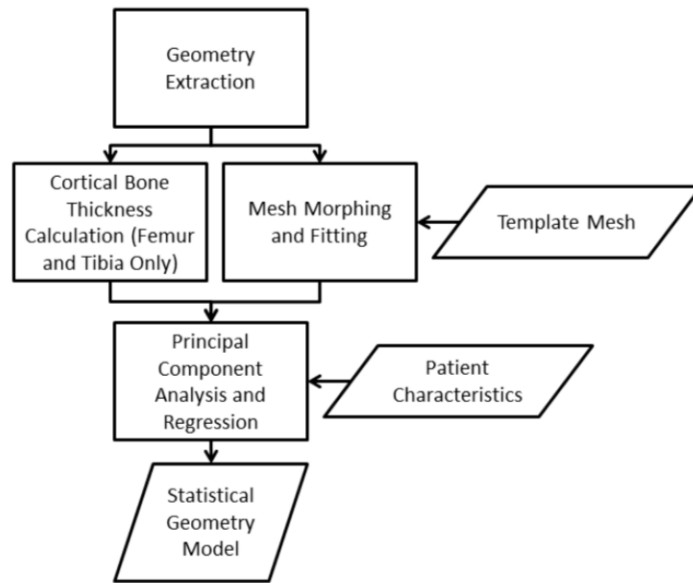


Figure 2-1. Flowchart for the steps used to develop the statistical femur, tibia, and pelvis geometry models.

FEMUR MODEL METHODS

Geometry Extraction

Clinical CT scans of male and female femurs were obtained from the University of Michigan Department of Radiology through a protocol approved by an institutional review board at the University of Michigan. The CT scans were collected using a resolution of 512×512 pixels with 1.25×10^{-3} m between slices. The in-plane resolution varied from 0.625×10^{-3} m to 0.977×10^{-3} m across studies. As shown in Figure 2-2, the patients were selected for age with groups between 18-89 years, patient femur length range was 0.385 m to 0.535 m, and the patient BMI range was 16-46 kg/m². Figure 2-2 shows that no predictor (age, BMI, femur length) was highly correlated with another for men and women. Femur length was measured as described in Figure 2-6.

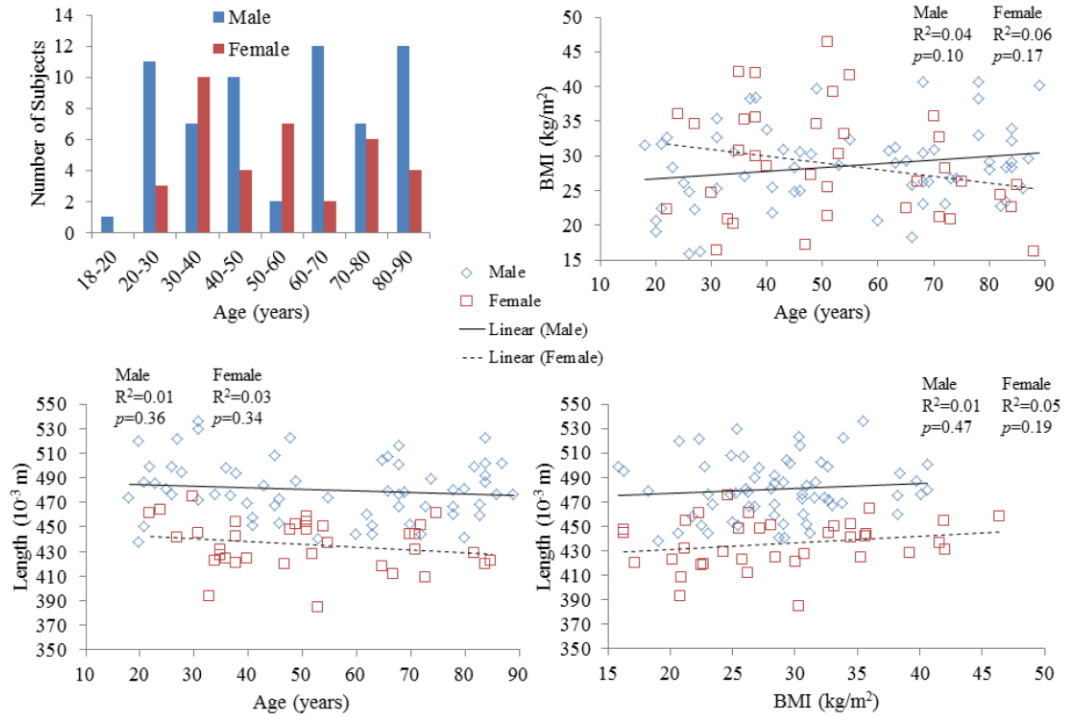


Figure 2-2. Distributions of subject characteristics for the femur data.

Thirty-six female and sixty-two male right femurs were segmented and 3D surfaces were extracted using OsiriX (Pixmeo, Switzerland). The 3D volume rendering mode was used for surface extraction with a Hounsfield Unit threshold value of 300, which was a value sufficiently low enough to capture detailed bone surface geometry. The coordinates of easily distinguishable anatomic landmarks, such as the most lateral point on the greater trochanter of the femur, were manually digitized in Rhinoceros 3D (Robert McNeel & Associates, Seattle, WA). The locations of additional landmarks were calculated programmatically from the locations of the original anatomic landmarks. A total of fifty-nine landmarks were digitized for each femur with thirteen anatomic landmarks used to determine forty-six additional landmarks, and the locations of these are shown in Figure 2-3. The thirteen anatomic landmarks included femoral head center, intercondylar notch, lateral greater trochanter, medial lesser trochanter, superior greater trochanter, medial epicondyle, lateral epicondyle, anterior lateral condyle, posterior lateral condyle, anterior medial condyle, posterior medial condyle, distal lateral condyle, and distal medial condyle. All forty-six additional landmarks were determined using the locations of the thirteen anatomic landmarks, and these forty-six landmarks were calculated to account

for regions with no anatomic landmarks. Thirty-six landmarks were evenly distributed in medial/lateral and anterior/posterior directions along the shaft of the femur, and eight landmarks were on cross-sections of the femoral head and neck to account for the shape of these regions. The last two landmarks were midpoints of lines calculated from anatomic landmarks in the intertrochanteric region and in the neck region. All landmark locations were reviewed to ensure that no errors in selection were made. The errors in landmark locations were investigated to ensure that differences between observers in landmark placement on the same anatomic areas were small. To do this, several people landmarked the same patient and the selected locations were compared. The average difference in landmark locations identified by different observers was 3.8×10^{-3} m across five femurs, which is a small value compared to the overall size of the femur.

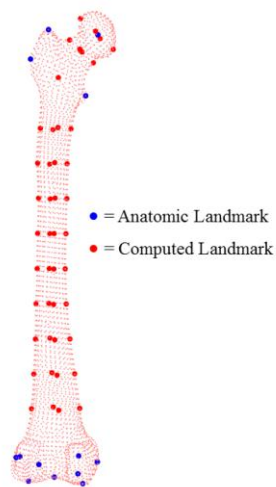


Figure 2-3. The fifty-nine landmark locations on the femur.

Morphing and Fitting Processes

Figure 2-4 illustrates the processes for morphing and fitting a template FE femur mesh onto extracted bone surface geometries. The template mesh comes from the right femur of the Total Human Model for Safety (THUMS) version 4 (Toyota Motor Corporation 2011). The first step in the morphing process involved landmarking the template mesh with the same landmarks that were digitized for the extracted surface geometries from the previous step. These landmarks were manually reviewed to ensure the locations were the

same as for the extracted femur geometries. The nodal coordinates from the template meshes were then morphed into the approximate geometry of each femur using the landmarks on the template meshes and the extracted surface geometries. Morphing was performed using radial basis function (RBF) morphing (Bennink et al. 2006; Carr et al. 2001). RBF morphing is used to morph one surface to another surface based on a set of landmarks and includes several function options such as equations based on thin plate splines ($\phi(r) = r^2 \ln(r)$). Thin plate splines (Bennink et al. 2006) were used in this work because they gave the best accuracy in mesh morphing. RBF morphing was performed by calculating a radial basis interpolation between the source landmarks on the template mesh and each set of target landmarks on each subject's geometry. The radial basis interpolation based on thin plate splines was then applied to the source nodes (template mesh nodes) to obtain sets of morphed nodes for each subject's geometry. Code developed in Mathematica by Bennink et al. (2006) and adapted by researchers at UMTRI was used to implement the RBF morphing, and this code is provided in Appendix A. Next, the morphed meshes were fitted to the surface of each patient's femur to match the patient geometries. Using a method similar to the one described in Reed et al. (Reed et al. 2009), the morphed nodes were moved to the extracted bone surfaces using an implicit surface methodology.

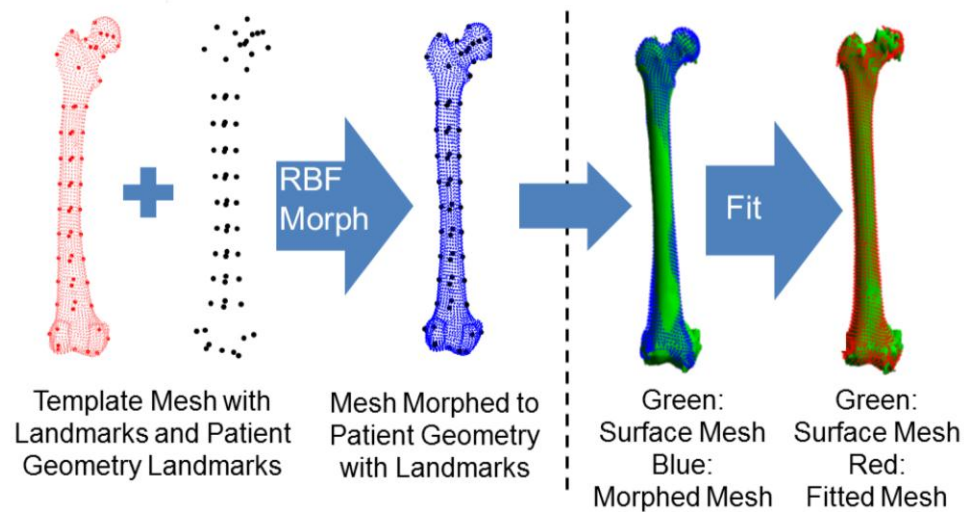


Figure 2-4. Example of the morphing and fitting processes for a template femur FE mesh onto an extracted bone surface geometry.

Cortical Bone Thickness Calculation

An algorithm was developed using Mathematica to calculate the thickness of cortical bone at each nodal coordinate from the morphed and fitted femur meshes, and this algorithm is shown in Figure 2-5. Before this algorithm was applied, the inner surfaces of cortical bone were extracted from the original CT scans in a similar method as for the outer surface using a calculated threshold value determined for each femur to extract only the cortical bone. The surface normals were then calculated at each nodal coordinate, and thickness values were determined based on distances between the outer and inner surfaces along the normal direction using the algorithm. If the thickness value was found to be zero at a nodal location, which occasionally happened near the condyles or the head, an average value from the eight closest points to the node was used to ensure all nodes had a non-zero value. In addition, if the thickness value fell below the 1.25×10^{-3} m minimum value in the ends of the femur, the value was set to 1.25×10^{-3} m in those locations.

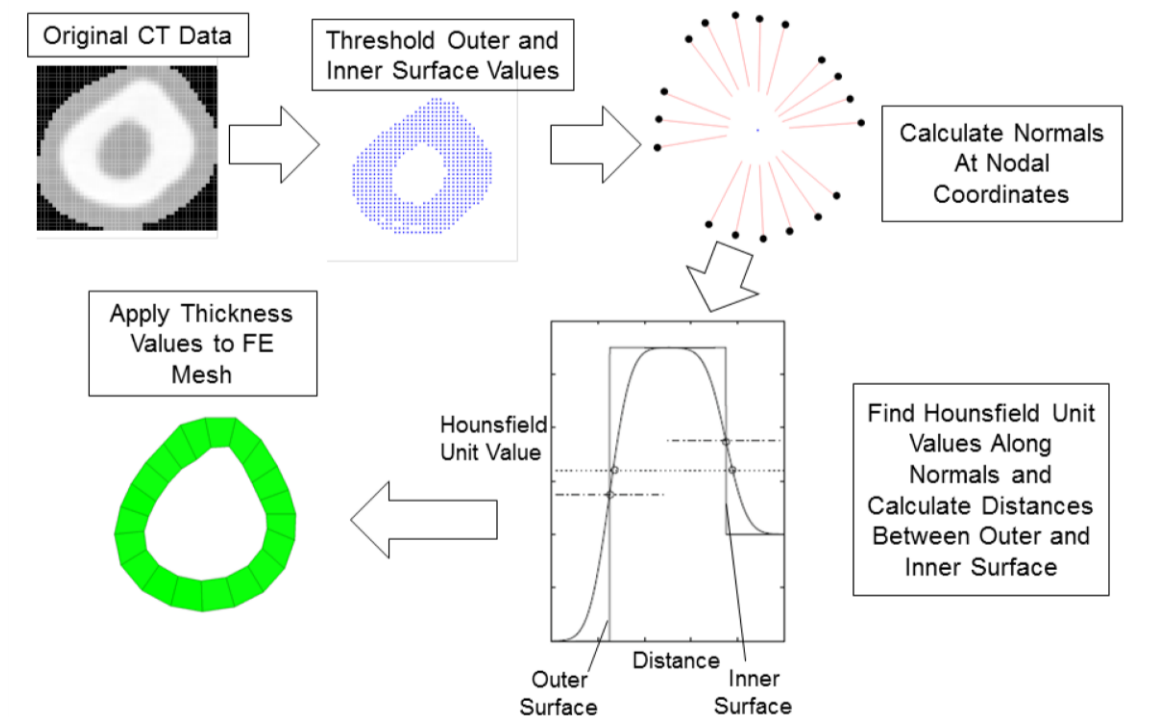


Figure 2-5. Cortical thickness calculation algorithm.

Principal Component Analysis and Regression

Statistical models of femur external surfaces and thicknesses at nodal locations for men and women were developed using PCAR techniques (Jolliffe 2002; Reed and Parkinson 2008). The principal component analysis method used here follows the method discussed by Li et al. (2011). The coordinates of the fitted template meshes were rigidly aligned using Procrustes alignment and rescaling (Slice 2007). Three coordinates at each of the nodes or the associated cortical thickness formed a geometry vector with a length of l (= total number of nodes \times 3 for coordinates, or total number of nodes for thicknesses) denoted as \mathbf{g} for one subject (\mathbf{g}_i for i subjects). The geometry vector for each subject was joined together to construct a geometry matrix \mathbf{G}_1 . To make the PCA method work properly, the geometry matrix \mathbf{G}_1 was centered by subtracting the mean $\bar{\mathbf{g}}$ from each of the subject's \mathbf{g}_i . This matrix is called the data centered matrix \mathbf{G} . PCA was computed by calculating the eigenvalues and eigenvectors of the covariance matrix of the centered geometry matrix \mathbf{G} . \mathbf{G} was decomposed as follows,

$$\mathbf{G} = \mathbf{S}\mathbf{P} \quad (1)$$

$$\mathbf{S} = \mathbf{G}\mathbf{P}^T \quad (2)$$

where \mathbf{S} is an $N \times l$ matrix called principal component (PC) scores and \mathbf{P} is the eigenvectors of \mathbf{G} , which is an $l \times l$ -normalized matrix. Any subject's nodal coordinates or thicknesses could be obtained based on Equation 3,

$$\mathbf{g}_i^* = \bar{\mathbf{g}} + \mathbf{P}_N^T \mathbf{S}_{Ni}^T \quad (3)$$

where \mathbf{S}_{Ni} is the row of matrix \mathbf{S}_N corresponding to the i th subject's PC scores.

To use the parameters such as age, BMI, and bone length to predict PC scores (\mathbf{S}_k), and in turn, to predict detailed LX geometry, a regression analysis was performed. A regression model was generated following the procedure used in Reed et al. (Reed et al. 2009),

$$\mathbf{S}_k^T = \mathbf{C}\mathbf{F} + \varepsilon^T \quad (4)$$

where \mathbf{F} is the feature matrix, \mathbf{C} is the coefficient matrix, ε^T is a vector of zero mean and normally distributed residuals.

Regression model predictions of PC scores were then used to reconstruct external femur surface coordinates and nodal thicknesses. Femur nodal coordinates were predicted using this regression analysis as functions of age, BMI, and femur length (which strongly correlates with stature) with separate models for men and women. Femur length is defined here as the distance along the long axis of the femur (determined from a line between midpoints of lines determined from anatomic landmark locations in the landmarking process) between the most superior point on the femoral head and most inferior point on the femoral condyles, and is shown in Figure 2-6. This femur length definition was used for comparison to validation data and can be altered depending on model use. Femur nodal thicknesses were predicted using the regression analysis as functions of age, BMI, and significant PC scores from the surface geometry models. The significant PC scores from the femur nodal coordinates models were used as potential predictors in the thickness regression functions due to the possible effects of external geometry on thickness. Significant PC scores were determined using a forward stepwise approach. The first 10 PC scores were considered since they accounted for most of the variance in external surface geometry, and a PC score was kept if its p -value was less than 0.05.

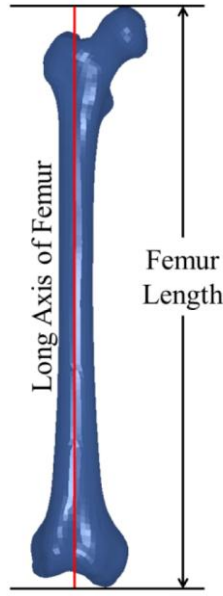


Figure 2-6. Femur length defined as the distance along the long axis of the femur (determined from anatomic landmark locations in the landmarking process) between the most superior point on the femoral head and most inferior point on the femoral condyles.

Right femurs were predicted and used in this study because the FE models that will eventually be used are symmetric and left femurs can be determined from reflecting the femur about the symmetric (Y) axis. The PCAR models used the same number of PC scores as number of subjects used to develop the models (36 for women and 62 for men). These numbers of PCs covered more than 99% of the variance in the data.

Evaluating the error in regression models predicting PC scores is of minimal value as error in the original coordinate system is the metric of interest. Instead, goodness of fit was investigated by assessing the improvement in femur geometry prediction obtained when using the regression model rather than the average femur. Values for cross-sectional area and cortical bone thickness along the shaft were compared between the femur data used to develop the statistical model and the femurs predicted using the original data's characteristics. A leave-one-out cross validation was performed for the female femurs to further validate the statistical models. This leave-one-out cross validation was done by removing one subject from the data, refitting the regression model to the data with one less subject, predicting the subject that was left out, calculating the error in the resulting model, and repeating for each subject. In addition, model

predictions for the femur were compared to extracted geometry from a different set of cadaver femurs (Ivarsson et al. 2009).

Linear Mixed Models Analysis

A LMM analysis was performed on cross-sectional areas at six different locations along the femur to investigate whether interaction effects between model parameters from PCAR models could be ignored. Random effects with an assumed normal distribution in this analysis were age, stature, and BMI, and fixed effects were sex and femur location. Separate models were developed to characterize the effects of these random and fixed effects on total cross-sectional bone area (total bone area) and cortical cross-sectional bone area (cortical bone area). Sex was included as a predictor to assess potential interactions. Cortical bone areas and the total bone areas were calculated at five evenly spaced locations along the shaft of the right femur. Total bone area was also calculated at a sixth location on the femoral neck. These six locations along the femur and the definitions of total bone area and cortical bone area are shown in Figure 2-7. Location 1 is located at 25% of the total femur length below the most superior point on the femur and location 5 is located at 25% of the total femur length above the most inferior point. Locations 2, 3, and 4 are spaced evenly between locations 1 and 5. Cortical bone area at the femoral neck was not calculated because cortical bone thickness was similar to the CT scan slice size and, as a result, the cortical thickness could not be accurately calculated. Similar to the methods in Shi et al. (2014), a stepwise procedure was used to find the significant predictors starting with fixed effects from single predictors and adding interaction terms between the significant predictors in the following steps. The model with the lowest Akaike Information Criterion (AIC) value was used (Akaike 1974).

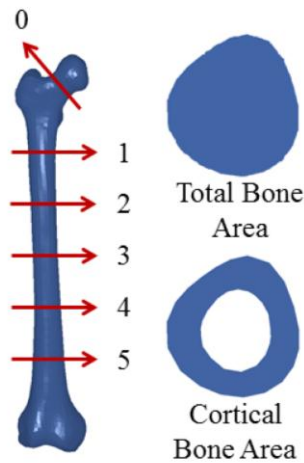


Figure 2-7. The five area locations (1-5) along the shaft of the femur and the one neck location (0) used for area measurements and the definitions of total bone area and cortical bone area.

FEMUR MODEL RESULTS

Principal Component Analysis and Regression

Overall R^2 values for the external geometry models and thickness models were calculated using Equation 5 where the residual sum of squares was the sum of squared errors between the observed and predicted coordinates or thicknesses, and the total sum of squares was the sum of squared differences between the observed coordinates and average coordinates or the observed thickness values and the average thicknesses. The overall calculated R^2 values for the male and female external geometry models were 0.77 and 0.74, respectively. The overall calculated R^2 values for the male and female femur thickness models were 0.31 and 0.36, respectively. The p -values from analysis of variance tests for the predictors on the first five principal components for the male and female femur external geometry models and thickness models are shown in Tables 2-1 and 2-2. The predictors used in the analysis of variance test for the geometry models were age, BMI, and femur length. The predictors used for the femur thickness models were age, BMI, and significant PC scores from the geometry models. Femur length had

the largest coefficient value in the male and female external geometry model regressions, indicating that length explains the largest portion of variance. BMI explained the largest portion of the variance in the male and female thickness models.

$$R^2 = 1 - \frac{\text{Residual sum of squares}}{\text{Total sum of squares}} \quad (5)$$

Table 2-1. *p*-values of predictors in the female and male femur external geometry models

Predictor		<i>p</i> -value				
		1st PC	2nd PC	3rd PC	4th PC	5th PC
Female Geometry	Age	0.300	0.378	0.019*	0.823	0.227
	Femur Length	0.000*	0.602	0.550	0.799	0.978
	BMI	0.001*	0.001*	0.832	0.903	0.011*
Male Geometry	Age	0.057	0.000*	0.058	0.894	0.103
	Femur Length	0.000*	0.934	0.574	0.570	0.813
	BMI	0.115	0.069	0.399	0.923	0.089

**p*<0.05

Table 2-2. *p*-values of predictors in the female and male femur thickness models

Predictor		<i>p</i> -value				
		1st PC	2nd PC	3rd PC	4th PC	5th PC
Female Thickness	Age	0.739	0.056	0.063	0.138	0.098
	BMI	0.030*	0.210	0.026*	0.178	0.621
	Geometry PC Score 2	0.140	0.213	0.158	0.998	0.315
	Geometry PC Score 5	0.018*	0.614	0.050	0.454	0.837
	Geometry PC Score 6	0.238	0.194	0.395	0.246	0.011*
	Geometry PC Score 7	0.017*	0.489	0.243	0.135	0.638
Male Thickness	Age	0.109	0.646	0.000*	0.080	0.090
	BMI	0.015*	0.150	0.313	0.050	0.224
	Geometry PC Score 3	0.949	0.001*	0.110	0.653	0.528
	Geometry PC Score 6	0.223	0.000*	0.219	0.863	0.920
	Geometry PC Score 9	0.011*	0.843	0.400	0.054	0.162

**p*<0.05

The effects of age, femur length, BMI, and gender on femur geometry predicted by the femur parametric models are shown in Figure 2-8. These femur models were created by

varying one parameter at a time and holding the other parameters constant. The cross-sections for five evenly spaced locations along the shaft are also shown for comparison. The models in these figures were aligned using a Procrustes approach rather than section centroids.

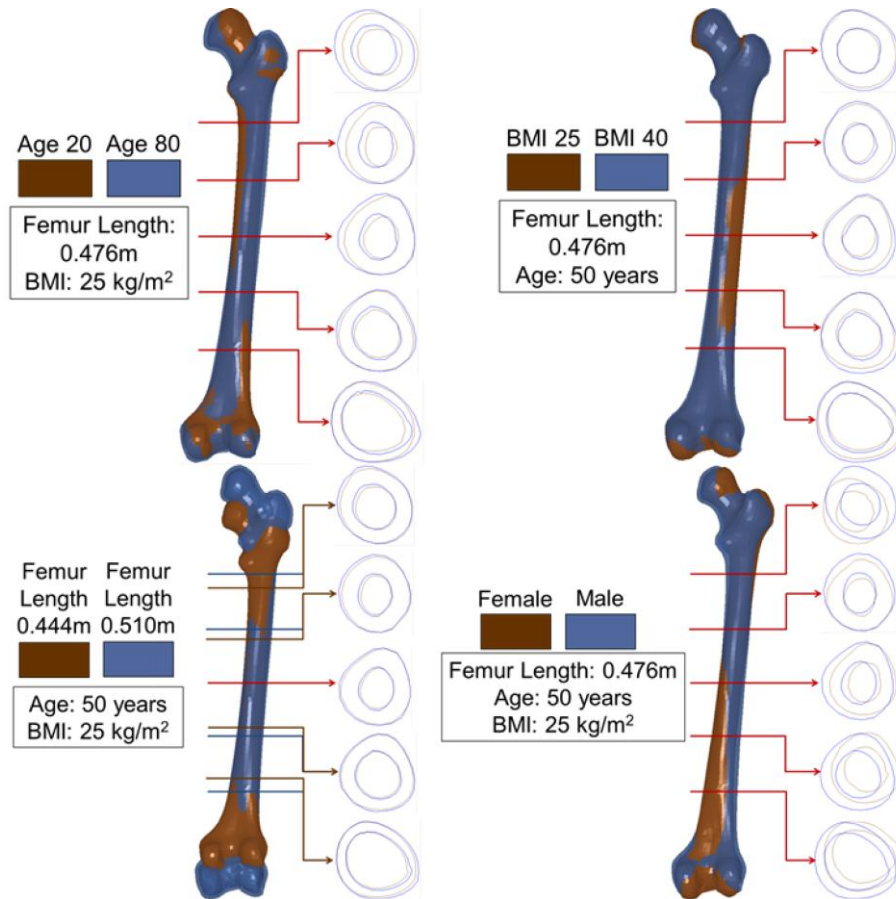


Figure 2-8. The effects of age, BMI, femur length, and gender on femur geometry predicted by the parametric models.

Midshaft cross-sectional cortical bone areas were calculated for the femur predicted geometries and the actual femur geometries, and the mean of the errors in predicted areas calculated as percentages of the original areas was 4.4%. The mean Euclidean distance between predicted and measured nodal coordinates and 95th percentile errors in nodal coordinate locations between the fitted meshes to the actual data and the predicted meshes were calculated. The distributions of errors in femur surface geometry are shown for both the male and female models in the left side of Figure 2-9. The mean and 95th percentile absolute differences between the actual thicknesses and predicted thicknesses

were also calculated. The distributions of these differences are shown in the right side of Figure 2-9. For the nodal coordinates, the larger errors occur in the ends of the femur. The residuals for each model were checked for normal distributions and no trends were seen with any model predictor. The leave-one-out cross validation gave a mean error of 3.49×10^{-3} m in overall Euclidean distance errors compared to 3.42×10^{-3} m for the original models, indicating that these models were valid.

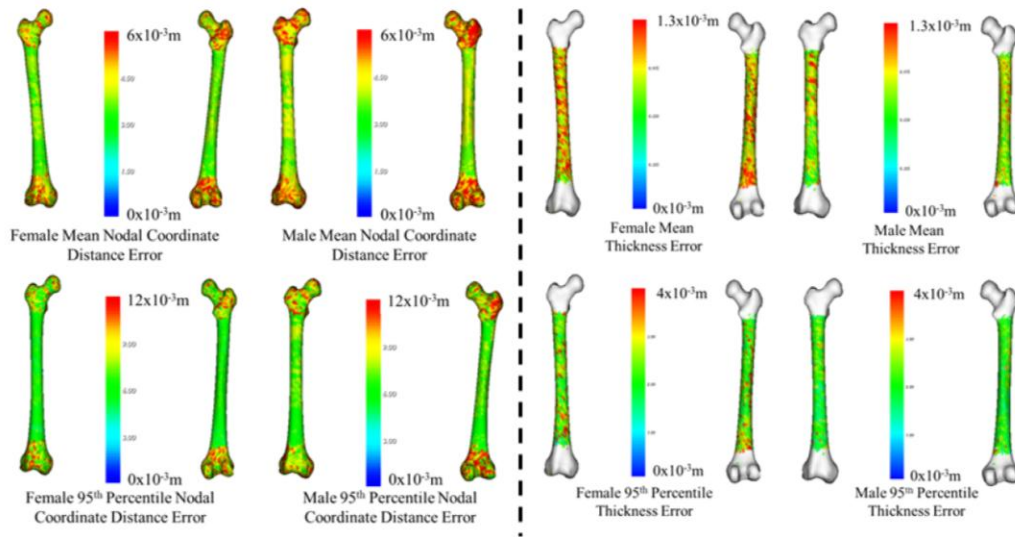


Figure 2-9. Distribution of mean and 95th percentile absolute errors in nodal coordinate locations (left two columns) and cortical thickness values at nodal locations (right two columns) between the actual femur data and predicted geometries.

The average Euclidean distance error in nodal coordinate locations based on the morphed template nodes between the 13 predicted shaft geometries from the statistical models and the shaft geometries from the CT scans of the Ivarsson et al. (Ivarsson et al. 2009) study after alignment using Procrustes alignment and rescaling was 4.8×10^{-3} m. The difference between the predicted error and average error indicates that predicting geometry using subject characteristics can more closely match real geometry than the average models normally used. The average error in midshaft cross-sectional cortical bone area between the predicted geometries and the PMHS geometries was 7.6%, and the average error between the predicted areas and the PMHS areas across the 5 locations was 2.9%. The errors in cortical bone area calculated at 5 different locations along the shaft between the

actual shafts and the predicted shafts are given in boxplots in Figure 2-10 with the average error indicated. The cortical bone areas were also compared qualitatively at midshaft to validate the predicted models, and Figure 2-11 shows the midshaft PMHS femur cross-sectional areas overlaid on the predicted areas.

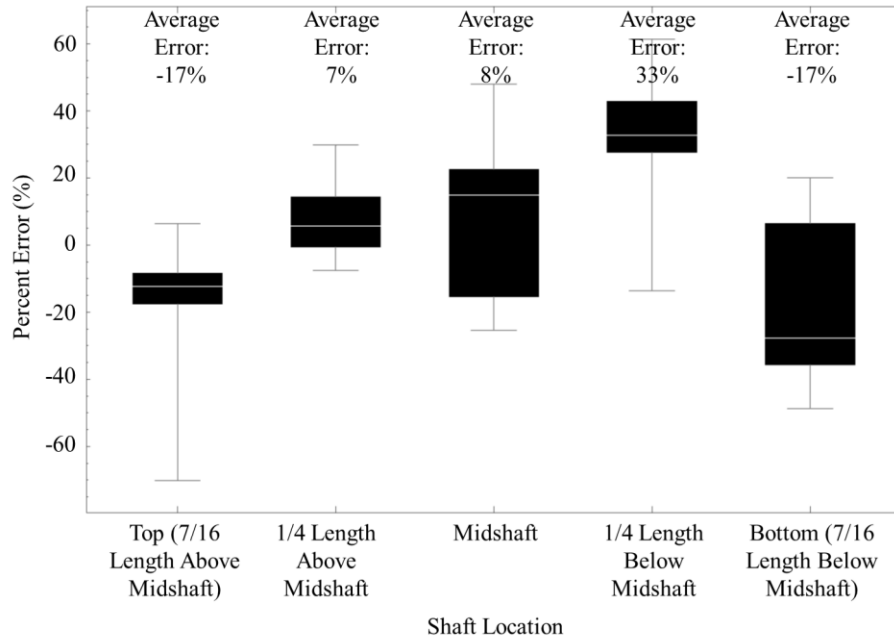


Figure 2-10. Cortical bone cross-sectional areas at five locations along the shafts of the PMHS femurs and the errors in the predicted shaft cross-sectional areas.

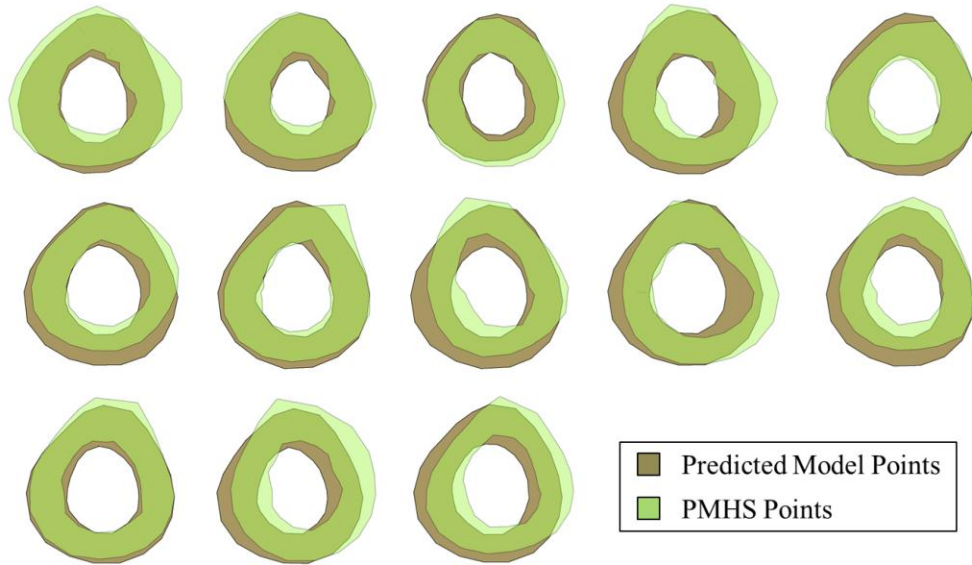


Figure 2-11. Midshaft cross-sectional areas of the 13 PMHS femurs and the predicted femur models.

Linear Mixed Models Analysis

Figure 2-12 shows the sex effects on total bone area at the neck (location 0) and 5 locations along the shaft (locations 1-5) and cortical bone area at the same 5 shaft locations by sex and location. In general, male femurs have a higher total bone area and larger cortical bone area than female femurs when other predictors are held constant at the same levels. Total bone area and cortical bone area at each of the levels increase with increasing stature, and total bone area increases with increasing age.

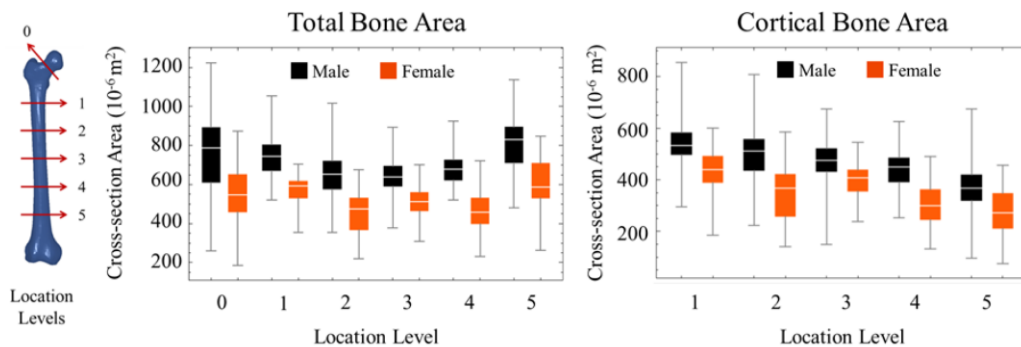


Figure 2-12. Distribution of femur cross-sectional areas by sex and location level.

The LMM results for cortical bone area and total bone area are shown in Tables 2-3 and 2-4, respectively. The significance of the predictors is listed with their coefficients determined from the regression. LMM analyses were performed with 2-way interactions, but 3-way interactions were also investigated since significant 3-way interactions were postulated. Although significant 3-way interactions were identified, the AIC score was not different when these interactions were included; therefore, the most parsimonious model was used. For the cortical area model, all fixed effect predictors were significant, and all random effect predictors except for BMI were significant in the total bone area model. The interaction of Stature*Location_Level was significant for the cortical bone model, while the interactions of Age*Location_Level and Location_Level*Sex were significant for the total bone area model ($p<0.05$). These results indicate that the stature effects on cortical bone area vary significantly by location, and the models predict that the increase in cortical area with increasing stature is greater for locations 2 and 4 (above and below midshaft) than the other locations. In addition, the age and sex effects on total bone area vary significantly by location. The models predict that the increase in total bone area with increasing age is greater for location 0 (the femoral neck) and smaller for locations 4 and 5 (bottom of the shaft) than the other locations. Larger differences in total bone areas between men and women exist for locations 1 (top of shaft) and 4 (below midshaft) than for the other locations. The significance levels for the predictors are shown in Tables 2-5 and 2-6.

Table 2-3. Cortical cross-sectional bone area model data

Effect	Estimate ¹	Standard Error	DF ²	t Value	Pr > t	
Intercept	-483.6	132.2	93.5	-3.7	0.0004	
Age (years)	0.7	0.3	93.0	2.7	0.0084	
Stature (m)	373.9	82.8	93.0	4.5	<.0001	
BMI (kg/m ²)	3.8	0.9	93.0	4.4	<.0001	
Male	48.3	17.5	93.0	2.8	0.0069	
Female	-48.3	-	-	-	-	
Location Level ³	1	162.8	10.4	388.0	15.7	<.0001
	2	111.1	10.4	388.0	10.7	<.0001
	3	104.1	10.4	388.0	10.0	<.0001
	4	56.0	10.4	388.0	5.4	<.0001
	5	0	-	-	-	-

Table 2-4. Total cross-sectional bone area model data

Effect	Estimate ¹	Standard Error	DF ²	t Value	Pr > t	
Intercept	-620.8	158.4	93.7	-3.9	0.0002	
Age (years)	1.5	0.3	93.0	5.0	<.0001	
Stature (m)	685.4	99.1	93.0	6.9	<.0001	
BMI (kg/m ²)	1.7	1.0	93.0	1.7	0.0947	
Male	67.5	20.9	93.0	3.2	0.0017	
Female	-67.5	-	-	-	-	
Location Level ³	0	-47.8	14.7	485.0	-3.3	0.0012
	1	-39.7	14.7	485.0	-2.7	0.0070
	2	-149.4	14.7	485.0	-10.2	<.0001
	3	-141.8	14.7	485.0	-9.7	<.0001
	4	-123.7	14.7	485.0	-8.4	<.0001
	5	0	-	-	-	-

¹ Coefficient values for the linear model.

² Degrees of freedom of each predictor.

³ Location levels as defined in Figure 2-3.

Table 2-5. Significance levels of predictors in the cortical bone mixed models

<u>Effect</u>	<u>Num DF</u>	<u>Den DF</u>	<u>F Value</u>	<u>Pr > F</u>
Age	1	93.02	7.25	0.0084
Stature	1	93.02	20.40	<.0001
BMI	1	93.02	19.76	<.0001
Gender	1	93.02	7.64	0.0069
Location_Level	4	384	5.20	0.0004
Stature*Location_Level	4	384	5.51	0.0003

Table 2-6. Significance levels of predictors in the total bone mixed models

<u>Effect</u>	<u>Num DF</u>	<u>Den DF</u>	<u>F Value</u>	<u>Pr > F</u>
Age	1	94.01	25.91	<.0001
Stature	1	94.01	60.76	<.0001
Gender	1	94.01	8.14	0.0053
Location_Level	5	475	7.09	<.0001
Age *Location_Level	5	475	2.75	0.0184
Location_Level*Gender	5	475	2.41	0.0354

TIBIA MODEL METHODS

Geometry Extraction

Tibia geometry was extracted using the same methods as those used for femur geometry extraction described above. As shown in Figure 2-13, the patient age groups were between 21-89 years, patient tibia length range was 0.328 m to 0.454 m, and patient BMI range was 15-43 kg/m². Figure 2-13 shows that no predictor (age, tibia length, and BMI) was highly correlated with another for the tibia data set.

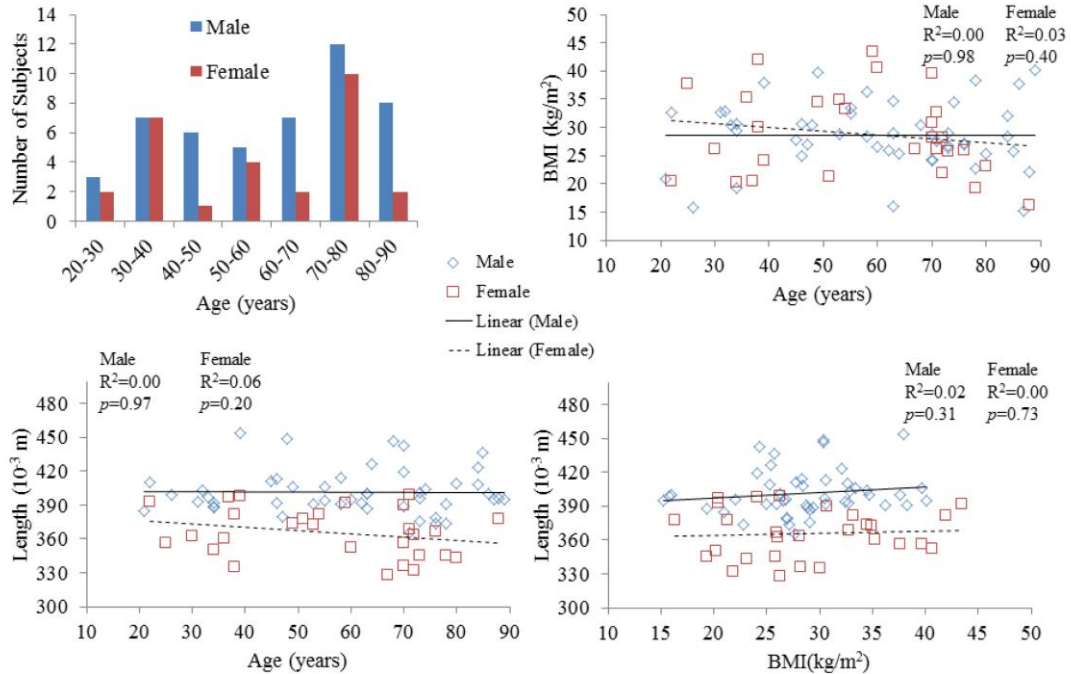


Figure 2-13. Distributions of subject characteristics for the tibia data.

Tibias were segmented and 3D surfaces were extracted from twenty-eight female and forty-eight male subjects. Seventy-six landmarks were digitized for each tibia with seven anatomic landmarks used to determine sixty-nine additional landmarks, and the locations of these landmarks are shown in Figure 2-14. The seven anatomic landmarks include the intercondylar tubercles, points on the tibial plateau, the tibial tuberosity, and two points on the medial malleolus. Forty of the sixty-nine additional landmarks were evenly distributed in medial/lateral and anterior/posterior directions along the shaft of the tibia, and twenty of those points were evenly spaced along the edge of the tibial plateau. The last nine additional points were midpoints of lines calculated between anatomic landmark locations and interpreted points based on points placed on the fibula.

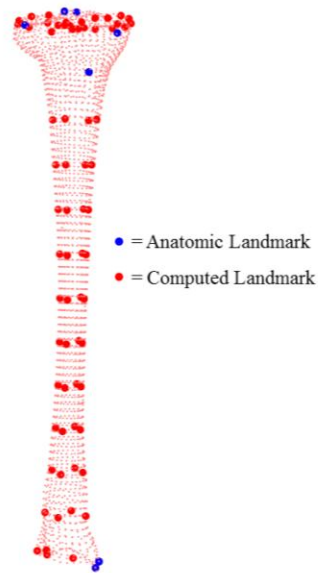


Figure 2-14. The seventy-six landmark locations on the tibia.

Morphing and Fitting Processes

The same morphing and fitting processes used for the femur were also used for the tibia. The template mesh comes from the right tibia of the Total Human Model for Safety (THUMS) version 4 (Toyota Motor Corporation 2011).

Cortical Bone Thickness Calculation

The thickness values of cortical bone were calculated at each nodal coordinate of the morphed and fitted tibia meshes using the same algorithm as was used for the femur. In addition, if the thickness value fell below the 1.25×10^{-3} m minimum value in the ends of the tibia, the value was set to 1.25×10^{-3} m in those locations.

Principal Component Analysis and Regression

Statistical models of tibia external surfaces and thicknesses at nodal locations for men and women were developed using the same PCAR techniques as for the femur models. Tibia nodal locations and the associated cortical thickness values were predicted using this regression analysis as functions of age, BMI, and tibia length (which strongly correlates with stature) with separate models for men and women. In addition, the

thickness models used significant PC scores from the geometry models as potential predictors in their regression functions due to the possible effects of external geometry on thickness. Tibia length is defined as the Euclidean distance between the most anterior point on the tibial tuberosity and the most inferior point on the medial malleolus, and is shown in Figure 2-15. This length is used to correspond to landmark locations from a body surface model that will be used when morphing the whole-body FE model in Chapter IV. Right tibias were predicted and used in this study because the FE models are symmetric and left tibias can be determined from reflecting the tibia. The PCAR models use the same number of PC scores as number of subjects used to develop the models (28 for women and 48 for men). These numbers of PCs cover more than 99% of the variance in the data.

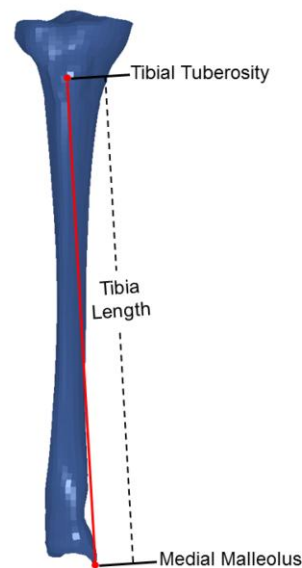


Figure 2-15. Tibia length defined as the Euclidean distance the most anterior point on the tibial tuberosity and the most inferior point on the medial malleolus.

To investigate the validity of the statistical tibia models, values for cross-sectional area and cortical bone thickness along the shaft were compared between the tibia data used to develop the statistical model and the tibias predicted using the original data's characteristics. In addition, errors between the actual data and the predicted geometries were determined. As a further validation, the errors between model-predicted landmarks and a small set of different data not included in the original dataset were determined.

TIBIA MODEL RESULTS

Principal Component Analysis and Regression

Overall R^2 values for the tibia external geometry models and thickness models were calculated in the same way as for the femur models using Equation 5 defined previously. The overall calculated R^2 values for the male and female external geometry models were 0.68 and 0.84, respectively. The overall calculated R^2 values were 0.39 and 0.38 for the male and female tibia thickness models, respectively. The p -values from analysis of variance tests for the predictors on the first five principal components for the male and female tibia external geometry models and tibia thickness models are shown in Tables 2-7 and 2-8. The predictors used in the analysis of variance test for the geometry models were age, BMI, and tibia length. The predictors used for the tibia thickness models were age, BMI, and significant PC scores from the geometry models. Tibia length explained the largest portion of variance for the male and female external geometry models, while geometry PC score 5 in the male thickness models and age in the female thickness models explained the greatest portion of variance.

Table 2-7. p -values of predictors in the female and male tibia external geometry models

Predictor		p -value				
		1st PC	2nd PC	3rd PC	4th PC	5th PC
Female Geometry	Age	0.544	0.040*	0.560	0.694	0.454
	Tibia Length	0.000*	0.556	0.591	0.986	0.819
	BMI	0.213	0.190	0.243	0.717	0.783
Male Geometry	Age	0.021*	0.199	0.642	0.015*	0.051
	Tibia Length	0.000*	0.955	0.600	0.732	0.750
	BMI	0.628	0.386	0.878	0.022*	0.865

* $p < 0.05$

Table 2-8. *p*-values of predictors in the female and male tibia thickness models

Predictor		<i>p</i> -value				
		1st PC	2nd PC	3rd PC	4th PC	5th PC
Female Thickness	Age	0.000*	0.373	0.048*	0.635	0.709
	BMI	0.009*	0.531	0.902	0.155	0.800
	Geometry PC Score 3	0.620	0.003*	0.894	0.311	0.817
	Geometry PC Score 4	0.009*	0.968	0.253	0.456	0.546
	Geometry PC Score 6	0.020*	0.654	0.566	0.588	0.376
Male Thickness	Age	0.561	0.626	0.012*	0.705	0.847
	BMI	0.973	0.500	0.895	0.885	0.266
	Geometry PC Score 2	0.802	0.806	0.305	0.005*	0.000*
	Geometry PC Score 5	0.009*	0.051	0.672	0.000*	0.092
	Geometry PC Score 6	0.036*	0.199	0.593	0.003*	0.032*
	Geometry PC Score 8	0.159	0.659	0.734	0.026*	0.877
	Geometry PC Score 9	0.729	0.155	0.285	0.001*	0.941

**p*<0.05

The effects of age, tibia length, BMI, and gender on tibia geometry predicted by the tibia parametric models are shown in Figure 2-16. These tibia models were created by varying one parameter at a time and holding the other parameters constant. The cross-sections at midshaft are also shown for comparison. The models in these figures were aligned using a Procrustes approach rather than section centroids.

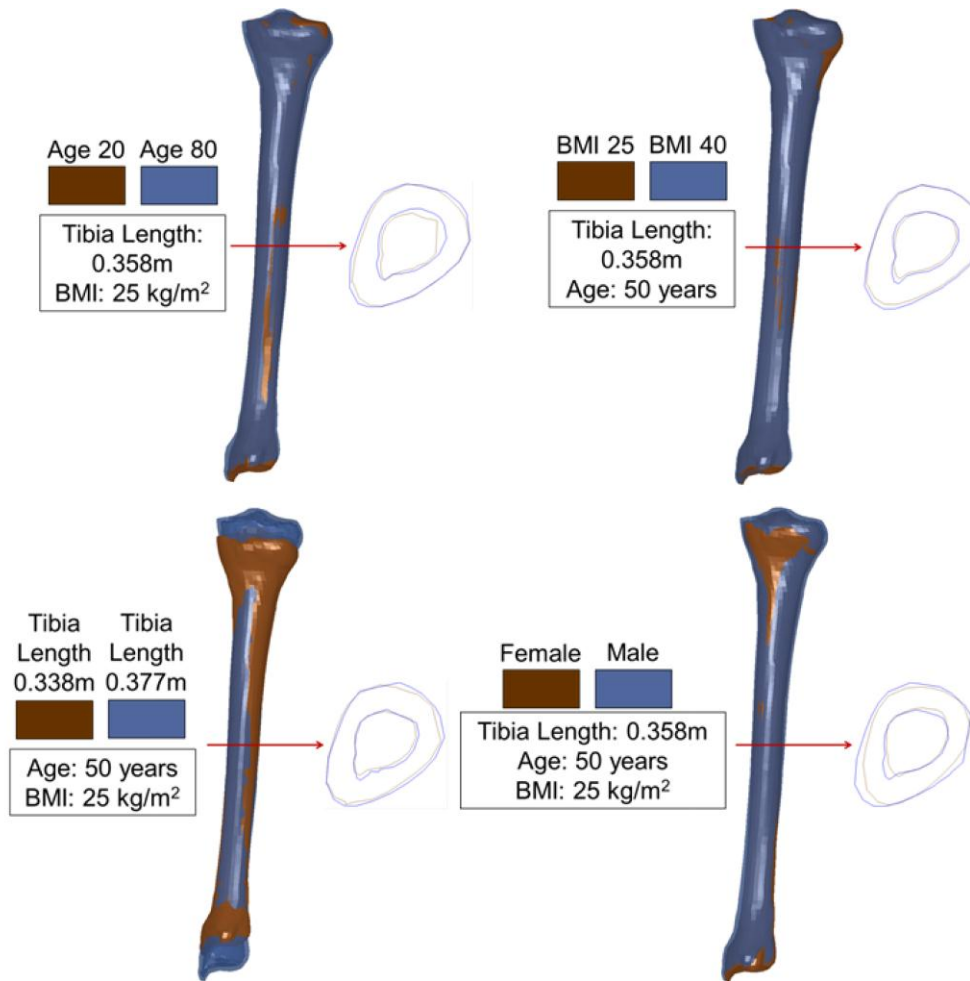


Figure 2-16. The effects of age, BMI, tibia length, and gender on tibia geometry predicted by the parametric models.

Midshaft cross-sectional cortical bone areas were calculated for the tibia predicted geometries and the actual tibia geometries, and the mean of the errors in predicted areas calculated as percentages of the original areas was 16.1%. The mean distance errors and 95th percentile errors in nodal coordinate locations between the fitted meshes to the actual data and the predicted meshes were calculated, and the distributions of errors in the tibia can be seen for both the male and female models in Figure 2-17. The mean and 95th percentile absolute differences between the actual thicknesses and predicted thicknesses were also calculated for the tibia, and the distributions of differences are shown in Figure 2-17. For the nodal coordinate errors, the larger errors occur in the ends of the tibia. The residuals for each model were checked for normal distributions and no trends were seen with any model predictor. The mean distance errors between observed and predicted

landmark locations for a set of nine males and six females spanning several decades of ages were determined. Male models had a mean distance error of 11×10^{-3} m, and female models had a mean distance error of 9×10^{-3} m. The landmark errors were evenly distributed throughout the tibia surface, and the errors were similar to the errors seen in the comparisons to the underlying dataset.

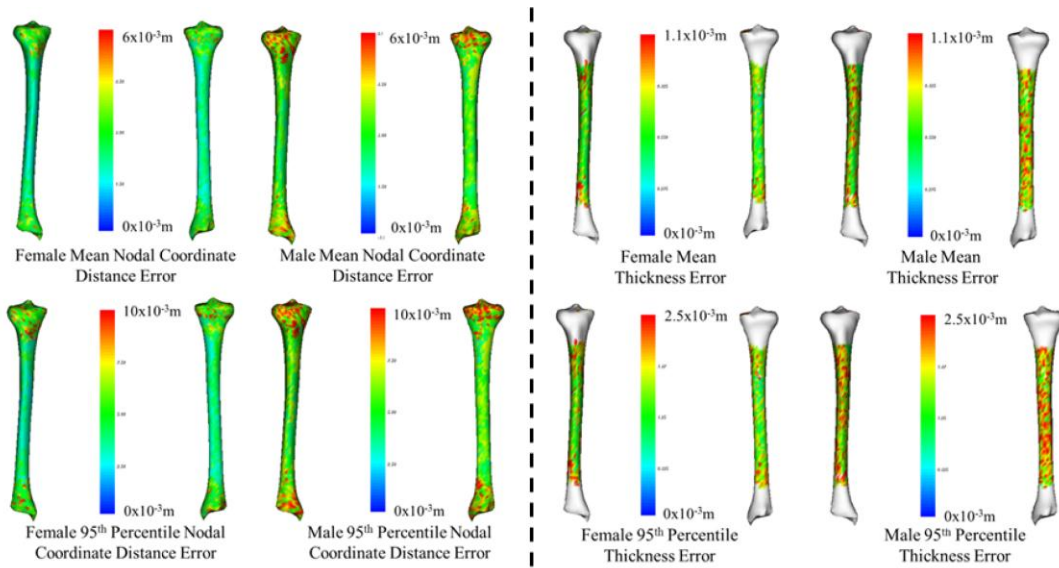


Figure 2-17. Distribution of mean and 95th percentile absolute errors in nodal coordinate locations (left two columns) and cortical thickness values at nodal locations (right two columns) between the actual tibia data and predicted geometries.

PELVIS MODEL METHODS

Geometry Extraction

Pelvis geometry was extracted using the same methods as the femur and tibia extraction.

As shown in Figure 2-18, the patient age groups were between 17-88 years, patient bispinous breadth range was 0.179-0.277 m, and patient BMI range was 15-46 kg/m^2 .

Figure 2-18 shows that no predictor was highly correlated with another for the pelvis data set.

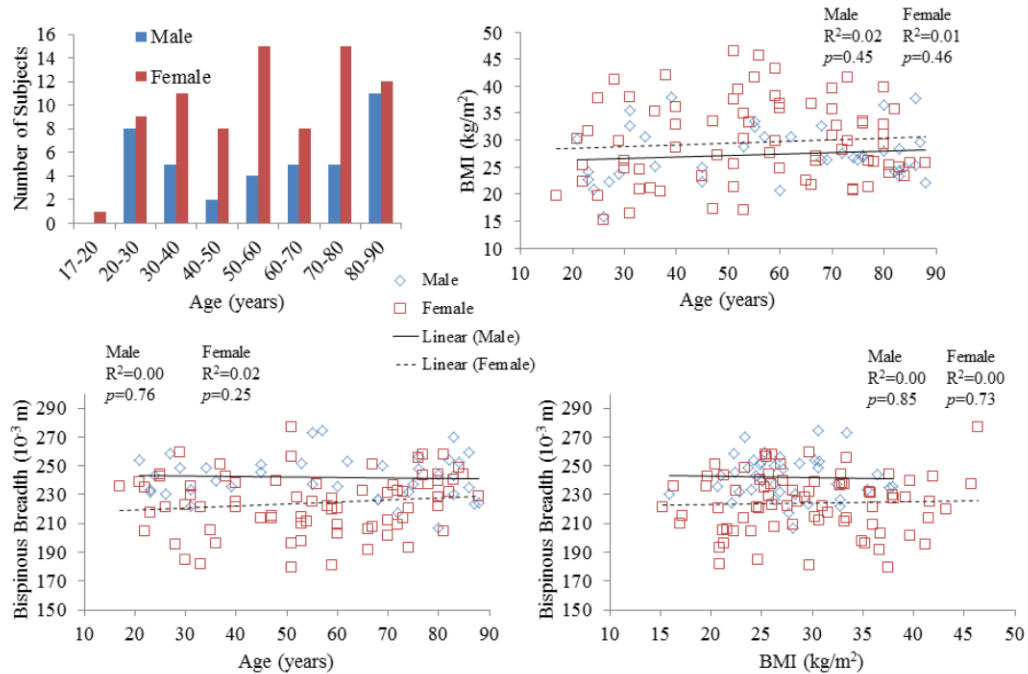


Figure 2-18. Distributions of subject characteristics for the pelvis data.

Pelves were segmented and 3D surfaces were extracted from seventy-seven female and thirty-nine male subjects. Forty-seven landmarks were digitized for each pelvis with thirty-one anatomic landmarks used to determine sixteen additional landmarks, and the locations of these landmarks are shown in Figure 2-19. The thirty-one anatomic landmarks included three places on the right and left iliac wings, posterior superior iliac spine, anterior superior iliac spine, inferior iliac spine, symphyseal pole, pubic symphysis, ischial tuberosity, acetabular notch, ischial spine, and points on the first sacral segment. The additional sixteen landmarks were determined from cross-sections at the pubic rami.

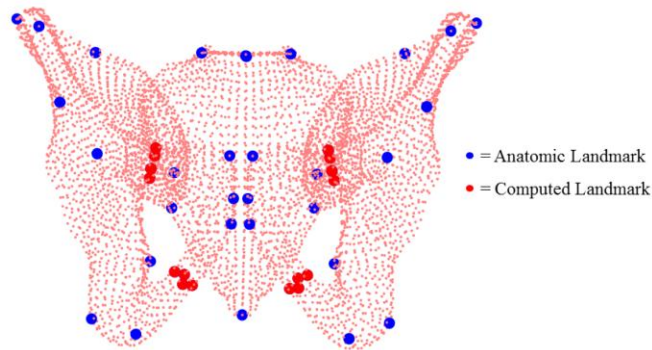


Figure 2-19. The locations of the forty-seven landmarks on the pelvis.

Morphing and Fitting Processes

The same morphing and fitting processes used for the femur and tibia were used for the pelvis. The template mesh comes from the pelvis of the Total Human Model for Safety (THUMS) version 4 (Toyota Motor Corporation 2011).

Principal Component Analysis and Regression

Statistical models of pelvis external geometry for men and women were developed using the same PCAR techniques as the femur and tibia external surfaces. Pelvis nodal locations were predicted using this regression analysis as functions of age, BMI, and bispinous breadth with separate models for men and women. Bispinous breadth is defined as the distance between the anterior superior iliac spines (ASIS) on the left and right side of the pelvis, and is shown in Figure 2-20. This parameter is used instead of stature because it corresponds to landmarks from the external body surface shape model and is useful for the whole-body morphing that will be described in Chapter IV. The PCAR models use the same number of PC scores as number of subjects used to develop the models (77 for women and 39 for men). These numbers of PCs cover more than 99% of the variance in the data. To investigate the validity of the statistical pelvis models, errors between the actual pelvis data and the predicted geometries were determined. As a further validation, the errors between model-predicted landmarks and a small set of different data not included in the original dataset were determined.

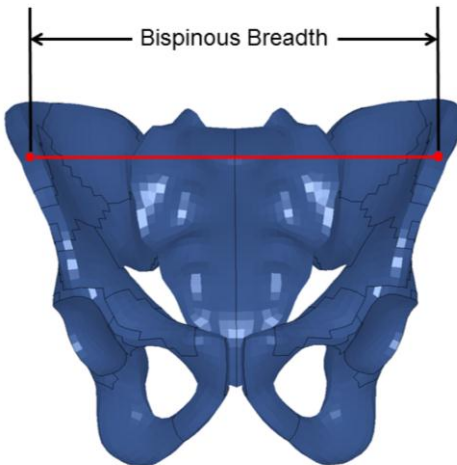


Figure 2-20. Bispinous breadth defined as the distance between the anterior superior iliac spines on the left and right side of the pelvis.

PELVIS MODEL RESULTS

Principal Component Analysis and Regression

Overall R^2 values for the external geometry models were calculated using Equation 1 where the residual sum of squares was the sum of squared errors between the observed and predicted coordinates, and the total sum of squares was the sum of squared differences between the observed coordinates and average coordinates. The overall calculated R^2 values for the male and female external geometry models were 0.15 and 0.18, respectively. The p -values from analysis of variance tests for the predictors on the first five principal components for the male and female pelvis external geometry models are shown in Table 2-9. The predictors used in the analysis of variance test for the geometry models were age, BMI, and bispinous breadth. The greatest portion of variance was explained by age for the male external geometry models and bispinous breadth for the female external geometry models.

Table 2-9. *p*-values of predictors in the female and male external geometry models

Predictor		<i>p</i> -value				
		1st PC	2nd PC	3rd PC	4th PC	5th PC
Female Geometry	Age	0.004*	0.729	0.895	0.382	0.000*
	Bispinous Breadth	0.000*	0.014*	0.000*	0.015*	0.725
	BMI	0.169	0.155	0.584	0.873	0.399
Male Geometry	Age	0.007*	0.111	0.042*	0.826	0.008*
	Bispinous Breadth	0.441	0.000*	0.242	0.000*	0.959*
	BMI	0.850	0.955	0.074	0.670	0.081

* $p < 0.05$

The effects of age, bispinous breadth, BMI, and gender on pelvis geometry predicted by the pelvis parametric models are shown in Figure 2-21. These pelvis models were created by varying one parameter at a time and holding the other parameters constant. The models in these figures were aligned using a Procrustes approach rather than section centroids.

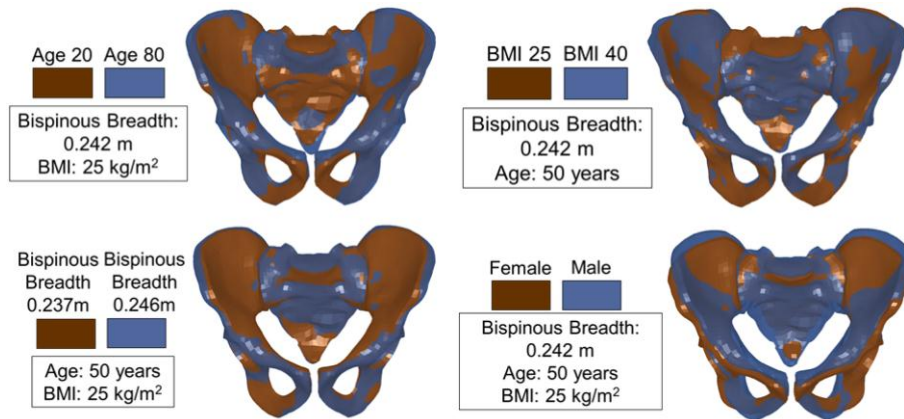


Figure 2-21. The effects of age, BMI, bispinous breadth, and gender on pelvis geometry predicted by the parametric models.

The mean distance errors and 95th percentile errors in nodal coordinate locations between the fitted meshes to the actual data and the predicted meshes were calculated, and the distributions of errors in the pelvis can be seen for both the male and female models in Figure 2-22. The larger errors occur in the symphysis region. The residuals for each model were checked for normal distributions and no trends were seen with any model predictor. The mean distance errors between observed and predicted landmark locations for a set of seven males and seven females spanning several decades of ages were determined. Male models had a mean distance error of 15×10^{-3} m, and female models had a mean distance error of 17×10^{-3} m. The largest errors occurred in the symphysis and ischium regions, and the errors were similar to the errors seen in the comparisons to the underlying dataset. An example of the landmark comparisons performed for one subject are shown in Figure 2.23, with the extracted surface shown with observed landmarks in red and predicted landmarks in blue.

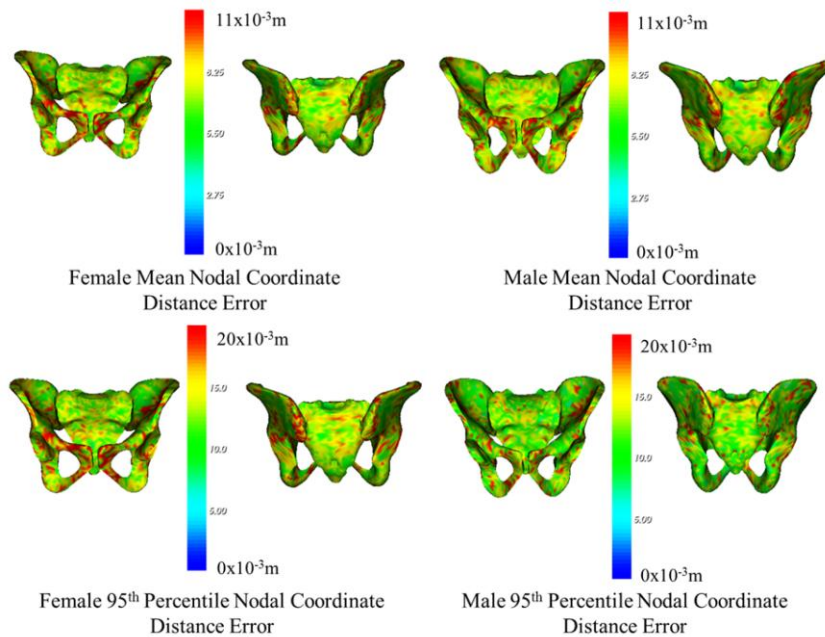


Figure 2-22. Distribution of mean and 95th percentile absolute errors in nodal coordinate locations between the actual pelvis data and predicted geometries.

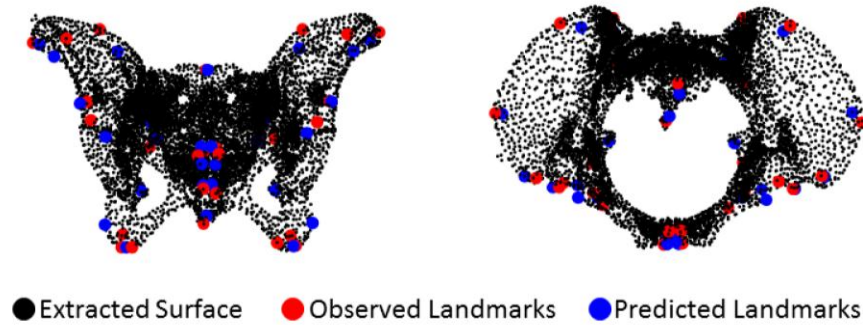


Figure 2-23. Example of the comparison between observed and predicted landmarks for a single subject from a separate set of data.

DISCUSSION

Summary

Statistical models of femur, tibia, and pelvis surface geometry and femur and tibia cross-sectional geometry were developed based on CT data and using PCAR methods to predict nodal coordinates for the associated predicted geometries. These models were used to investigate the variations in femur, tibia, and pelvis geometry with subject parameters. The statistical models describe the variance in bone shapes with a small number of variables and PCs well representing the data in orthogonal directions. The resulting statistical models are readily implemented to enable rapid generation of geometries associated with a particular set of subject characteristics since nodal coordinates are predicted by the models. Distance error distributions and thickness error distributions, as well as average midshaft errors for the femur and tibia were calculated. However, it is difficult to determine whether these values are low enough to result in FE models with reasonable performance without comparing the outputs of simulations using geometries predicted by the geometry models to experimental responses. Such a comparison is presented in the next chapter for the femur.

PCAR Models

Template pelvis, femur, and tibia meshes were morphed and fit to subject geometries, which resulted in reasonably smooth meshes to use for the femur and tibia PCAR models.

However, some individual pelvis surfaces did not result in smooth meshes. The femur and tibia fitting method used the fact that the shapes were similar to cylinders to clean out any inside faces before fitting, but the pelvis is not shaped like a cylinder and did not correctly remove inside faces for some surfaces. Eventually these surfaces will need to be remeshed to remove any inside faces. However, the PCAR analysis inherently will smooth the meshes and remove some roughness when calculating PC scores and fitting regressions to the data. The roughness is not well predicted by the regression models and is not included in the PC scores used in the models, which allows for predictions with smoother geometry than the meshes used to develop the models.

The male and female external surface geometry models for the femur and tibia better fit the underlying data than the thickness models with R^2 values of 0.77 and 0.74 vs. 0.31 and 0.36 for the femur surface and thickness male and female models, and R^2 values of 0.68 and 0.84 vs. 0.39 and 0.38 for the tibia surface and thickness male and female models. This indicates that overall sizes and shapes of the femur and tibia are substantially better predicted by subject age, bone length, and BMI, but the variations in thickness are not well explained by these predictors or geometric features captured by the geometry PC models. In addition, the inclusion of external geometry model PC scores did not result in substantial improvement in predictive ability of the thickness models. It is possible that variation in thickness could be better explained if other predictors were used, such as the presence of diseases (e.g. osteoporosis). In addition, the models can best predict the geometry at values closest to the average values of the parameters and predict geometry least well at the extreme ends of the parameter values, as is expected. Since the models are simple linear regressions, the results are not much affected by leaving out a single point, as was done in the leave-one-out cross-validation.

External surface geometry models were developed for the pelvis, but thickness models were not developed because the thickness values of cortical bone in most regions of the pelvis are lower than the resolution of the CT scans. The pelvis surface models explain less of the variance in the experimental data compared to the femur and tibia models (R^2 of 0.15 and 0.18 for male and female pelvis surface models vs. 0.77 and 0.74 for femur

and 0.68 and 0.84 for tibia surface models) because age, BMI, and bispinous breadth do not capture all of the variation in pelvis shape. However, these parameters were used for the pelvis models to provide consistent model inputs between lower-extremity bones so that only one set of subject characteristics was needed to predict all bone geometries. In addition, these parameters are the best local or whole body level predictors of geometry.

Femur length, tibia length, and bispinous breadth are used as predictors in statistical models developed in this study as surrogates for stature. Relationships between stature and bone length or bispinous breadth can be developed from existing datasets and used to reparameterize models so that stature is a predictor. However, using bone length as a predictor is advantageous as femur length or tibia length can be determined from other existing statistical models that are useful for defining geometry targets for whole-body FE models as functions of age, BMI, and stature, such as driver posture prediction models and models of external body shape (Manary et al. 1998; Reed et al. 2013). This approach of using lengths determined from statistical models of whole body posture and external body shape that are parameterized based on stature, BMI, age, and sex ensures that geometries predicted by each of the statistical models are consistent, even if the models are based on different patient/occupant populations.

The pelvis, femur, and tibia geometry could be predicted using multiple regressions without PCAR, but PCAR has several benefits. PCAR was used for three reasons: (1) the principal modes can be explored in the data set to aid in the understanding of the geometric variance, (2) the number of modes of variance (PCs) that are significantly related to potential predictors can be quantified, and (Moran et al. 2003) the orthogonality of the PCs can be exploited, along with the approximate normality of the PC scores, to generate femurs, tibias, or pelves that span a desired range of the population for future applications. In addition, PC scores were used as predictors for the femur and tibia thickness models to account for effects of outer surface geometry on bone thickness, rather than directly predicting thickness from subject descriptors. This enables an explicit linkage between geometry and thickness, even when the thickness in a particular region of the bone may not be related to overall subject descriptors.

The sample sizes used for development of the statistical models described in this chapter could be considered a limitation in the development process. However, the effects of BMI and size on geometry are generally linear, and since subjects exist on both the low and high ends of the ranges of these parameters across all age groups for all datasets, the predictions of data between these extremes is likely reasonable. In addition, the variation seen in the population can occur due to factors not covered by the parameters, regardless of the ability of the parameters to capture that variation.

Linear Mixed Models

The LMM analysis found that age, sex, stature, and BMI affect femur cross-sectional area. The effects of subject characteristics on femur geometry therefore vary by level, and these effects must be taken into account when predicting bone geometry. As was expected, both total area and cortical bone area increased with increasing stature. Total bone area also increased with increasing age, agreeing with bone literature that femur bone geometry changes with age (bones normally increase in total diameter and marrow space normally expands with aging), leading to a larger total cross-sectional area with age but weaker bones due to the change in moment with the increase in marrow space (Clarke 2008). The significant interactions between subject characteristics and location level indicate that effects need to be accounted for by models that can predict the geometry of any given set of subject characteristics, highlighting the utility of the PCAR models, which include these effects.

LMM analyses performed for the femur and tibia showed that no meaningful interactions existed between the parameters (age, BMI, bone length). In addition, a LMM analysis was not performed for the pelvis since cross-sectional areas useful in a LMM analysis did not exist. Finally, no significant interactions were found between model parameters for the pelvis in the PCAR analysis.

Model Errors

Errors in calculated femur cross-sections were determined as mean overall errors for each location considering both positive and negative values. This type of error calculation is more appropriate than using absolute errors because the models are intended to be used to generate FE models representing the entire occupant population, and average errors close to zero indicate that the models reasonably represent the population. Some models may predict higher or lower results than the average, but as long as the average error in geometry is close to zero and is unrelated to subject characteristics, the model predictions should be reasonable. These FE models will be based on the statistical model predictions and then simulations will be performed with this population of models.

Cortical thickness calculation errors were due to the inherent problem with the resolution of clinical CT scans. However, these errors did not affect the thickness values in the shafts of the femurs and tibias where thickness values were robustly calculated. An average value was used to allow for the models to have cortical bone in all locations, which is particularly important for finite-element modeling using solid elements. Since the locations of the zero values were not concentrated in one particular area in the ends of the femurs and tibias, the averaging process should not have meaningfully affected results.

Chapter III

Development and Validation of the Parametric Finite Element Models

INTRODUCTION

FE models with parametric geometry have been developed for many body regions, including some lower-extremity models (Gayzik et al. 2008; Hu et al. 2012; Li et al. 2011; Lu et al. 2013; Lu and Untaroiu 2013; Shi et al. 2014; Shi et al. 2015; Besnault et al. 1998; Bryan et al. 2010; Bryan et al. 2009; Kurazume et al. 2009; Nicolella and Bredbenner 2012). However, none of these existing models include lower extremities that are parametric with occupant characteristics. In addition, the traditional validation methods where models are compared to scaled corridors developed from normalized data are not appropriate for parametric FE models.

This chapter describes the use of the statistical models of the femur, tibia, and pelvis to generate parametric FE models of the femur, tibia, and pelvis. The parametric FE femur models were validated using the methods proposed by Hu et al. (2012). Specifically, the responses of parametric FE femur models were compared with individual male and female specimen responses from a previous study by Ivarsson et al. (2009) of the tolerance of the cadaveric femoral shaft to combined axial-compression and three-point bending. The Ivarsson data were selected because detailed information on impact response, femur geometry, and subject BMI, age, and stature were available. These validation methods serve as an example for all parametric FE lower-extremity model components since the methods of comparing experimental results with simulation results predicted based on subject-specific data can be applied for validating the parametric tibia

and pelvis models. However, studies with all relevant information for the tibia and pelvis could not be found in the previous literature.

METHODS

Parametric FE Femur Model

Parametric FE models of adult male and female femurs were developed by using existing statistical models to predict nodal coordinate locations as functions of age, BMI, and femur length and then applying these nodal coordinates to a baseline/template FE model. The statistical geometry models are described in Chapter II and by Klein et al. (2015). These models were developed by extracting femur geometry from a stratified sample of clinical CT scans of the adult population, fitting a template finite element femur mesh to the surface geometry of each subject, and programmatically determining thickness of cortical bone at each nodal location. Principal component analysis (PCA) was performed on the thickness and nodal coordinates and linear regression models were developed to predict principal component scores as functions of age, BMI, and femur length. The right femur of the Total Human Model for Safety (THUMS) 4 (Toyota Motor Corporation 2011) model was used as the template and, as a result, the statistical models directly predict target nodal locations of the parametric FE femur models.

Parametric FE Tibia and Pelvis Models

Parametric FE models of adult male and female tibias and pelvises were developed by using the existing statistical models to predict nodal coordinate locations as functions of age, BMI, and tibia length/pelvis bispinous breadth and then applying these nodal coordinates to the baseline/template FE models. The template FE tibia mesh came from the right tibia of the THUMS 4 and consists of 2,417 hexahedral elements with a total of 4,836 nodes. The template FE pelvis mesh came from the pelvis of the THUMS 4 and consists of 5,958 quad shell elements with a total of 5,956 nodes. The predicted meshes were combined with material property values from the template FE models to generate the final parametric FE tibia and pelvis models.

Femur Validation Data

Data for model validation were obtained from a study by Ivarsson et al. (2009) from which individual femur response histories and information on the subject age, sex, and size were available. In the Ivarsson et al. study, PMHS femoral shaft specimens were subjected to combined axial compression and anterior-to-posterior or posterior-to-anterior three-point bending. PMHS from which femurs were obtained for this study included nine male and four female subjects with ages between 40 and 65 years, BMI between 18 and 42 kg/m², and femur lengths from 0.430 to 0.572 m. Additional detail on these specimens is provided in Appendix B.

Figure 3-1 illustrates the setup for the Ivarsson tests. Denuded femoral shaft specimens were potted in cups that were attached to hinge joints. Bending was applied to the isolated femoral shafts by impacting at midshaft in either the anterior-to-posterior or posterior-to-anterior direction at a velocity of about 1.5 m/s. At the same time, a predetermined level of axial compressive force was applied along the long-axis of the femoral shaft by gussets whose motion was controlled by a mechanism linked to the impactor so that downward motion of the impactor caused the gussets to move toward each other. This motion of the gussets compressed a block of aluminum honeycomb; the width of the honeycomb block was varied between tests (with crush strength 4-16 kN) to control the applied force at the desired level.

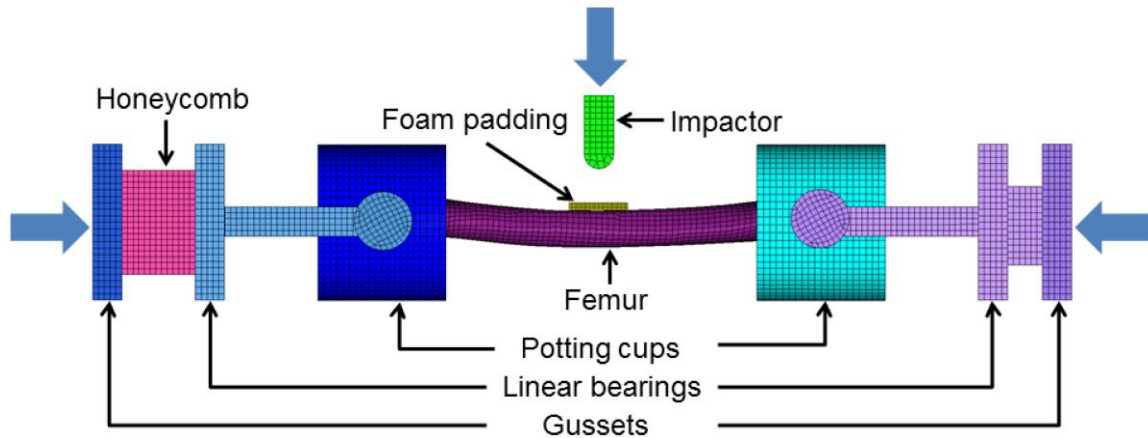


Figure 3-1. Ivarsson et al. (Ivarsson et al. 2009) test set-up with combined bending and axial compression due to the impactor and moving gussets.

Material Properties

A single femur material property was used in the validation simulations. Similar to the template femur model from THUMS 4, an elasto-plastic material definition was used (MAT_024, MAT_PIECEWISE_LINEAR_PLASTICITY). Parameters used in this model were those of the template THUMS 4 femur with the exception of the yield stress (34.5 MPa), which was outside the 100 - 150 MPa range in the literature (Burstein et al. 1976; Dokko et al. 2009). Therefore, a material optimization was performed using an FE model of the femoral shaft with the average geometry from the Ivarsson study to identify the yield stress that was associated with a predicted force history that best matched the average experimental force history. Optimization was performed using modeFRONTIER version 4.3.0 (ESTECO, Italy) and resulted in a value of 140 MPa for yield stress. This value was used in all validation simulations. All other material properties for the non-femur components in the simulations were matched to the values reported for the Ivarsson study.

Validation Simulations

The subject characteristics in the Ivarsson study were used to predict femur geometry for use in the validation simulations, using subject femur length, BMI, and age as inputs. Thirteen right femurs were predicted from the statistical model results, and twelve left

femurs were determined using a reflection of the corresponding right femurs about the long axis of the femur. As previously noted, the optimized material property (yield stress = 140 MPa) that matched the average response of all subjects was used in the simulations to remove the mean effect of material properties on loading results. The model setup used to match these tests is the same as the experimental setup shown in Figure 3-1. The measured impactor displacement histories from the tests were applied to the impactor in the simulations.

All simulations were configured in HyperMesh Version 11.0 (Altair Engineering Inc., Troy, MI) and performed using LS-DYNA version 971 (Livermore Software Technology Corporation, Livermore, CA). Impactor force histories were compared between the experimentally measured combined loading tests and the parametric simulations to assess model validity. Peak impactor forces at the time of femoral shaft fracture in the tests were compared to the parametric impactor forces at the same time. Fracture was not simulated for the parametric femur models so that the predicted forces at the time of experimental fracture could be compared to the experimental peak impactor forces. The percent errors in impactor force at the time of experimental failure between the tests and the simulations were calculated using Equation 1, and the percent differences in the slope values of the force histories between the tests and simulations were also determined. The slope values of the force histories were calculated by fitting a straight line using linear regression between the time at 5% of peak experimental force and the time at 95% of peak experimental force for both experimental and model predicted data, and then using the slope of this fitted line.

$$\text{Percent error} = (\text{Simulation} - \text{Test}) / \text{Test} * 100\% \quad (1)$$

Trends in the experimental peak forces and the forces predicted by the FE models at the time of experimental fracture with age, BMI, and femur length were characterized using linear mixed models (LMM). LMMs were used to account for the reduction in variance associated with using right and left femurs from the same subjects in different test conditions. Effect estimates from the LMM analysis for the model predicted dataset were

compared to the mean and 95% confidence intervals predicted in the LMM analysis on the experimental dataset to assess how well the predicted data matched trends in the experimental data. Due to the small number ($n = 8$) of female femurs, only the male femurs were used in the LMM analysis to characterize trends.

RESULTS

Parametric FE Models Development

The parametric FE femur models generated from the previously developed statistical models consist of 3,060 hexahedral elements with a total of 6,124 nodes each. The mesh quality for the parametric models was minimally affected by the morphing process. The minimum Jacobian value for the template THUMS 4 femur was 0.38, and this value was used to evaluate the mesh quality for the predicted femurs based on the Ivarsson data. Approximately 5% of all the elements for each femur fell below the 0.38 level. The majority of these elements were located at the ends of the femurs (in the femoral head, neck, and condyles). Since the ends of the femur were potted in the simulations, the minimum Jacobian value was calculated for the shaft of each femur. The average of the minimum Jacobian in the shaft for each subject was 0.25 (range 0.20-0.31).

Validation Simulations

The average error in peak force predicted by the parametric models was 5%, and the average error for the 17 male models was 4%, while the average error for the 8 female models was 8%. The average slope for the experimentally measured results was -472 kN/s, and the average slope for the parametric results was -471 kN/s. The average difference in slope values for the right and left parametric femurs was -1%, and the average difference for the male models was -2%, while the average difference for the female models was 1%.

A typical comparison of predicted and measured force histories is shown in Figure 3-2. The times at 5% and 95% of the peak force experimental fracture are indicated. Figure 3-

3 compares the peak impactor forces and slopes for the experimental values and the values predicted by the parametric models. The R^2 value for the force values was 0.632 and the R^2 value for the slope values was 0.638. The values for peak forces and slopes and the average and absolute errors in peak forces and slopes for each parametric model simulation are provided in Appendix C and the resulting impactor force histories for the experiments and the simulations are provided in Appendix D.

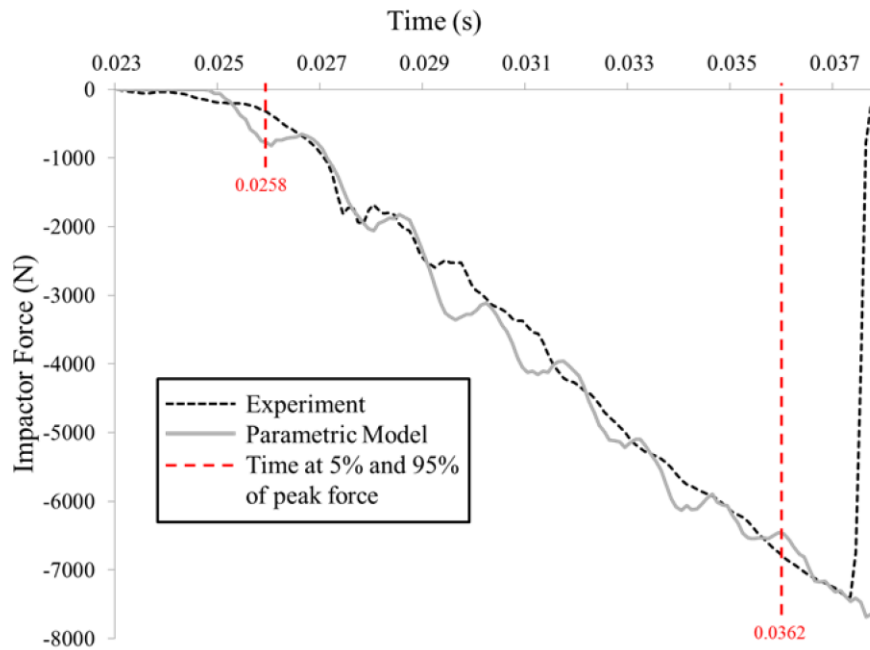


Figure 3-2. Example of impactor force history from an experimental result compared to impactor force results from a simulation with the parametric model.

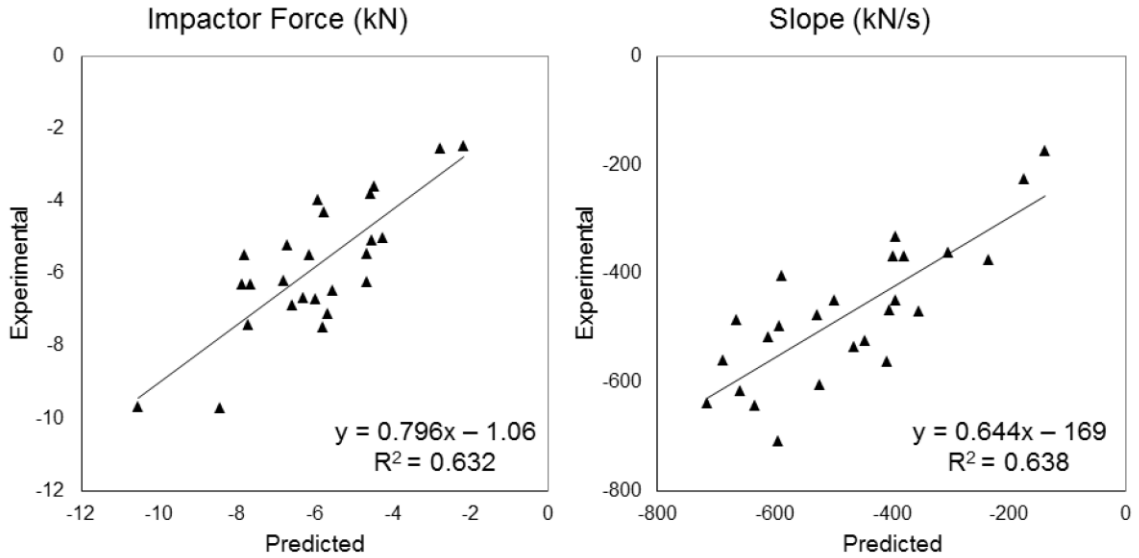


Figure 3-3. Comparison between the peak impactor forces (left) and slope values (right) for the experimental values and values predicted by the parametric models.

The effect estimates generated when LMM analysis was used to fit the same set of parameters to the experimentally measured peak force and the predicted force at the time of experimental fracture are shown in Table 3-1. All parameters used in the parametric models were included in the LMM analysis and the 68% confidence intervals for the LMM results on experimental data are also given. 68% confidence intervals were used to consider an interval of plus or minus a standard deviation, which indicates that the models are not statistically different. Model estimates all fall within the experimental confidence intervals, indicating that the male parametric femur model reproduces trends present in the experimental dataset.

Table 3-1. Linear mixed models analysis results for male experimental and model predicted results

Effect	Experimental Coefficient Estimate	68% Confidence Interval ($\pm 1\sigma$) on Experimental Estimate	Model Coefficient Estimate
Intercept	-24.0	(-33.7, -14.4)	-25.0
Age	0.183	(0.116, 0.249)	0.0852
Femur Length	0.0286	(0.0140, 0.0431)	0.0390
BMI	-0.265	(-0.321, -0.208)	-0.229

DISCUSSION

Summary

Parametric FE models of the femur, tibia, and pelvis were developed in this chapter. The parametric FE femur models were validated by performing simulations of combined compression and bending tests of the femoral shaft from a previous study. These tests were used for validation because sufficient information was available to effectively characterize specimen geometry and because the applied force histories were available for all tests. Impactor forces from simulations, on average, matched well to experimental values at the time of failure with an average error of 5% across the 25 validation simulations. In addition, the simulations were able to match the trends in the experimental dataset. However, there was substantial variation between predicted and measured peak forces between subjects, likely because the parametric femur model does not exactly predict the geometry of any specimen and because average material properties were used in all validation simulations. This suggests that the parametric femur models should be used in simulations aimed at understanding the response of a population rather than predicting the response of any individual, at least until data on how material properties vary with model predictors (in particular age and gender) are available. Specifically, the parametric models should be used to generate a set of FE models associated with occupant characteristics that span the population and the simulation results should be weighted based on the exposure of the subset of occupants represented by the model to motor-vehicle crashes.

Validation Simulations

Only one set of femur data was used for validation because this dataset is the only study known to include the information on subject characteristics and the response histories needed for subject-specific validation. This dataset has a small range of ages (40-65 years), but the parametric models were able to reproduce the trends present in the experimental dataset with subject characteristics for male femurs. More validation data

will be needed in the future, but this validation method follows the paradigm proposed by Hu et al. (2012) for validating parametric models.

While the male parametric femur model reproduced trends present in the experimental dataset, each individual subject may not have fit the experimental results. Subjects with characteristics at the extremes of the ranges used to develop the models, such as a very small stature, may not have fit as closely as those with characteristics near the averages. These types of results are acceptable according to the Hu et al. (2012) methods for validation, as long as the models are able to match the trends overall, as was the case for the validation simulations.

The only validation simulations performed here were for the male and female femur FE models. Similar types of validation simulations could be performed for the pelvis and tibia, but no studies were found that have the necessary level of detail about the specimens for complete parametric model validation. In addition, more data is needed in the studies that describe testing with the entire lower extremities before validation simulations can be performed for the lower extremities.

Material Properties

Although it is well established that material properties vary between specimens and as a function of age (Clarke 2008), material properties were not varied in the validation simulations. Excluding the effects of specimen characteristics on material properties can result in errors in model predictions. For example, force at failure could increase with increasing age if material properties are not varied instead of force decreasing with increasing age. Despite this possibility, a single average material property was used in validation simulations as this approach allowed geometry effects to be compared and because the age range in the experimental dataset used for validation was relatively small.

The average material properties used in the validation simulations have an effect on the error seen in the results. The average material property was used to consider only the effect of geometry (and thus the error in geometry) in the simulation results, but the

choice for average material property values has an effect as well. Eventually improved material models will be needed so that less error will be seen in the simulations.

Future Work

The models developed here are an important step toward developing a parametric FE model of the entire lower extremities that can be used to improve understanding of the effects of age, gender, and BMI on the likelihood, location, and severity of lower-extremity injuries in frontal crashes. Future work will involve additional validation of the femoral head, neck, and condyles. However, these validation simulations require studies with the necessary subject characteristics and response histories, which are not yet available in the scientific literature. In addition, material properties that are parametric with occupant characteristics should be included in future simulations with the parametric models. Specifically, future work should consider relationships between bone density and material properties when developing parametric material models as such relationships have been used to determine material properties for previous FE models (e.g., Bredbenner et al. 2014; Keaveny et al. 2008; Keyak and Falkinstein 2003).

Chapter IV

Application of the Parametric Whole-body Models

INTRODUCTION

The relative contributions of the hypothesized reasons for the effects of age, sex, and BMI on LX injury in frontal crashes described in Chapter I can best be assessed using a parametric FE model. This FE model needs to have skeletal geometry, external surface geometry, posture, and material properties that can be varied with occupant characteristics. The development and application of techniques to generate male and female whole-body parametric FE models using the parametric FE pelvis, femur, and tibia models described in Chapters II and III and an external body surface shape model previously developed at UMTRI is described in this chapter. These parametric FE models were whole-body FE models with geometry that spans a range of occupant age, BMI, and stature combinations for both men and women. This set of models was used in frontal impact simulations to begin to explore the effects of variations in occupant characteristics on lower-extremity injury.

METHODS

Overview

Male and female parametric whole-body models were developed by combining the femur, tibia, and pelvis models described in Chapters II and III with an existing model of

external body surface shape using methods adapted from Hwang et al. (2014). Figure 4-1 shows the process used to combine these models and to generate FE model geometry associated with a target set of occupant age, stature, and BMI. Landmarks from the external body surface shape model that corresponded to landmarks from the skeletal component models were used to link and position the bones inside the predicted external body surface shape. The other skeletal components and the soft tissues were then morphed using a thin plate spline RBF using the external surface and femur, tibia, and pelvis models as boundaries. The resulting whole-body model consists of target external surface geometry, target pelvis, femur, and tibia geometry, morphed other skeletal components and soft tissue, and material properties. The external body surface shape model was developed using principal component analysis and regression analysis with age, BMI, stature, and sex predicting the external body surface, external surface landmarks, and joint landmarks. The lower half of the body (below the diaphragm) used the predicted external body surface and predicted parametric pelvis, femurs, and tibias as morphing targets. The upper half of the body (above the diaphragm) was only morphed based on the external surface since the focus of this work is on the lower extremities.

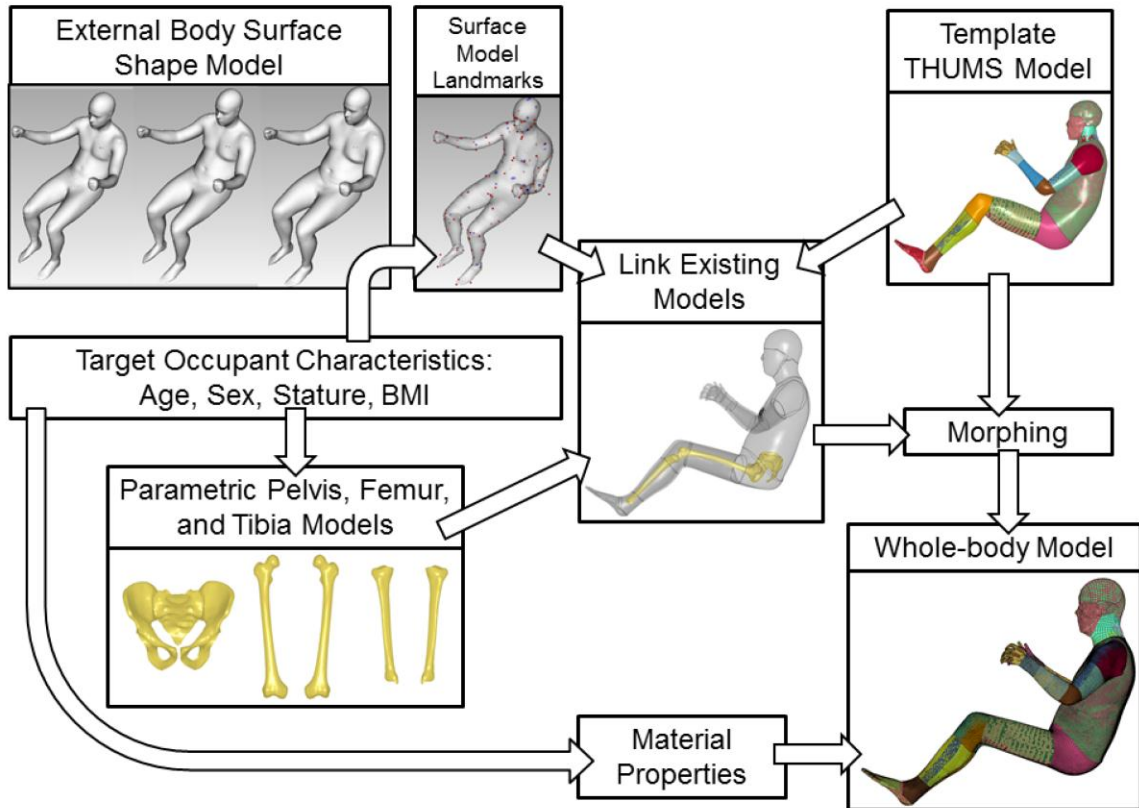


Figure 4-1. Flowchart of the process for developing a whole-body model with target geometry and material properties from statistical geometry and material models and a template mesh.

Parametric Whole-body Model Development

For development of a parametric whole-body model, femur length was defined as the distance between the center of the femoral head and the midpoint of the femoral epicondyles. This allowed the joint landmark locations predicted by the external body shape model to be used to align the femur inside the surface model. The new definition of femur length is shown in Figure 4-2.

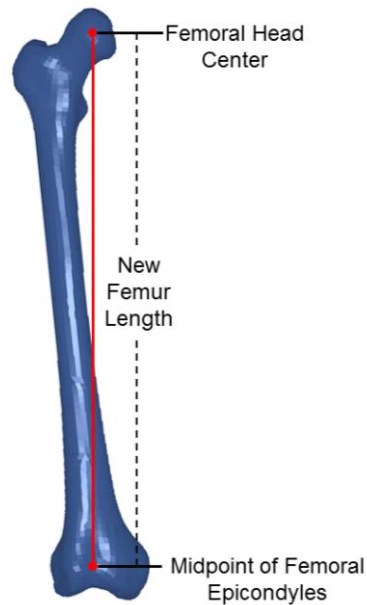


Figure 4-2. Femur length defined as the Euclidean distance between the center of the femoral head and the midpoint of the femoral epicondyles.

The steps used to develop the male and female parametric whole-body models are listed below.

- Input age, stature, BMI, and sex.
- Calculate bispinous breadth using regression equations for men and women, given in Equations 1 and 2, that predict bispinous breadth as a function of stature.

$$\text{Bispinous breadth (Male)} = 0.176 + 0.0371 * \text{Stature (m)} \quad (1)$$

$$\text{Bispinous breadth (Female)} = 0.0864 + 0.0852 * \text{Stature (m)} \quad (2)$$

- Predict body surface shape using age, stature, BMI, and sex using existing surface model. Examples of predicted body surface shapes are shown in Figure 4-3. Then morph template external THUMS surface to predicted body surface shape.

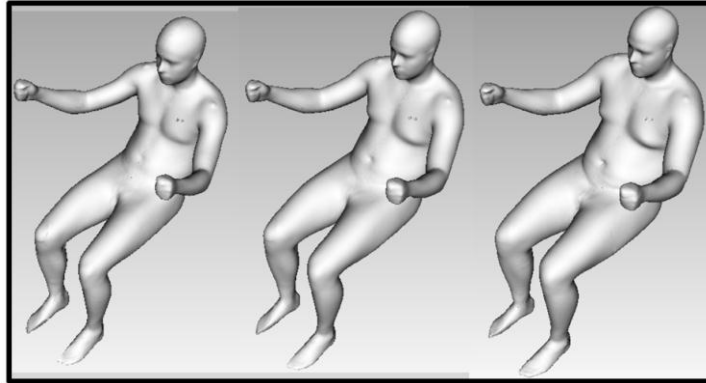


Figure 4-3. Examples of small, midsize, and large male body surface shapes predicted by the external body surface shape model.

- Use landmarks from surface model to calculate femur length and tibia length to use for predicting femur and tibia models. The lengths determined from the surface model are shown in Figure 4-4.

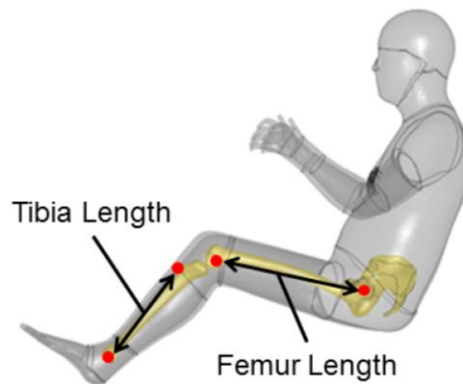


Figure 4-4. Femur and tibia length determined from landmark locations predicted by the external body surface shape model.

- Predict parametric pelvis, right femur, and right tibia using existing pelvis, femur, and tibia models described in Chapters II and III.
 - Reflect predicted right femur and predicted right tibia along y-axis to get predicted left femur and predicted left tibia since the template THUMS is symmetric.
- Position parametric pelvis, femur, and tibia inside morphed external surface model.
 - Calculate landmarks for predicted pelvis, femur, and tibia corresponding to landmarks from morphed THUMS bones based on predicted surface model (template THUMS bones are morphed based on morphing of external surface to determine target landmarks for positioning). The specific landmarks used for the positioning include pelvis ASIS, PSIS, and L5S1, femoral head center and lateral and medial epicondyles, and tibia medial malleolus and ankle joint location. All landmarks are listed in Hwang et al. (2014) and the ASIS, PSIS, femoral head center, lateral

epicondyle, tibial tuberosity, and medial malleolus are shown in Figure 4-5.

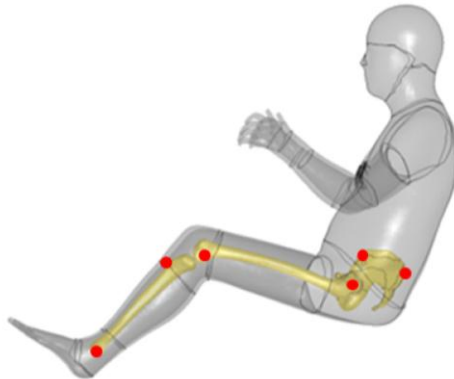


Figure 4-5. Landmarks used to position the pelvis, femur, and tibia.

- Use singular value decomposition (SVD) (Weisstein 2015) and distance minimization to align the predicted pelvis with the original pelvis. An example of this process is shown in Figure 4-6.

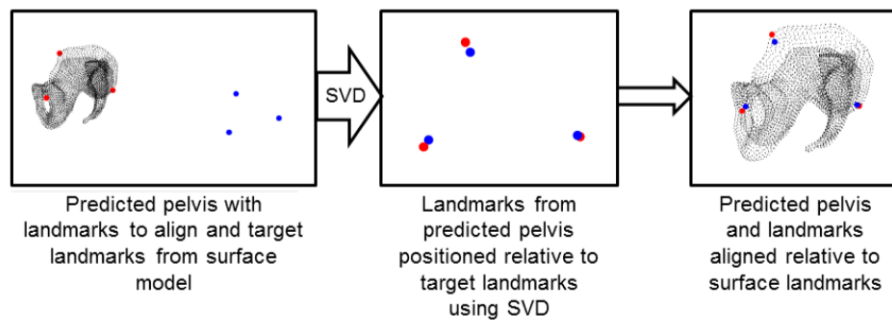


Figure 4-6. Example of process for positioning the predicted bones inside the external surface using SVD.

- Align predicted femurs using SVD and distance minimization. Repeat for left femur.
- Align the predicted right tibia using SVD and distance minimization. Repeat for left tibia.
- Morph femur and tibia trabecular bone to match predicted and aligned right and left femurs and tibias. Figure 4-7 shows trabecular bone inside the right femur.

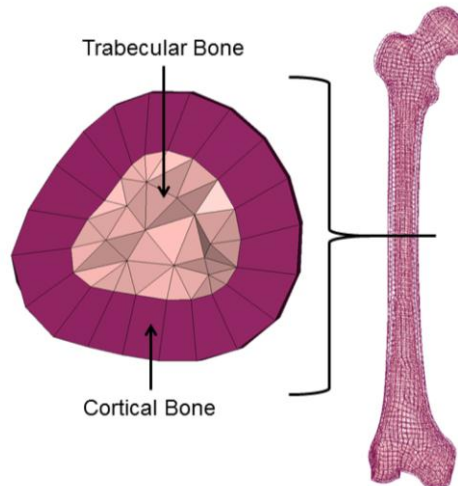


Figure 4-7. Morphed trabecular bone inside the right femur.

- Divide whole body into segments for morphing of soft tissues between bones and the external body surface. An example of the three body segments for the right leg is shown in Figure 4-8.



Figure 4-8. Three segments for right leg.

- Morph nodes in the shared surfaces between segments of body.
 - Shared surfaces include: pelvis-upper body, thorax-right arm, thorax-left arm, upper-lower, pelvis-right thigh, pelvis-left thigh, right thigh-right knee, left thigh-left knee, right knee-right lower leg, left knee-left lower leg.
- Morph each segment of the whole-body beginning with the lower half of the body and then the upper half of body. The two halves are split by the diaphragm.
 - Use shared areas, pelvis, femurs, tibias, and external body surface as targets.
- After morphing is complete, update all nodes in new file.
- Export node IDs and nodal coordinates.

- This exported file is then included in the template file with all other model definitions, such as material properties. An example of the morphed model is shown in Figure 4-9.

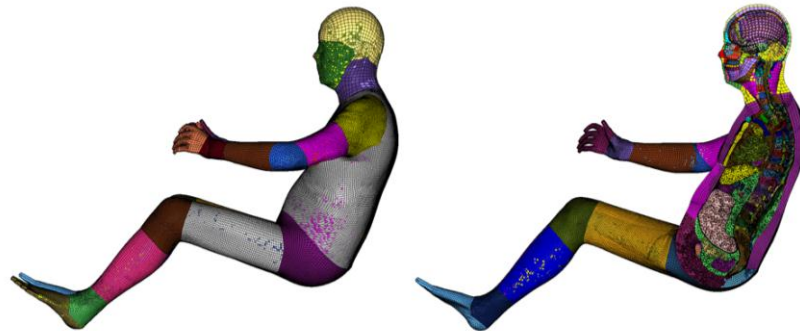


Figure 4-9. An example of the morphed whole-body model.

Examples of male and female morphed whole-body models are shown in Figure 4-10. A table of 27 male and 27 female morphed models with three levels each for age, BMI, and stature to show the ranges of occupant characteristics is provided in Appendix E. The levels include ages 20, 50, and 75 years for age; BMI values of 25, 30, and 35 kg/m²; and statures of 5th, 50th, and 95th percentile statures for men and women (1.636, 1.763, and 1.887 m and 1.507, 1.622, and 1.731 m, respectively).

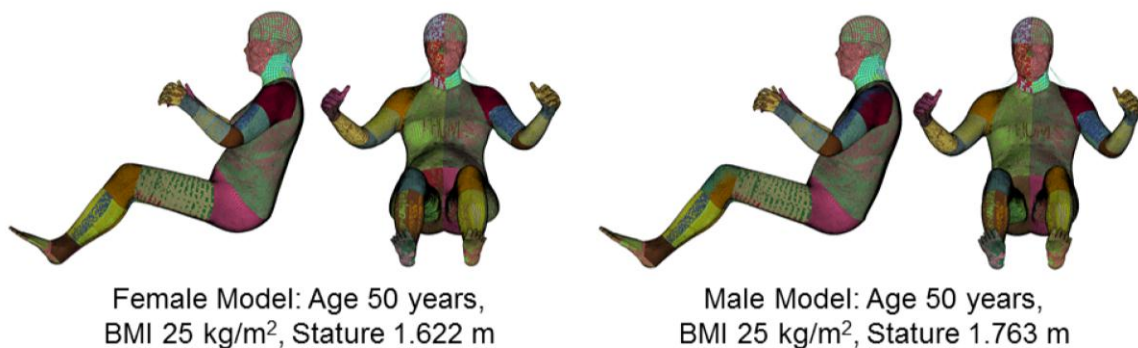


Figure 4-10. Female and male morphed whole-body model examples.

Parametric Whole-body Model Application Simulations

A series of simulations was performed with the whole-body models inside a single vehicle package representing a midsize sedan using the set-up shown in Figure 4-11.

This simulation set-up represents a frontal crash with deltaV or ΔV (total change in vehicle center of gravity velocity over the duration of the crash event) of 56 kph. The boundary conditions and vehicle package parameters were from a validated model provided by General Motors to represent the 56 kph deltaV, but each whole-body model had to be positioned and set up in the simulation. A partial factorial design of experiments was used to select 12 male models and 12 female models with three levels for each of the three parameters of age, BMI, and stature determined from the 27 male and 27 female models described above. The Uniform Latin Hypercube method was used to select 12 male models and 12 female models to use for the simulations to represent the entire 27 male and 27 female models generated. 24 simulations were performed out of 54 total possible simulations to limit the time needed. Table 4-1 lists the 24 sets of subject characteristics used to predict the whole-body models. A table with all 54 sets of occupant characteristics is provided in Appendix F. The three levels for each parameter included ages of 25, 50, or 75 years, BMI of 25, 30, or 35 kg/m², and statures of 5th, 50th, or 95th percentile for men and women. The minimum age of 25 was chosen because there was limited data below this age on which to base the models. The age of 50 was chosen because it is the highest age before the risk of osteoporosis increases, thus having an effect on bone material properties (National Osteoporosis Foundation). The maximum age of 75 was chosen because it is the age at which fatal crash rates start increasing for the elderly population (defined as 65 or older by the CDC). The minimum BMI value was chosen because the baseline model has a BMI of 25, and the larger values were chosen to consider the effects of obesity since larger BMI has been shown to have an effect on lower-extremity injury risk. The stature ranges were chosen because they span the three sizes of crash test dummies (5th percentile female, 50th percentile male, and 95th percentile male) and the 5th percentile to 95th percentile choices for both sexes considers the range in the population.

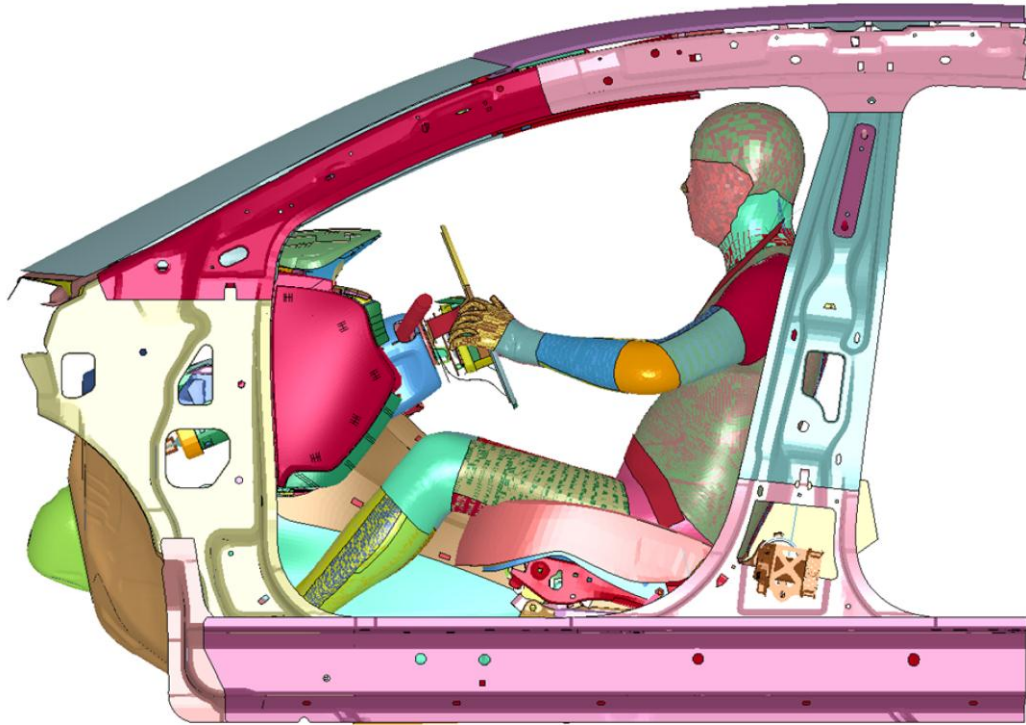


Figure 4-11. Simulation set-up.

Table 4-1. Subject characteristics used for simulations

Female Models				Male Models			
Female Test ID	Age (years)	BMI (kg/m ²)	Stature (m)	Male Test ID	Age (years)	BMI (kg/m ²)	Stature (m)
F1	25	25	1.507	M1	25	25	1.636
F4	25	30	1.507	M4	25	30	1.636
F7	25	35	1.507	M7	25	35	1.636
F9	25	35	1.731	M9	25	35	1.887
F11	50	25	1.622	M11	50	25	1.763
F15	50	30	1.731	M15	50	30	1.887
F17	50	35	1.622	M17	50	35	1.763
F18	50	35	1.731	M18	50	35	1.887
F19	75	25	1.507	M19	75	25	1.636
F20	75	25	1.622	M20	75	25	1.763
F23	75	30	1.622	M23	75	30	1.763
F24	75	30	1.731	M24	75	30	1.887

The fore-aft and vertical positions of the 24 models were set relative to the vehicle seat using hip locations predicted by a statistical posture-prediction model developed by Reed et al. (2002) that used stature, sitting height, and BMI, as well as vehicle package factors to predict posture including hip joint center location. Equations 3a and 3b give the regression equations adapted from Reed et al. and used in this work with constant values

used for vehicle package factors. For simplicity, and because it was unlikely to meaningfully affect lower extremity responses in frontal crashes, the vehicle seat was set to the same fore-aft position in all simulations. When using the posture prediction model, sitting height was determined using a sitting height to stature ratio of 0.52, which is the average value in the population (ANSUR II report).

$$HJC_x = -0.1315 + S * 0.0000482 - BMI * 0.002677 + 0.005 * C \quad (3a)$$

Where, HJC_x is the hip joint center location along the X axis (fore-aft, with positive being fore), S is stature in m, BMI is body mass index in kg/m^2 , and C is cushion angle in degrees, which was held constant at 14.5° for this study.

$$HJC_z = -0.1434 + BMI * 0.002009 + 0.0007 * H + 0.0001375 * SWBoF + 0.00049 * C \quad (3b)$$

Where HJC_z is the hip joint center along the Z axis (with positive being upward), H is the sitting height determined using $0.52 * Stature$, and SWBoF is the steering wheel to ball of foot distance calculated using a steering wheel diameter of 0.541 m and a seat height of 0.255 m in this study.

For each model, pre-simulations were used to position the hands and right foot on the steering wheel and pedal, respectively. In these pre-simulations, the hands, arms, and right leg were allowed to move and the rest of the body was set as rigid so that the position relative to the seat did not change.

Following each pre-simulation, the seatbelt was fit to the model's external body surface shape. The belt fitting process was based on a statistical model of seat belt fit developed by Reed et al. (Reed et al. 2013) that predicts the locations of the lap belt and shoulder belt. The lap belt location is predicted in a sagittal plane passing through the left anterior superior iliac spine (ASIS) landmark of the pelvis as a function of age, stature, BMI, and belt angle for the x-coordinate and as a function of BMI only for the z-coordinate.

Equations 4a and 4b give the statistical models used to determine the x and z locations of

the lap belt. Age, BMI, and stature were used to predict the location of the belt relative to the left ASIS of the pelvis using the same belt angle of 75 degrees from the vehicle set-up for each whole-body models. The location of the belt relative to the right ASIS was also predicted using the model assuming the same location in two dimensions as the left ASIS. The shoulder belt was fit to a corresponding location on the chest for each whole-body model rather than using the statistical model since the focus was on variations in lower-extremity response. An example of the seatbelt fit is shown in Figures 4-12 and 4-13.

$$LB_x = 0.156 + 0.000297*L - 0.0003*A - 0.00512*BMI - 0.00004*S \quad (4a)$$

Where LB_x is the lap belt position relative to the ASIS in the X axis in m, L is the lap belt angle, which was 75 degrees in this study, A is age in years, BMI is body mass index in kg/m^2 , and S is stature in m.

$$LB_z = -0.0701 + 0.0047*BMI \quad (4b)$$

Where LB_z is the lap belt position relative to the ASIS in the Z axis in m.

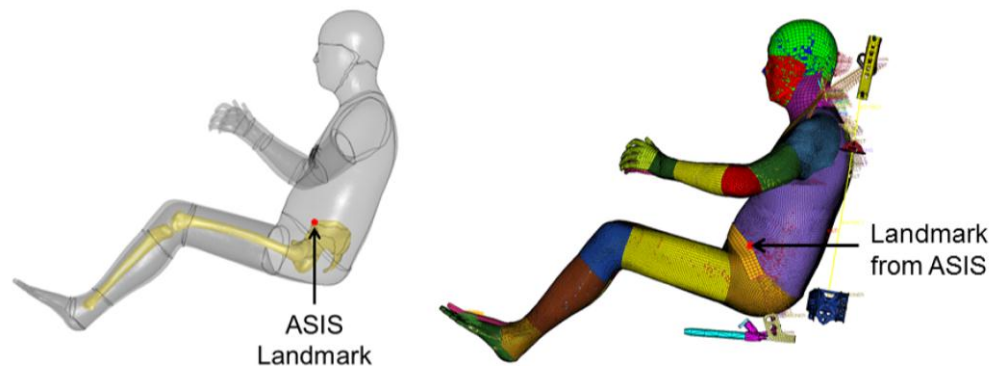


Figure 4-12. Seatbelt fit determined from ASIS landmark.

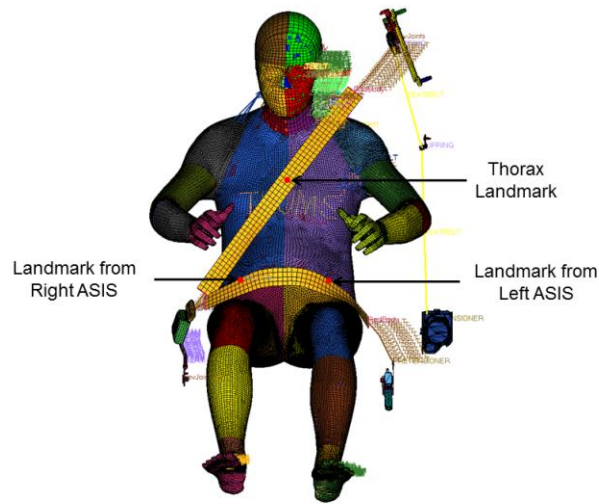


Figure 4-13. Seatbelt fit determined from ASIS landmarks and thorax landmark.

Material Properties

Femur and pelvis material properties were varied to account for the reported decrease in yield stress and Young's Modulus with increasing age based on Equations 5 and 6.

These equations were developed using data reported in the meta analysis performed by Dokko et al. (2009).

$$\text{Young's modulus (GPa)} = -0.06 * \text{age} + 18 \text{GPa} \quad (5)$$

$$\text{Yield stress (MPa)} = -0.16 * \text{age} + 136 \text{MPa} \quad (6)$$

The effects of age on the modulus and yield stress in the tibia were incorporated in the parametric tibia model by scaling Equations 7 and 8, using the scale factors shown in Equations 5 and 6. These scale factors were determined from previously published data (Burstein et al. 1976; Dokko et al. 2009).

$$\text{Young's modulus scale factor} = 1.23 \quad (7)$$

$$\text{Yield stress scale factor} = 1.27 \quad (8)$$

Simulation Outputs

To compare the effects of age, BMI, and stature on lower-extremity injury risk, several outputs were determined, including principal strain values for the pelvis, right and left femur, and right and left tibia, and contact forces at the knees, hips, and distal tibias. The maximum principal strain values in the pelvis, right and left femurs, and right and left tibias were determined and were normalized using the ultimate strain values determined for each age group to be able to compare a predictor of injury across the age groups. Equation 9 was used to determine the ultimate strain value for the femur and pelvis based on data reported by Dokko et al. (2009), and the tibia value was scaled using Equation 10. A multivariate regression was performed for each bone with age, BMI, and stature as the predictors to determine if these characteristics had a significant effect ($p < 0.05$) on the ratio of predicted strain to ultimate strain, or normalized strain. In addition, a multivariate linear regression was performed for the forces at the knees, hips (proximal femurs), and distal tibias with age, BMI, and stature as the predictors to determine if these characteristics had a significant effect ($p < 0.05$) on force results for the male and female simulations. The effects of age, BMI, and stature were also assessed by determining kinematics of the belt relative to the spine in the simulations.

$$\text{Ultimate strain} = (-0.0087 * \text{age} + 2) / 100 \quad (9)$$

$$\text{Ultimate strain scale factor} = 1.08 \quad (10)$$

RESULTS

Parametric Whole-body Model Development

Similar to the baseline THUMS models, each morphed model had a total of 1,313,685 solid elements and 395,024 shell elements. The minimum solid element Jacobian value for the baseline THUMS model was 0.25 and the minimum shell element Jacobian was 0.28 for the baseline model. These values were used to compare to the parametric models, and the results are shown in Tables 4-2 and 4-3. Some of the models had bad elements in which the Jacobian value was less than zero, especially the shortest and

thinnest female models with a stature of 1.507 m and a BMI of 25 kg/m². These elements were fixed prior to simulations by either translating some of the nodes of the element to obtain positive Jacobian values or by deleting a small area of elements where the bad values occurred. The minimum Jacobian values listed in Tables 4-2 and 4-3 were the values for the set of 24 models used in the simulations.

Table 4-2. Female mesh quality results after the morphing process

Female Test ID	Min. Solid Element Jacobian	Num. Solid Elements < 0.25	% Solid Elements < 0.25	Min. Shell Element Jacobian	Num. Shell Elements < 0.28	% Shell Elements < 0.28
F1	0.01	43	0.00327	0.00	3	0.00076
F2	0.05	5	0.00038	0.28	0	0.00000
F3	0.24	2	0.00015	0.28	0	0.00000
F4	0.16	11	0.00084	0.25	3	0.00076
F5	0.22	2	0.00015	0.27	4	0.00101
F6	0.23	1	0.00008	0.28	0	0.00000
F7	0.19	11	0.00084	0.18	3	0.00076
F8	0.19	3	0.00023	0.20	4	0.00101
F9	0.17	4	0.00030	0.22	2	0.00051
F10	0.03	16	0.00122	0.28	0	0.00000
F11	0.17	5	0.00038	0.28	0	0.00000
F12	0.26	0	0.00000	0.28	0	0.00000
F13	0.22	4	0.00030	0.27	2	0.00051
F14	0.27	0	0.00000	0.28	0	0.00000
F15	0.24	1	0.00008	0.28	0	0.00000
F16	0.22	7	0.00053	0.20	2	0.00051
F17	0.20	1	0.00008	0.22	2	0.00051
F18	0.17	2	0.00015	0.24	2	0.00051
F19	0.03	26	0.00198	0.28	0	0.00000
F20	0.23	2	0.00015	0.28	0	0.00000
F21	0.24	2	0.00015	0.28	0	0.00000
F22	0.23	7	0.00053	0.27	2	0.00051
F23	0.25	0	0.00000	0.28	0	0.00000
F24	0.24	2	0.00015	0.28	0	0.00000
F25	0.23	4	0.00030	0.22	3	0.00076
F26	0.21	1	0.00008	0.24	2	0.00051
F27	0.17	10	0.00076	0.26	2	0.00051

Table 4-3. Male mesh quality after the morphing process

Male Test ID	Min. Solid Element Jacobian	Num. Solid Elements < 0.25	% Solid Elements < 0.25	Min. Shell Element Jacobian	Num. Shell Elements < 0.28	% Shell Elements < 0.28
M1	0.07	8	0.00061	0.11	3	0.00076
M2	0.25	0	0.00000	0.28	0	0.00000
M3	0.25	0	0.00000	0.28	0	0.00000
M4	0.22	2	0.00015	0.25	2	0.00051
M5	0.25	0	0.00000	0.27	2	0.00051
M6	0.26	0	0.00000	0.28	0	0.00000
M7	0.01	21	0.00160	0.12	5	0.00127
M8	0.09	4	0.00030	0.25	2	0.00051
M9	0.15	5	0.00038	0.27	2	0.00051
M10	0.10	6	0.00046	0.27	2	0.00051
M11	0.24	1	0.00008	0.28	0	0.00000
M12	0.25	0	0.00000	0.28	0	0.00000
M13	0.24	2	0.00015	0.26	2	0.00051
M14	0.25	0	0.00000	0.27	2	0.00051
M15	0.25	0	0.00000	0.28	0	0.00000
M16	0.01	22	0.00167	0.21	5	0.00127
M17	0.21	4	0.00030	0.26	2	0.00051
M18	0.09	7	0.00053	0.24	2	0.00051
M19	0.11	8	0.00061	0.28	0	0.00000
M20	0.24	2	0.00015	0.28	0	0.00000
M21	0.24	1	0.00008	0.28	0	0.00000
M22	0.23	4	0.00030	0.26	2	0.00051
M23	0.24	2	0.00015	0.28	0	0.00000
M24	0.14	2	0.00015	0.22	3	0.00076
M25	0.03	12	0.00091	0.23	3	0.00076
M26	0.23	2	0.00015	0.26	2	0.00051
M27	0.02	15	0.00114	0.27	2	0.00051

Parametric Whole-body Model Application Simulations

Male Strain Results

Table 4-4 gives the resulting normalized strains for each model for the femurs, tibias, and pelvis from the male simulations. For the male simulations, BMI was significant for the right femur, age and BMI were significant for the left femur, and age was significant for the pelvis. For the femurs, an increase in age from 25 to 75 years and BMI from 25 to 35 years caused an increase in the normalized strain while holding other parameters constant, indicating that older and higher BMI occupants will have larger strain values in the femur. For the pelvis, an increase in age from 25 to 75 years caused an increase in the normalized strain while holding other parameters constant, indicating that older

occupants will have larger strain values in the pelvis. The coefficient values for each parameter for the linear multivariate regression equations determined for the right femur, left femur, and pelvis are given in Table 4-5.

Table 4-4. Male model normalized strain results

Male Test ID	Right Tibia	Left Tibia	Right Femur	Left Femur	Upper Pelvis Surface	Lower Pelvis Surface
M1	0.211	0.424	0.142	0.176	0.489	0.499
M4	0.254	0.530	0.148	0.181	0.439	0.455
M7	1.428	1.272	0.249	0.370	0.433	0.439
M9	0.329	0.366	0.230	0.277	0.314	0.276
M11	0.267	0.498	0.162	0.283	0.388	0.399
M15	0.355	0.445	0.261	0.292	0.528	0.423
M17	0.447	0.309	0.258	0.337	0.369	0.447
M18	0.307	0.513	0.408	0.373	0.327	0.314
M19	0.302	0.556	0.148	0.270	0.491	0.577
M20	0.316	0.637	0.203	0.341	0.976	1.189
M23	0.482	0.428	0.236	0.417	1.194	1.218
M24	0.595	0.678	0.317	0.452	0.586	0.722

Table 4-5. Coefficient values for each parameter for the male linear multivariate regression equations determined for the right femur, left femur, and pelvis

	Intercept	Age Coefficient	BMI Coefficient	Stature Coefficient
Right Femur	-0.692	0.001	0.012	0.0002
Left Femur	-0.386	0.003	0.010	0.0001
Pelvis	1.363	0.011	-0.004	-0.0007

Figure 4-14 shows the distributions of normalized strain in the right femur for BMI, the left femur for BMI and age, and the pelvis for age for the male models. Only the parameter indicated was allowed to vary in these plots since the other values were held constant at the middle value from the ranges. Figures 4-15a, 4-15b, 4-15c, and 4-15d show the changes in the distributions for principal strain for the right femur for BMI, the left femur for BMI and age, and the pelvis for age for the male models. The male model with age 25 years, BMI 25 kg/m², and stature 1.636 m had normalized strain values that exceeded the ultimate strain value in tension in a contiguous group of elements in the right and left tibias, indicating the prediction of tibia fractures. The locations of both of these fractures were along the inferior lateral edge of the bones. In addition, the male

subjects with age 75 years, BMI 25 kg/m², and stature 1.763 m and age 75 years, BMI 30 kg/m², and stature 1.763 m had strain values in the pelvis that exceeded the ultimate strain values. The locations predicted for fracture in both of these subjects were along the edge of the left acetabulum.

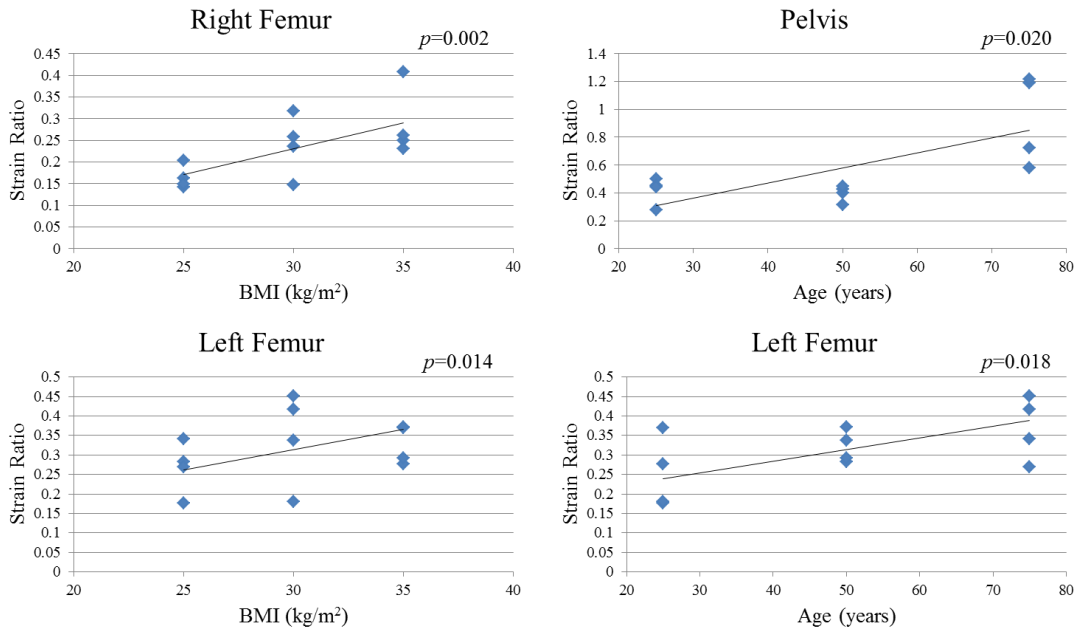


Figure 4-14. Distributions of normalized strains for the right femur with BMI (top left), the pelvis with age (top right), the left femur with BMI (bottom left), and the left femur with age (bottom right).

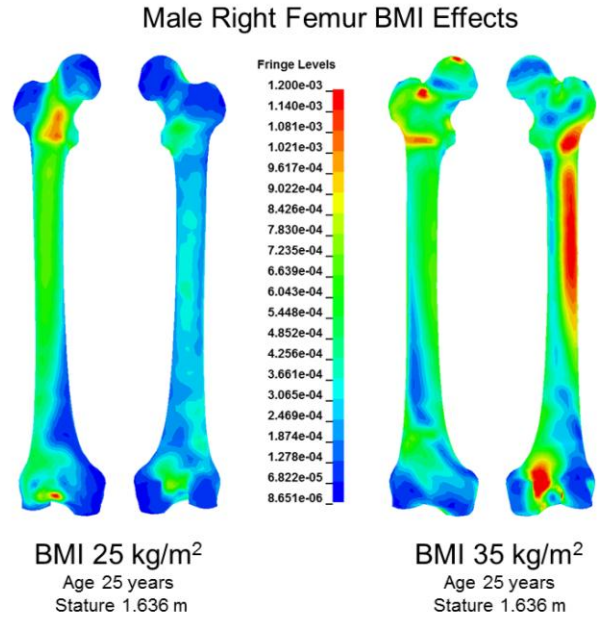


Figure 4-15a. Change in distributions of principal strain with BMI for the right femur.

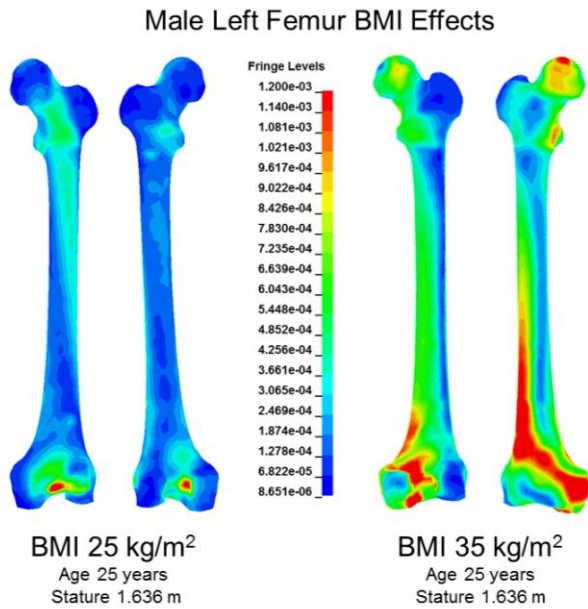


Figure 4-15b. Change in distributions of principal strain with BMI for the left femur.

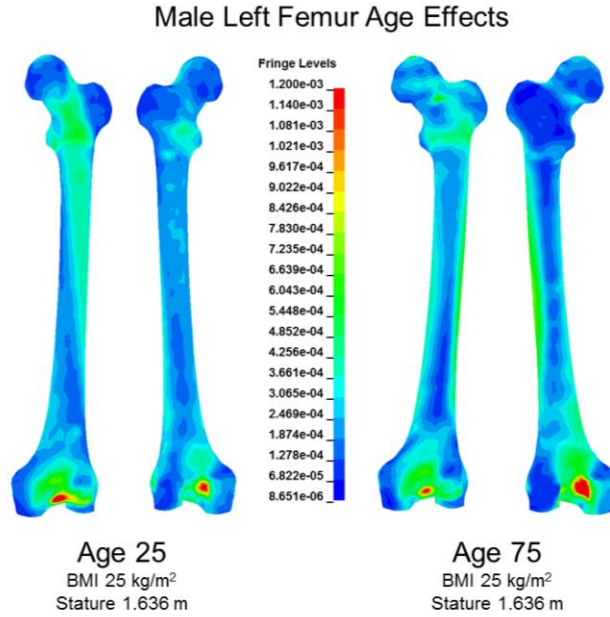


Figure 4-15c. Change in distributions of principal strain with age for the left femur.

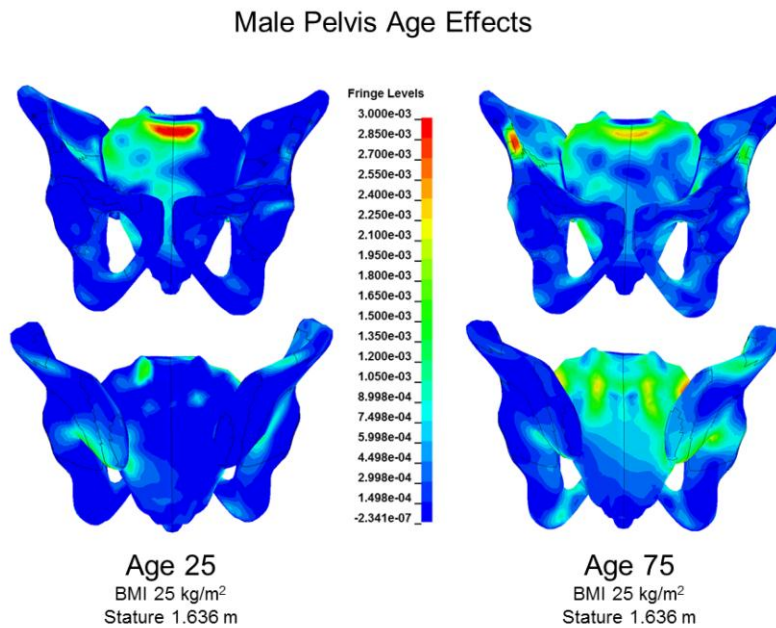


Figure 4-15d. Change in distributions of principal strain with age for the pelvis.

Male Force Results

The multivariate regression indicated that an increase in BMI from 25 to 35 kg/m² and stature from 1.636 to 1.887 m both caused a significant increase in force at both the right and left knee while holding other parameters constant. An increase in BMI from 25 to 35

kg/m² caused significant increases in the forces at the right and left hips. No significant effects were seen for the right distal tibia, while an increase in age and stature caused a significant decrease in force at the left distal tibia. One data point had a much higher left distal tibia force than the others, but without this data point in the analysis, the effects of age and stature were still significant. Table 4-6 gives the resulting contact forces at the knees, hips, and distal tibias for the male simulations. Figure 4-16 shows the distributions of forces in the right and left knee for BMI and stature, the right and left hips for BMI, and the left distal tibia for age and stature for the male models. Only the parameter indicated was allowed to vary in these plots since the other values were held constant at the middle value from the ranges.

Table 4-6. Male model force results

Male Test ID	Right Knee (kN)	Left Knee (kN)	Right Hip (kN)	Left Hip (kN)	Right Distal Tibia (kN)	Left Distal Tibia (kN)
M1	1.255	1.123	1.160	0.763	1.489	2.321
M4	1.145	1.313	0.908	1.236	2.330	2.924
M7	1.292	2.534	3.074	2.784	7.072	6.373
M9	2.231	3.530	2.617	2.274	3.508	2.480
M11	1.363	2.209	1.181	1.089	2.151	1.871
M15	1.564	4.025	2.204	2.328	4.722	1.734
M17	1.699	2.111	2.043	1.986	2.504	2.414
M18	2.250	4.031	1.942	2.568	3.464	2.285
M19	1.136	1.627	0.956	0.877	1.719	2.096
M20	1.348	2.622	1.085	1.122	2.127	1.290
M23	1.186	2.540	1.381	1.814	3.969	1.555
M24	1.608	4.118	1.885	2.398	4.201	1.715

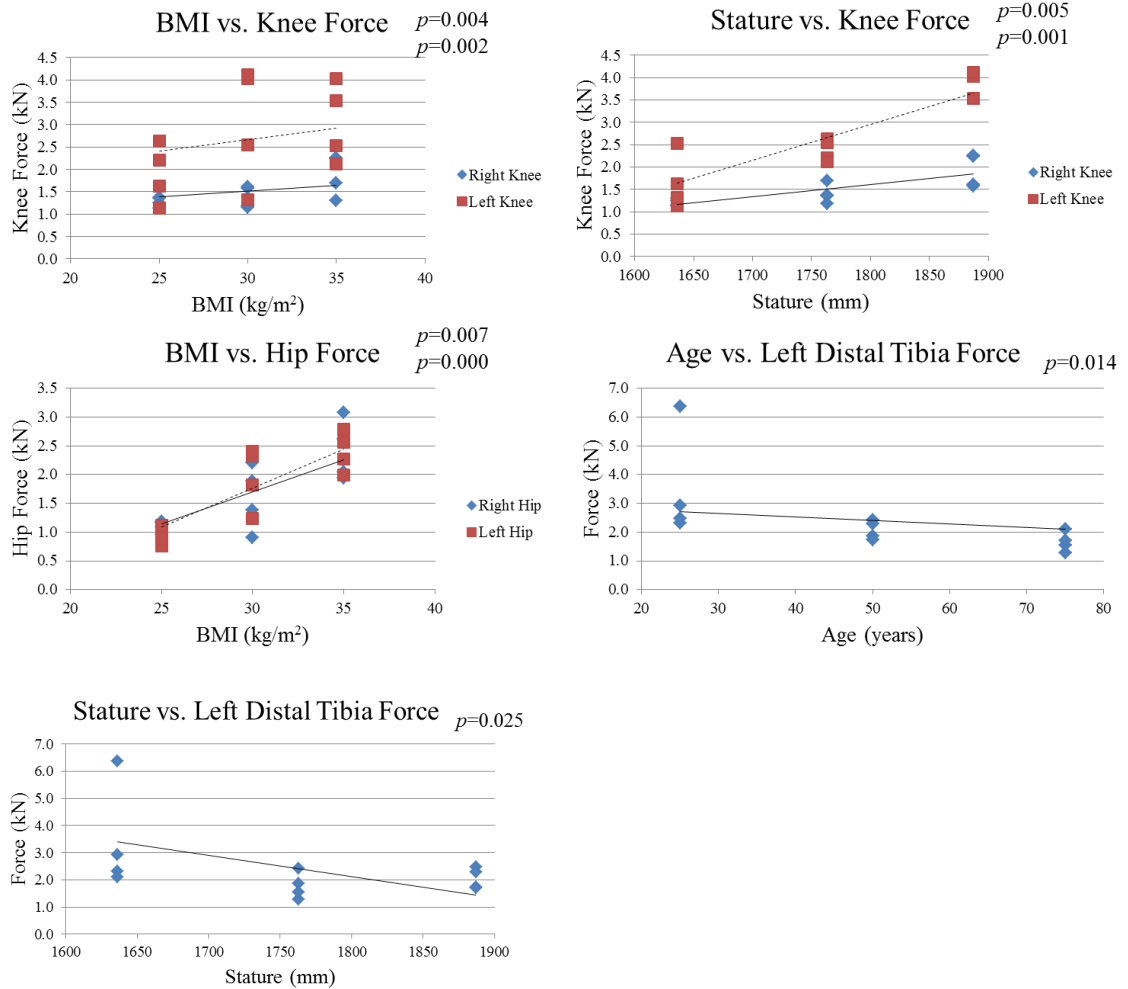


Figure 4-16. Distributions of forces for the male simulations.

Female Strain Results

Table 4-7 gives the resulting normalized strains for each model for the femurs, tibias, and pelvis from the female simulations. For the female simulations, BMI was significant for the right tibia, stature was significant for the left tibia, and age was significant for the left femur. For the right tibia, an increase in BMI from 25 to 35 kg/m² caused an increase in the normalized strain while holding other parameters constant, indicating that higher BMI occupants will have larger strain values in the right tibia. For the left tibia, an increase in stature from 1.507 m to 1.731 m caused a decrease in the normalized strain, indicating that taller occupants will have smaller strain values in the left tibia. For the left femur, an increase in age from 25 to 75 years caused an increase in the normalized strain,

indicating that older occupants will have larger strain values in the left femur. The coefficient values for each parameter for the linear multivariate regression equations determined for the right tibia, left tibia, and left femur are given in Table 4-8.

Table 4-7. Female model normalized strain results

Female Test ID	Right Tibia	Left Tibia	Right Femur	Left Femur	Upper Pelvis Surface	Lower Pelvis Surface
F1	0.393	0.734	0.167	0.192	0.527	0.589
F4	0.375	0.571	0.202	0.209	0.613	0.694
F7	0.481	0.755	0.229	0.238	0.528	0.570
F9	0.741	0.357	0.270	0.256	0.649	0.861
F11	0.262	0.488	0.238	0.198	0.455	0.461
F15	0.437	0.559	0.839	0.418	0.734	0.824
F17	0.543	0.597	0.288	0.360	0.566	0.445
F18	0.691	0.337	0.329	0.285	0.400	0.388
F19	0.618	0.872	0.233	0.296	1.343	1.406
F20	0.278	0.537	0.334	0.290	0.400	0.403
F23	0.851	0.907	0.337	0.376	0.389	0.419
F24	0.594	0.466	0.319	0.477	1.513	1.120

Table 4-8. Coefficient values for each parameter for the female linear multivariate regression equations determined for the right tibia, left tibia, and left femur

	Intercept	Age Coefficient	BMI Coefficient	Stature Coefficient
Right Tibia	-0.466	0.004	0.031	-0.0001
Left Tibia	2.947	0.004	0.008	-0.001
Left Femur	-0.503	0.003	0.007	0.0003

Figure 4-17 shows the distributions of normalized strains in the right tibia for BMI, the left tibia for stature, and the left femur for age for the female models. Only the parameter indicated was allowed to vary in these plots since the other values were held constant at the middle value from the ranges. Figures 4-18a, 4-18b, and 4-18c show the changes in the distributions for principal strain for the right tibia for BMI, the left tibia for stature, and the left femur for age for the female models. The female subjects with age 75 years, BMI 30 kg/m², and stature 1.731 m and age 75 years, BMI 25 kg/m², and stature 1.507 m had normalized strain values that exceeded the ultimate strain value in the pelvis, indicating a fracture prediction. The location predicted for fracture was along the edge of top part of the first sacral segment for both subjects.

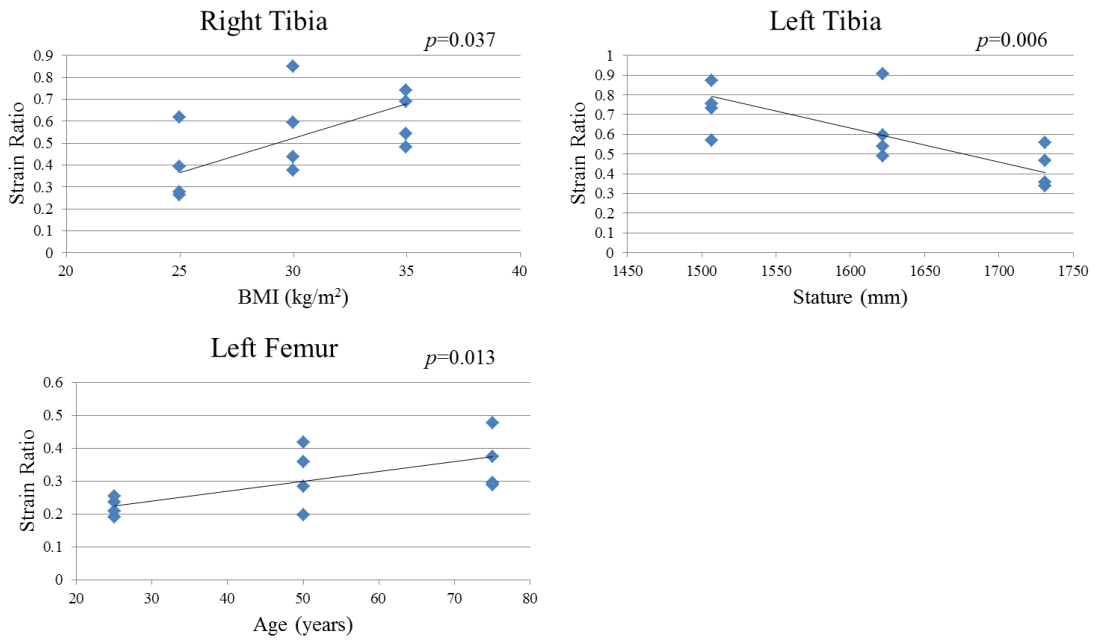


Figure 4-17. Distributions of normalized strains for the right tibia with BMI (top left), the left tibia with stature (top right), and the left femur with age (bottom left).

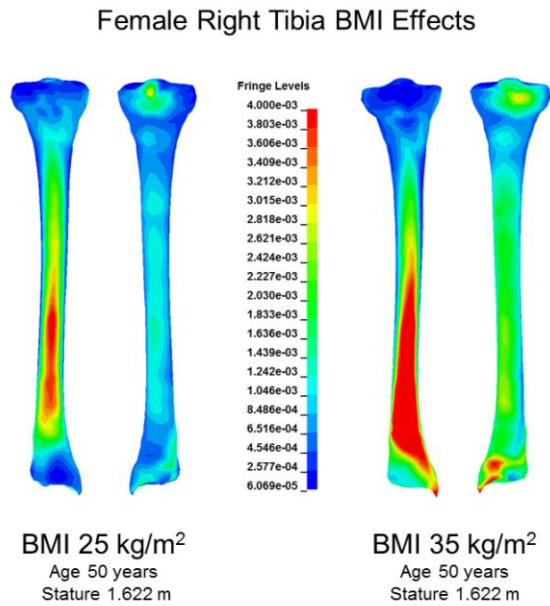


Figure 4-18a. Change in distributions of principal strain with BMI for the right tibia.

Female Left Tibia Stature Effects

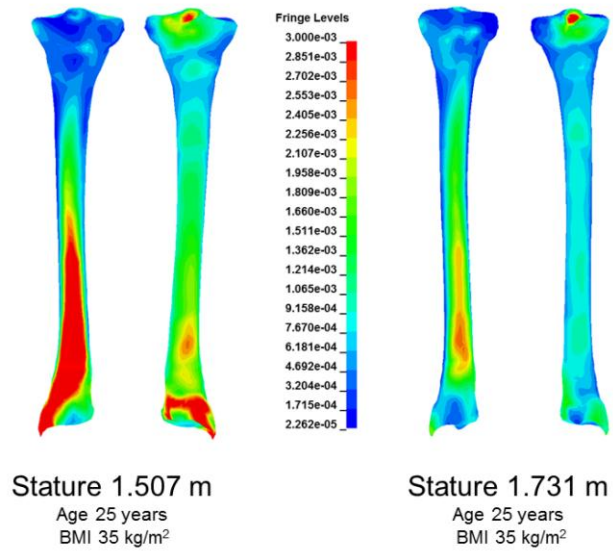


Figure 4-18b. Change in distributions of principal strain with stature for the left tibia.

Female Left Femur Age Effects

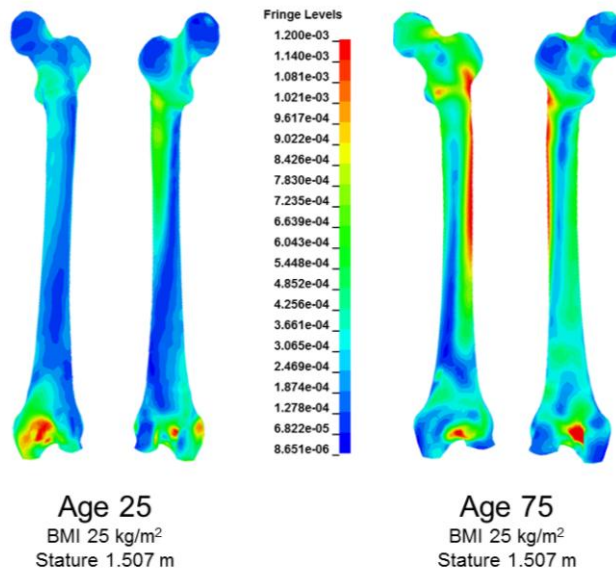


Figure 4-18c. Change in distributions of principal strain with age for the left femur.

Female Force Results

The multivariate regression indicated that an increase in BMI from 25 to 35 kg/m² and stature from 1.507 m to 1.731 m both caused a significant increase in force at the right and left knee. In addition, an increase in age from 25 years to 75 years caused an increase of force at the left knee. An increase in BMI from 25 to 35 kg/m² and stature from 1.507 to 1.731 m caused significant increases in the forces at the right hip, and an increase in BMI from 25 to 35 kg/m² caused an increase in force at the left hip. An increase in BMI from 25 to 35 kg/m² caused an increase in force at the right distal tibia, while an increase in age from 25 to 75 years and stature from 1.507 to 1.731 m caused a significant decrease in force at the left distal tibia. Table 4-9 gives the resulting contact forces at the knees, hips, and distal tibias for the female simulations. Figure 4-19 shows the distributions of forces in the right and left knee for BMI and stature, the left knee for age, the right hip for BMI and stature, the left hip for BMI, the right distal tibia for age, and the left distal tibia for age and stature for the female models. Only the parameter indicated was allowed to vary in these plots since the other values were held constant at the middle value from the ranges.

Table 4-9. Female model force results

Female Test ID	Right Knee (kN)	Left Knee (kN)	Right Hip (kN)	Left Hip (kN)	Right Distal Tibia (kN)	Left Distal Tibia (kN)
F1	0.740	1.045	0.991	1.003	2.117	3.039
F4	1.304	0.890	1.376	1.673	2.396	3.059
F7	1.143	0.911	1.158	1.756	3.004	3.460
F9	1.725	2.230	2.332	1.934	4.327	2.333
F11	0.826	1.500	0.778	0.703	1.576	1.973
F15	1.352	2.025	1.745	1.525	2.531	1.610
F17	1.386	1.851	1.700	2.036	4.468	2.474
F18	1.612	2.047	2.225	1.958	5.160	2.487
F19	0.682	0.908	1.005	1.438	2.467	2.721
F20	0.960	1.927	0.983	0.934	1.665	1.795
F23	1.335	1.867	1.234	1.361	3.536	2.086
F24	1.397	2.123	1.474	1.542	3.689	1.356

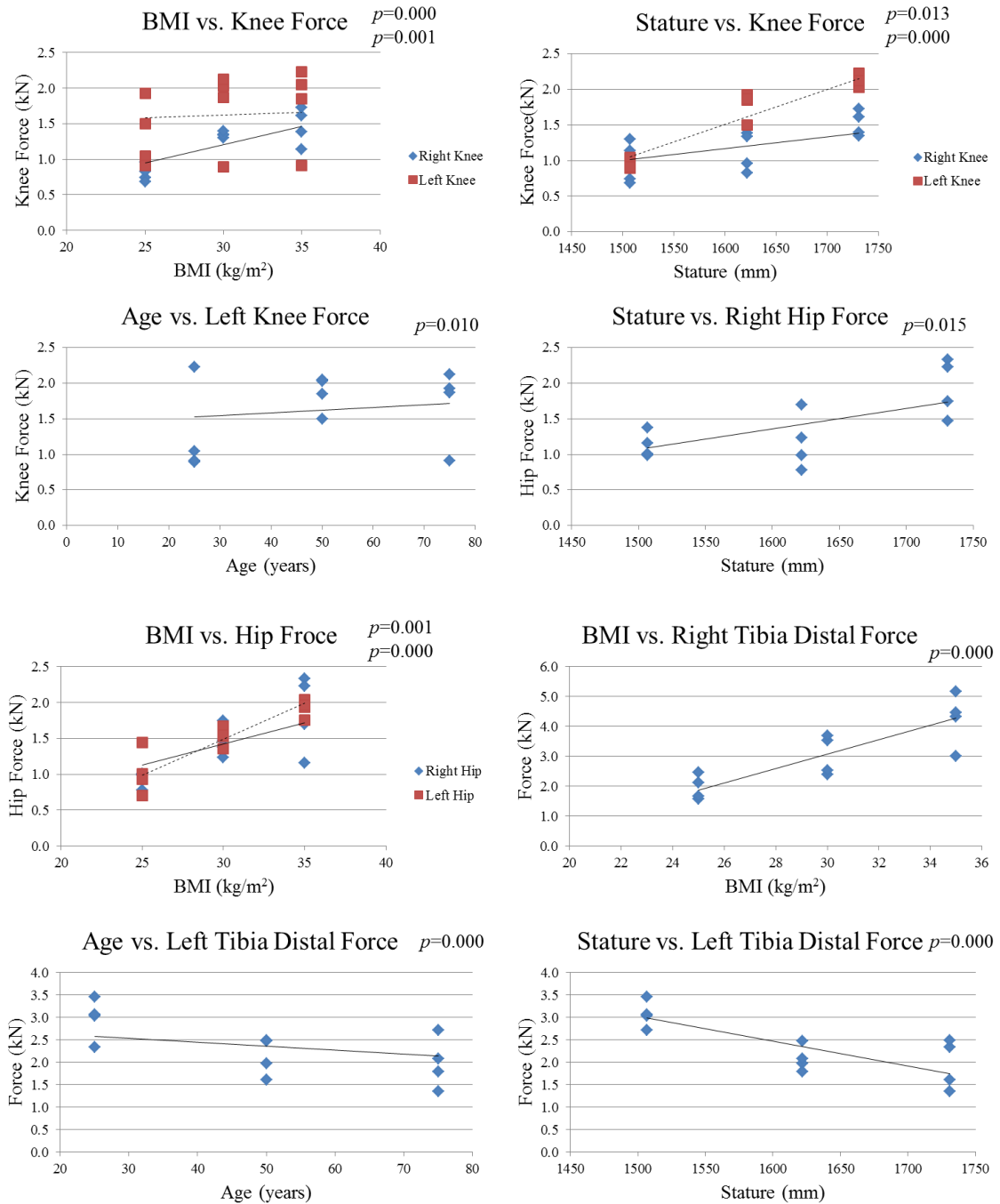


Figure 4-19. Distributions of forces for the female simulations.

Male and Female Kinematics Results

The kinematics of the spine relative to the lap belt (abdomen compression) was also investigated for the application simulations to further investigate the effects of age, BMI, and stature. For the male simulations, an increase in BMI, stature, and age caused an

increase in compression of the abdomen. For the female simulations, an increase in BMI and stature caused an increase in compression of the abdomen.

DISCUSSION

Summary

The development process for the whole-body parametric models with target skeletal geometry and material properties was described in this chapter. Twelve male and twelve female models were generated for use in simulations representing a single frontal crash to investigate the effects of age, BMI, and stature on lower-extremity injury. For the male simulations, an increase in age caused an increase in normalized strain values (peak strain normalized by age-adjusted ultimate strain) in the left femur and pelvis and an increase in BMI caused an increase in normalized strain values for the right and left femur. In addition, an increase in BMI and stature both caused a significant increase in force at the right and left knee. For the female simulations, an increase in BMI caused an increase in the normalized strains for the right tibia, and an increase in stature caused a decrease in the normalized strains for the left tibia. An increase in age caused an increase in the normalized strain for the left femur. In addition, an increase in BMI and stature both caused a significant increase in force at the right and left knee, and an increase in BMI caused significant increases in the forces at the right and left hips. These results indicate that, for similar crash conditions, increasing age and BMI cause increases in strain values and BMI causes increases in forces such that elderly and higher BMI occupants may be at increased risk for lower-extremity injuries, although the effects differ between left and right sides of the body. This is likely because of asymmetric lower-extremity posture and vehicle-specific factors like differences in left-to-right knee bolster geometry.

BMI Effects

The strain, force, and kinematic results of the whole-body simulations agree with hypotheses that the increase in LX injury risk with BMI is caused by increased amounts of adipose tissue over the ASIS with increasing BMI, which prepositions the belt farther

above the ASIS. As a result, the belt has to compress more flesh before it engages skeletal structures that can resist belt load. In addition, the severity of the knee bolster interaction increases (higher forces are seen at the knees).

Age Effects

Substantive differences did not exist in kinematics with age. The effects of age on strain can be attributed to the differences in geometry seen with age in the femur and pelvis predicted by the models as well as the use of age-dependent material properties in simulations. Figure 4-20 is taken from Figure 2-8 in Chapter II and shows the increase in overall cross-section geometry (total area of cross-sections of bone) and the decrease in cortical thickness in the femur with age. It is important to note that these geometric changes are not sufficient to produce an increase in strain with age. In fact, a series of simulations of femur response in which material properties were not changed with age produce an opposite effect, where strain decreased with increasing age. This finding indicates that it is critical to consider age-related changes in material properties when performing simulations with parametric FE models.

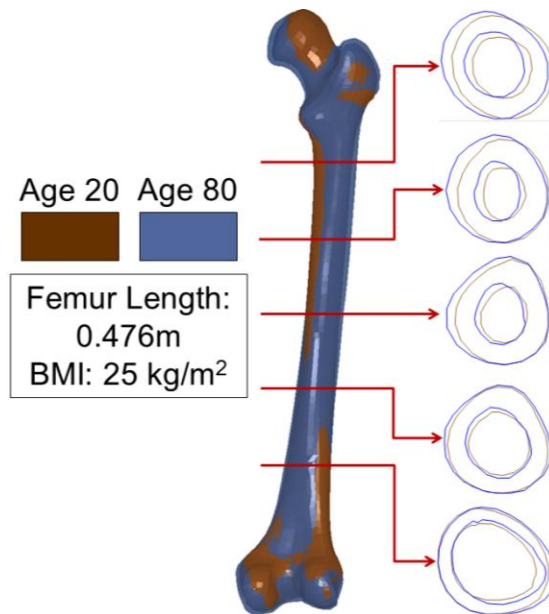


Figure 4-20. The effects of age on femur geometry predicted by the male femur models.

Sex and Stature Effects

Differences exist between men and women in the strains and forces predicted from the whole-body model simulations. Larger strains were predicted for women than for men in the right femur, right tibia, and pelvis. This result agrees with the finding that women are at increased risk for injury. However, it is difficult to determine the reasons for this difference due to the separate male and female models used. The effects of occupant characteristics on strains were different for different bones for men and women (femur versus tibia and right side versus left side). Again, the reasons for these differences are difficult to determine using the separate models because sex is not a parameter in the separate models. The results of the male versus female simulations can be compared for stature effects, but the same statures were not used in the models. Future work could develop a model with gender as a parameter, but then the stature effects would be difficult to investigate due to these interactions.

Other Effects

The left versus right sided differences in the effects of age, BMI, and stature on normalized strain results were likely due to differences in pre-crash posture. The right foot was positioned on the pedal for each simulation, which caused differences in the position of the right foot versus the left foot. These pre-crash postures were also different for varying statures due to the predicted location of the foot relative to the pedal. These differences suggest that posture (and likely vehicle interior geometry) has an effect on injury risk. In addition, the effects of occupant characteristics were not seen for all bones. These findings suggest that existing crash test dummies, such as the Hybrid III midsize male, which represent a fit young male (normal BMI), may not be useful for studying the effects of occupant characteristics on injury.

The hypotheses that women are at increased risk for foot-ankle injuries, while men are at increased risk for KTH injuries, and that men will have more hip injuries compared to women and women will have more knee and thigh injuries compared to men were neither proved nor disproved by the application simulations. Meaningful differences were not found between knee, thigh, hip, and foot-ankle strain responses for men and women, but

further work could determine the differences between men and women and these injuries by performing more simulations with similar sizes of men and women to compare predicted injury locations. In addition, the hypothesis that the effects of BMI are greater for men could not be tested. Also, the effect of age causing more KTH injuries was not found due to the limited number of simulations.

Knee Bolster Contact

Every simulation performed in this work resulted in knee-to-knee bolster contact. In most crash test simulations with Hybrid III dummy models and in physical testing with these same dummies, the knees of the dummy rarely contact the knee bolster. This is because the dummy has an unrealistic anterior pelvis geometry that results in the ASIS always capturing the lap belt. Assessing lower extremity injury risk could be better performed with a dummy with more realistic pelvis geometry, like the THOR midsize male, and perhaps with more flesh over the ASIS.

Fore-aft Seat Position

The fore-aft seat position of the vehicle seat was kept the same in the simulations performed in this work, although the location of the hips of the FE model relative to the knee bolster was set to size appropriate locations. As described in the methods, this was done for simplicity and because the position was unlikely to meaningfully affect the results in the lower extremities. However, the posture model used can also predict seat fore-aft position, and this position is affected by subject characteristics. Therefore, future work should include the varying seat fore-aft positions predicted by the posture model.

Poor Quality Elements

Some of the whole-body models listed in Tables 4-2 and 4-3 had elements with negative Jacobian values, as described in the results above. The areas where most of the bad elements occurred were in the soft tissue between the ribcage and pelvis because the baseline THUMS model had a smaller area in this region than a human. The THUMS model could be improved before using it for morphing, or a different baseline model

could be used. While it was straightforward to determine where elements with negative Jacobian values occurred in the models so that they could be fixed before simulations, a few other female models had elements that only caused an issue during simulations. These models were the highest BMI models in which the external body surface shape was affected by seatbelt locations. The skin folds predicted by the surface model would produce elements that would turn into bad elements during simulations due to interactions with the seatbelt. In these few instances, the location of the shoulder belt was changed slightly to allow the simulations to run to completion.

Foot Model

While the pelvis, femur, and tibia geometries were determined from the existing parametric models described in Chapters II and III, the feet were morphed based on targets from the external body surface model. This approach ignores changes in skeletal geometry that are not related to changes in external body surface shape. Considering these changes would require a parametric foot model that considers foot skeletal geometry. Such a model should be developed in the future.

Chapter V

Summary and Discussion

SUMMARY

The lower extremities are the most frequently injured body region in frontal crashes, accounting for 36% of all AIS 2+ injuries sustained by front-seat occupants (Kuppa and Fessahaie 2003). The effects of age, sex, and BMI on lower-extremity (LX) injury in frontal crashes can best be assessed using a FE model with geometry that is parametric with these occupant characteristics. Therefore, the main goal of this research was to develop such a parametric FE whole-body model and use it to begin to explore the effects of age, sex, and BMI on variations in LX geometry, material properties, body size, and body shape on lower-extremity injury risk. Male and female finite element models that have geometry and material properties that are parametric with, age, BMI, and stature were developed and validated in this work. Simulations were performed with these models to investigate the effects of age, sex, and BMI on variations in LX geometry, material properties, body size, and body shape, and to begin understanding the effects of these variations on lower-extremity injury risk.

Statistical models of femur, tibia, and pelvis surface geometry and femur and tibia cross-sectional geometry were developed based on CT data and using PCAR methods to predict nodal coordinates for the associated predicted geometries. These models were used to investigate the variations in femur, tibia, and pelvis geometry with subject parameters. This work generated parametric models that predict femur, tibia, and pelvis geometry based on age, BMI, and stature for men and women. In addition, age, BMI, and stature were found to significantly affect bone geometry.

Parametric FE models of the femur, tibia, and pelvis were developed in this work by linking the statistical models to meshes of similar bones from a baseline FE model of the human occupant from Toyota's THUMS 4 model, thus allowing the mesh geometries of these bones to be predicted based on occupant characteristics. The ability of the femur model (as an example of methods for all lower-extremity bones) to reproduce the responses of occupants with different geometry was validated by morphing the model to simulate responses of cadaver femurs used in studies of LX injury tolerance reported in the literature. The loading conditions applied to each femur were simulated and compared to the predicted and measured responses within and across test series. The validation simulations performed suggest that these types of models produce reasonable results compared to previous models and experimental studies.

Parametric FE whole-body models were developed by combining the parametric FE pelvis, femur, and tibia models with an external body surface shape model previously developed at UMTRI that predicts shape using age, sex, BMI, and stature. The pelvis, femur, and tibia models were fit inside the surface model, and the bone models and the external surface model were used to morph the template mesh to develop the whole-body models. Frontal-crash simulations of drivers of different sexes, ages, statures, and BMIs were performed with the whole-body models to begin assessing the relative contributions of age, sex, and BMI on the risk of LX injury. Results of these simulations are generally consistent with field data and indicate that increases in age and BMI cause increases in strains and forces in the lower extremities such that elderly and higher BMI occupants are at increased risk for particular types of lower-extremity injuries. However, the effects appear to differ between left and right sides of the body, likely because of asymmetric lower-extremity posture and vehicle-specific factors like differences in left-to-right knee bolster geometry. The results of the kinematics analysis of the lap belt also agree with hypotheses about the increase in compression of the abdomen with BMI. These hypotheses include that the increase in LX injury risk with BMI is caused by increased amounts of adipose tissue over the ASIS, which is thought to be because the belt sits farther above the ASIS as BMI increases and because the belt has to compress more flesh

before it engages skeletal structures that can resist belt load (Turkovich 2010). In addition, the results from the simulations neither support nor refute the hypotheses about sex effects. These hypotheses include that differences in LX injury risk and injury patterns with occupant sex may also be caused by differences in the size and shape of LX bones between men and women. Men have a larger bone size, on average, than women, consistent with their larger body size (Riggs et al. 2004). In addition, the differences in pelvic-bone anatomy and shape between men and women could explain differences in the risk of some LX injuries, i.e., the female acetabulum of the pelvis faces more forward than the male acetabulum (Wang et al. 2004).

LIMITATIONS

Development and Validation of the Statistical Models

Sample Size

The size of the samples used in development of the female femur and tibia statistical models could be considered low with 36 female subjects for the femur model and 28 female subjects for the tibia model (compared to 62 male subjects for the femur and 48 male subjects for the tibia). This is especially true in the young end of the distribution where a very few number of young female subjects were used. However, the addition of more data is likely not a good use of resources other than to improve the fit of the model for younger subjects. For example, fifteen additional female femurs were added to the female femur statistical model, and the new R^2 value for the external surface geometry was 0.75. Since this value is only slightly higher than the original value (0.74), more data is not necessarily useful for the female femur statistical model. This result would be similar for the female tibia statistical model. Therefore, no additional subjects were included in the development of the statistical models since the female subjects cover similar ranges in ages and BMIs as the male subjects.

Residual Variance

Residual variance exists in the PCAR models, and this residual variance could be considered when generating models of the population. However, residual variance was not considered in the statistical models in this work. If it was considered, occupants with anatomic variants that might affect injury response might be better represented. No methods were developed to consider the residual variance, but PCAR can be used to develop such methods. For example, a term that takes into account the residuals would need to be calculated and added to the regression equations along with the terms for the parameters. Future work could consider ways to include more of the residual variance to even better fit the subjects the models are trying to represent. Methods that consider more of the residual variance may be able to account for more anatomical variations that affect impact response.

Linearity Assumption

The PCAR methods assume that subject characteristics have a linear effect on PC scores. While this assumption is valid and produces reasonable statistical models, a nonlinear model may be able to fit the underlying data even better. For example, the effects of age may increase nonlinearly in the older age ranges. Future work should consider nonlinear effects of subject characteristics on PC scores in the regression analysis or nonlinear PCA to determine if the linear assumption holds true.

Foot Statistical Model

For this study, a simple scaled and morphed foot model based on the external body surface shape was used in simulations with the FE models described in Chapter IV. The overall trend in foot size should be captured by this method, which should allow for reasonable predictions of foot-ankle injury risk. A statistical model of the foot was not included in this study that explicitly considers variations in individual foot bone geometry with occupant characteristics that are independent from external geometry. Eventually such a model will need to be developed so that it can be used in the entire lower-extremity parametric model.

Sex

Separate models were developed for men and women in this study so that the effects of age, BMI, and stature on lower extremity injury response in frontal crashes could be studied for both sexes. However, this approach prevents the characterization of sex effects on lower extremity injury response. Sex could have been used as a binary variable in one model, instead of two separate models, where male or female were the two options. This type of model would have allowed the effects of sex on injury response to be estimated, but such estimates would likely have been confounded with the effects of stature, which covaries with sex.

Development and Validation of the Parametric Finite Element Models

Validation Simulations

The validation simulations performed with the femur served as an example of the methods used for validation of parametric models in this work because there were not sufficient data in the literature to validate the responses of other body regions of the parametric model in a similar manner. The existing data do not include the necessary cross-sectional geometry, material properties, and response data for complete validation. Further validation of the femur and other skeletal components as well as the whole lower extremity response is needed. However, the results of the femur validation simulations suggest that the process for varying model geometry does not affect model validity, and by extension, that the morphed tibia and pelvis models, as well as the entire morphed lower extremities, are likely valid.

Material Properties

Material properties determined from CT were not considered in this work, despite previous research that has done exactly this. Bone density values derived from calibrated CT can be used to determine material properties, and CT data, along with relationships

between density and material properties, have been used to develop subject-specific FE models (e.g., Keaveny et al. 2008 and Keyak and Kalkinstein 2003). However, other studies indicate that the relationship between bone density and material properties may vary with predictors of bone geometry, such as age. For example, Heaney (2003), Nalla et al. (2004), and a series of related papers suggest that age-related changes in fracture toughness on a material level contribute to increased fracture risk for older adults. This suggests that statistical models of material properties that are based on the spatial distribution of bone and bone density for a body region should be supplemented with data from physical testing of bone material from that body region. Parametric material models could be generated using methods similar to those described by Bredbenner et al. (2014), where CT scan data can be used to determine relationships between density and material properties at all locations on the bone. These density-based models will, at best, apply regionally and not at the single element level. Reasons for this are that such material models are not available for a wide range of anatomic regions and that implementing these models would fundamentally change the baseline FE model and thus require extensive revalidation.

Application of the Parametric Whole-Body Models

Parameters Used in Simulations

Age, BMI, and stature were varied for the male and female models used in the simulations described in Chapter IV. In addition, pelvis, femur, and tibia material properties were varied with age for these models. However, the location of model hips relative to the seat H-point was used, and the posture of the models was determined by the external surface model which is based on body shape in a single seat. Fore-aft seat position was not varied, and as a result, the pelvis interacted with different parts of the seat than it would in a real world situation where an occupant would adjust fore-aft position. In addition, the average predicted seatbelt fit was used for each set of characteristics by determining the position of the lap belt based on regression equations. Seatbelt fit and posture will need to be varied in the future as they are known to affect

lower-extremity injury risk. Eventually material models that consider the effects of bone disease will also need to be used in the parametric models.

Simulation Approach

A Uniform Latin Hypercube design of experiments approach was used in this work to determine a reduced set of simulations to begin to explore the effects of occupant characteristics on lower-extremity injury. A reduced set of simulations was needed because each simulation requires over 13 hours to run on 80 nodes on cluster space at the University of Michigan. The set of 24 simulations is small, and therefore, the results of the simulation study should be considered as an initial investigation into the effects on injury. Despite this small number of simulations, there were some significant trends in model predictions with occupant characteristics. This indicates that the approach used in this work represents a reasonable first step in using simulations with parametric FE models to explore the effects of occupant characteristics on lower-extremity injury.

Shoes

The whole body models developed in this work did not include shoes because the template THUMS model lacks shoes. Shoes can affect the response of the lower extremities in a crash. Variations in leg loads can exist and differences in ankle stability occur with different sizes of heels (Crandall et al. 1996). These variations can change how the lower leg and foot-ankle regions are loaded in a frontal crash, which can change the risk for injury. However, the large variation in style of shoe worn by drivers makes it difficult to determine effects of shoes on lower-extremity injury.

Fracture Prediction

Although fracture was not simulated in this work, it is possible to implement ultimate strain-based failure criteria and use element deletion methods to estimate the effects of bone fracture on subsequent injury. However, fracture prediction is difficult as it is affected by mesh quality, density, and element type, and post yield behavior varies with age and strain rate. Fortunately, simulating fracture prediction is not necessary for most

applications of parametric FE models as loading should be in the sub-fracture regime. Therefore, predicted strain normalized by ultimate strain can be considered in an objective function for optimization.

BENEFITS OF PARAMETRIC MODELS

To further investigate the parametric FE models, the benefits of using parametric models were quantified by comparing the results of simulations with the male and female parametric femur models to simulations with (1) femur models with geometry derived from length scaling, (2) the midsize male femur (which represents the scenario in which no attempt is made to account for the effects of occupant characteristics on injury), (3) femur models with specimen-specific geometry, and (4) femur models with specimen-specific geometry and yield stress fit to match individual specimen responses.

Comparison between Parametric Models and Scaled/Midsized Models

The benefits of the parametric FE modeling approach for generating different model geometries over traditional geometric scaling methods for the femur were assessed by (1) uniformly scaling the THUMS 4 FE femur models in all three axes to match the femurs from the Ivarsson study using a scaling ratio determined from femur length, (2) performing simulations of the test conditions applied to the femurs in the Ivarsson study, and (3) comparing the results of these simulations with similar simulations performed using the parametric femur models. In generating scaled femurs, left femurs were generated using a reflection about the long axis of the corresponding right scaled femurs.

In addition, simulations were performed with the unmodified right midsize male THUMS 4 femur in the 25 test setups for right and left femurs from the Ivarsson study to compare the parametric models to the midsize-male model. The right midsize femur was reflected about the long axis to compare simulations with the average left femur to the 12 left-side tests.

An average material property for the scaled femurs was calculated in the same way as for the parametric femurs, and this value (yield stress=160 MPa) was used in the scaled femur and midsize-male femur simulations. Similar to the validation simulations described in Chapter III, the errors of the impactor forces at the time of experimental failure between the tests and the midsize and scaled simulations were calculated using Equation 1, and the differences in the slope values of the force histories between the tests and simulations were also determined using the same method as for the parametric models.

$$\text{Percent error} = (\text{Simulation} - \text{Test}) / \text{Test} * 100\% \quad (1)$$

Comparison between Parametric Models and Specimen-specific Models with and without Specimen-specific Yield Stress

An estimate of the error in parametric model FE predictions that is associated with geometry was obtained by comparing the results of simulations of the Ivarsson tests using femurs with specimen-specific geometry to the results of corresponding simulations with the parametric FE models. Femur models with specimen-specific geometry were developed from CT scans of the PMHS femoral shaft by morphing and fitting the shaft of the THUMS 4 femur template mesh onto bone surfaces from the 25 PMHS femurs from the Ivarsson study and calculating cortical thickness values along the shafts. The same yield stress value that was used in the validation simulations (140 MPa) was used for all simulations to isolate the effects of errors in geometry from those of material properties.

In addition, a specimen-specific yield stress was obtained by optimizing the fit to the loading curves for each of the models of the Ivarsson femurs. The baseline THUMS material values were used for all material properties except yield stress. Impactor force errors at the time of experimental failure between the tests and the specimen-specific simulations, with and without specimen-specific yield stress, were calculated using Equation 1, and the differences in the slope values of the force histories between the tests and simulations were also determined. The results from these comparisons were used to assess the relative performance of specimen-specific and parametric models. The

comparisons between the parametric, specimen-specific, and specimen-specific yield stress models provided an estimate of the contributions of geometry and material properties to model errors.

Benefits of Parametric Models Results

The average error in peak force (5%) and the average slope (-1%) predicted by the parametric models were provided in Chapter III. Figure 5-1 shows boxplots of the distributions of differences between impactor forces at the time of experimental failure for the tests and parametric simulations and distributions of differences between the slope of the force histories from the time of impactor contact until the time of fracture between the experimentally measured results and the simulation results. The first box plot on the left gives the percent error for the force, and the first box plot on the right gives percent error for slope.

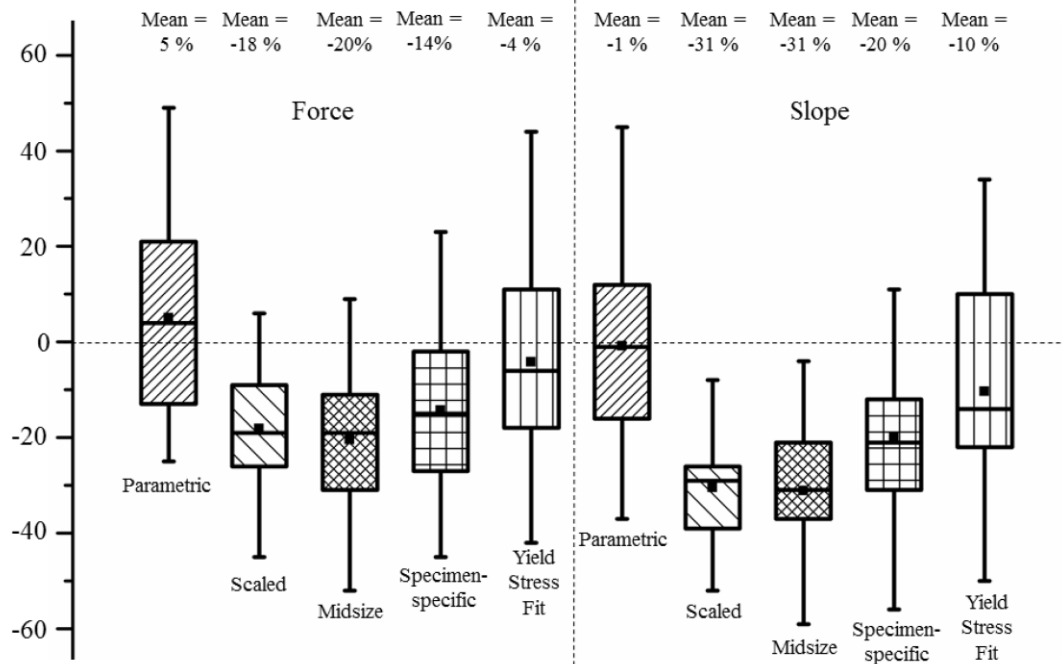


Figure 5-1. Distributions of percent differences between peak impactor forces (left) and slopes (right) for the experimentally measured test results and the values for parametric, scaled, midsize, specimen-specific, and yield stress fit results.

The next two box plots on the left side of Figure 5-1 show the distributions of differences between peak impactor forces for the experimentally measured results and the results of the scaled and midsize femur simulations. The average error for the scaled femurs was -18% and the average error for the midsize femurs was -20%. Therefore, the parametric femurs had the lowest average error of the 3 sets of simulations (parametric, scaled, and midsize femur simulations) at 5%. The parametric femurs also had the lowest absolute average error at 18% compared to scaled at 19% and midsize at 21%. The results for the slope values follow similar trends, as can be seen on the right side of Figure 5-1. The values for and the average and absolute errors in peak forces and slopes for each of the midsize and scaled tests are provided in Appendix G.

The last two box plots on the left side of Figure 5-1 show the distributions of differences between the experimentally measured results and the results of the specimen-specific with and without specimen-specific yield stress femur simulations. The average error for the specimen-specific femurs was -14% and the average error for the yield stress fit femurs was -4%. Therefore, the parametric femur models had similar error to the yield stress fit specimen-specific models. The parametric femurs also had similar absolute error to the specimen-specific with and without specimen-specific yield stress femurs. The results for the slope values follow similar trends, as can be seen on the right side of Figure 5-1. The values for and the average and absolute errors in peak forces at the time of fracture in the tests and slopes for each of the specimen-specific with and without specimen-specific yield stress tests are provided in Appendix G. The response curves for all parametric, scaled, midsize, specimen-specific, and yield stress fit specimen-specific simulations are provided in Appendix H.

Similar to the results of previous parametric model studies (Gayzik et al. 2008; Li et al. 2011; Shi et al. 2015), the results of this study indicate that parametric models can, on average, more accurately predict human responses than models of different sizes developed using simple scaling methods. Comparisons of parametric model predictions to the predictions of FE models generated using the different approaches to simulating population variability in geometry indicated that the average error in the peak force was

much smaller for the parametric models (5%) than for either the midsize-male femur model (-18%) or the uniformly scaled femur models (-20%). In addition, the error in peak force for the parametric models (5%) was similar to the error in peak force for the specimen-specific models with an individually fit yield stress (-4%). The error in peak force for the specimen-specific geometry only models was larger than the parametric models due to the average material property better fitting the parametric model results. While these results only apply to the femur, they are likely generalizable to long bones, such as the tibia, where similar errors in geometry and similar material properties are expected.

FUTURE WORK

Population-Based Simulations

The parametric modeling approach proposed in this work enables the use of whole-body FE models for population-based simulations. Such population-based simulations are performed by using the parametric model to generate FE models with geometries that span the ranges of distributions of occupant characteristics and using these models in simulations of crashes. Given that the relative exposure of occupants with different characteristics involved in crashes is known from real world crash injury data, simulation results can be weighted to estimate population response and injury risk. For example, if more elderly occupants experience a certain type of injury in a certain type of crash, then this can be taken into account when running that type of crash simulation.

Effects of Muscle Forces on Lower-extremity Injury Risk

While no muscle models were included in this work, the effects of muscle forces on lower-extremity injury risk cannot be ignored. For example, Chang (2009) proved that muscle tension increases knee impact forces by increasing the effective mass of the KTH complex due to tighter coupling of muscle mass to bone. Age, BMI, and stature will have an effect on muscle tension in both men and women in crashes, and eventually muscle models should eventually be included in parametric models.

Residual Variance

As described above, the statistical models do not incorporate residual variance into their predictions, which means the parametric FE models do not consider residual variance as well. To include residual variance in the simulations with FE models, a term that takes into account the residuals in the statistical models would need to be added to the regression equations. Then the parametric models would account for the residuals since the statistical models predict the locations of nodal coordinates for the parametric FE models, and simulations with the FE models would consider residuals, as well.

Validation Simulations

The shafts of the femur models were the only component of the lower-extremity FE models that were validated using PMHS data due to the lack of necessary information in most other PMHS studies. Validation simulations need to be performed with the whole femur, tibia, and pelvis, as well as all lower-extremity components combined, and then with the whole-body model. However, very few studies exist with the necessary information on cross-sectional geometry, external geometry, response data, and posture that are needed to completely validate the lower-extremity or whole-body models. Once sufficient data is found or becomes available, the validation simulations can be performed using similar methods to the FE femur model validation described in Chapter III in which the ability of the femur model to reproduce the responses of subjects with different geometry was validated. Further validation of the femur and validation of the tibia and pelvis should be one of the main focuses of future work, as well as validation of the lower extremities combined. However, future work should also focus on performing PMHS tests with the necessary detail for complete validation so that the validations can be done.

Effects of Occupant Characteristics on Lower-extremity Injury Risk

Only one series of application simulations in a frontal crash scenario with the whole-body model was performed in this work because the lower extremities are the most frequently injured body region in frontal crashes sustained by front-seat occupants (Kuppa and

Fessahaie 2003). Eventually more simulations with an improved whole-body model will be necessary to further investigate the effects of subject characteristics on lower-extremity injuries and other body region injuries. For example, more simulations than the 24 performed in this work could be performed to cover more of the ranges of ages, statures, and BMIs for both sexes seen in the crash-involved population. In addition, different boundary conditions than the 56 kph frontal crash scenario could be used. Other parameters such as seatbelt fit and posture could be varied with occupant characteristics instead of choosing the average fit or posture. Finally, all other parameters mentioned in the discussion of Chapter IV above could also be included such as seat position and material properties. All of these future simulations can be used to design better occupant protection systems to protect the entire population (not only the vulnerable populations of female, elderly, and high BMI occupants). Parametric material models especially should be one of the main focuses of future work since material properties also vary significantly with occupant characteristics, as has been described previously. In addition, analyses of the future simulations should include nonlinear effects, particular those of age. Next steps for this work include using all 27 male and 27 female models generated as described in Chapter IV to run simulations in the frontal crash scenario, as well as generating models where one parameter is varied at a time while the other two parameters are held constant for the male and female models and performing frontal crash simulations with those models. This second set of simulations allow for independent estimates of the effects of occupant characteristics on injury at the expense of realistic simulations. In addition, more than 27 female and 27 male models will be developed to further investigate the effects of age seen at ages above 50 years.

Chapter VI

Conclusions

The effects of age, sex, and BMI on variations in LX geometry, material properties, body size, and body shape were investigated in this work to begin understanding the effects of these variations on lower-extremity injury risk. This was accomplished by developing, validating, and performing simulations with male and female human-body finite element models that have geometry and material properties that are parametric with, age, BMI, and stature. Major contributions of this work include:

- Using principal component analysis and regression analysis to develop statistical models that predict the external surface geometry of the pelvis, femur, and tibia as functions of age, BMI, and a size parameter reasonably well.
- Validating the parametric FE femur model successfully as an example of new validation methods by matching the mean overall in the experimental dataset and following the trends in the dataset.
- That this is one of the first applications of whole-body model development using morphing of body shape, posture, and skeletal geometry.
- Performing frontal-crash simulations of drivers of different ages, statures, and BMIs with 12 male and 12 female whole-body models to begin assessing the relative contributions of age, sex, and BMI on the risk of LX injury.
- That age and BMI significantly affect the response of the lower-extremities in frontal crash simulations such that an increase in age and BMI caused increases in predicted risk of injuries, agreeing with the hypotheses that elderly and high BMI occupants are at increased risk for lower-extremity injuries.
- Developing whole-body models that can eventually be used to design occupant protection systems to reduce the risk of lower extremity injuries for vulnerable populations, as well as the entire population.

Appendices

APPENDIX A

Mathematica code for radial basis function interpolation from Bennink et al. (2006):

```
Options[RadialBasisInterpolation] =
  {RadialBasisNorm → Automatic, Smoothness 0.};
ThinPlateSplineNorm[1] =
  Compile[{{#1, _Real, 1}},  $\sqrt{(\#1.\#1)}$ ];
ThinPlateSplineNorm[2] =
  Compile[{{#1, _Real, 1}},
    (If[#1>0., #1[Log[ $\sqrt{\#1}$ ], 0.] &] [#1.#1];
ThinPlateSplineNorm[p_?OddQ] =
  Compile[{{#1, _Real, 1}}, ( $\#1.\#1$ )p/2, {{p, _Integer}}];
ThinPlateSplineNorm[p_?EvenQ] =
  Compile[{{#1, _Real, 1}},
    (If[#1>0., #1p/2 Log[ $\sqrt{\#1}$ ], 0.] &] [#1.#1], {{p, _Integer}}];
GaussianNorm[σ_] = Compile[{{#1, _Real, 1}},
  (If[#1>0.,  $e^{-\frac{\#1}{2\sigma^2}}$ , 1.] &] [#1.#1], , {{σ_Real}}];
RadialBasisInterpolation[data_List, opts___?OptionQ] :=
  Module[{points, values, n, pointDim, valueDims,
    valueRank, ϕ, B, Q, O, A, λ, x, w, a, slots},
    {ϕ, λ} = (RadialBasisNorm, Smoothness) /. {opts} /.
      Options[RadialBasisInterpolation];
    {points, values} = N[Transpose[data]];
    If[Depth[points] == 2, points = List /@ points];
    {n, pointDim} = Dimensions[points];
    valueDims = Rest[Dimensions[values]];
    valueRank = Length[valueDims];
    If[ϕ == Automatic,
      ϕ = ThinPlateSplineNorm[Max[2, pointDim]];
    O = Table[0., {pointDim + 1}, {pointDim + 1}];
    B = Outer[ϕ[ #1 - #2] &, points, points, 1];
    Q = (Prepend[#1, 1] &) /@ points;
    A = MapThread[Join,
```

```

MapThread[Join,  $\left( \begin{array}{c} B - \lambda IdentityMatrix[n] \\ Q^T \end{array} \right) \begin{array}{c} Q \\ O \end{array} ]];
b = PadRight[Transpose[values,
  RotateRight[Range[valueRank + 1]]],
  Append[valueDims, n pointDim + 1], 0];
x = Map[LinearSolve[A, #1] &, b, {valueRank}];
w = Map[Take[#1, n] &, x, {valueRank}];
a = Map[Take[#1, -(pointDim + 1)] &, x, {valueRank}];
slots = Array[Slot, {pointDim}];
(Compile[#1, #3.#4 /@ Transpose [#5- #6] + #2,
  {{#4[_], _Real, 0}}] &)[{#1, _Real} &] /@ slots,
a.Prepended[slots, 1], w,  $\phi$ , slots, Transpose[points]]]$ 
```

Mathematica code for an example of radial basis function morphing from Bennink et al. (2006):

```

source = Table[Random[Real, {10, 90}], {7}, {2}];
target = source + Table[Random[Real, {-5, 5}], {7}, {2}];
grid = Table[{x, y}, {x, 1, 100, 2.5}, {y, 1, 100, 2.5}];
Show[Graphics[{Gray, Line/@ grid, Line/@ gridT, Blue,
  PointSize[0.02], Point/@ source, Red,
  Circle[#1, 2] & /@ target}], AspectRatio→1, Frame→True];
rbi := If[# == 0, 0.5,  $\frac{BesselJ[1, \frac{1}{5}\sqrt{\#}]}{\frac{1}{5}\sqrt{5}}$ ] & [v.v];
rbi = RadialBasisInterpolation[{source, target}T, RadialBasisNorm→rbi];
newgrid = Map[rbi @@ #1 &, grid, {2}];
Show[Graphics[{Gray, Line/@ newgrid, Lin/@ newgridT,
  PointSize[0.02], Blue, Point /@ (rbi @@ #1 &) /@ source,
  Red, (Circle[#1, 2] &) /@ target}], AspectRatio→1, Frame→True];

```

APPENDIX B

Table B-1. Subject characteristics from Ivarsson et al. (2009) data

Test ID	Subject ID	Femur Side	Age (years)	Femur Length (m)	BMI (kg/m ²)	Gender
1.01	373	Left	51	0.548	19.5	Male
1.02	373	Right	51	0.548	19.5	Male
1.03	374	Left	62	0.491	27.2	Male
1.04	374	Right	62	0.491	27.2	Male
1.05	375	Left	62	0.484	25.9	Male
1.06	375	Right	62	0.484	25.9	Male
1.07	376	Left	49	0.572	26.8	Male
1.08	376	Right	49	0.572	26.8	Male
1.09	377	Right	62	0.501	29.1	Male
1.10	378	Left	44	0.512	22.0	Male
1.11	378	Right	44	0.512	22.0	Male
1.12	379	Left	58	0.525	42.1	Male
1.13	379	Right	58	0.525	42.1	Male
1.14	380	Left	65	0.496	27.2	Male
1.15	380	Right	65	0.496	27.2	Male
1.16	381	Left	53	0.488	18.5	Male
1.17	381	Right	53	0.488	18.5	Male
1.18	382	Left	64	0.445	31.7	Female
1.19	382	Right	64	0.445	31.7	Female
1.20	383	Left	40	0.430	20.0	Female
1.21	383	Right	40	0.430	20.0	Female
1.22	387	Left	45	0.436	38.3	Female
1.23	387	Right	45	0.436	38.3	Female
1.26	389	Left	50	0.440	23.3	Female
1.27	389	Right	50	0.440	23.3	Female

APPENDIX C

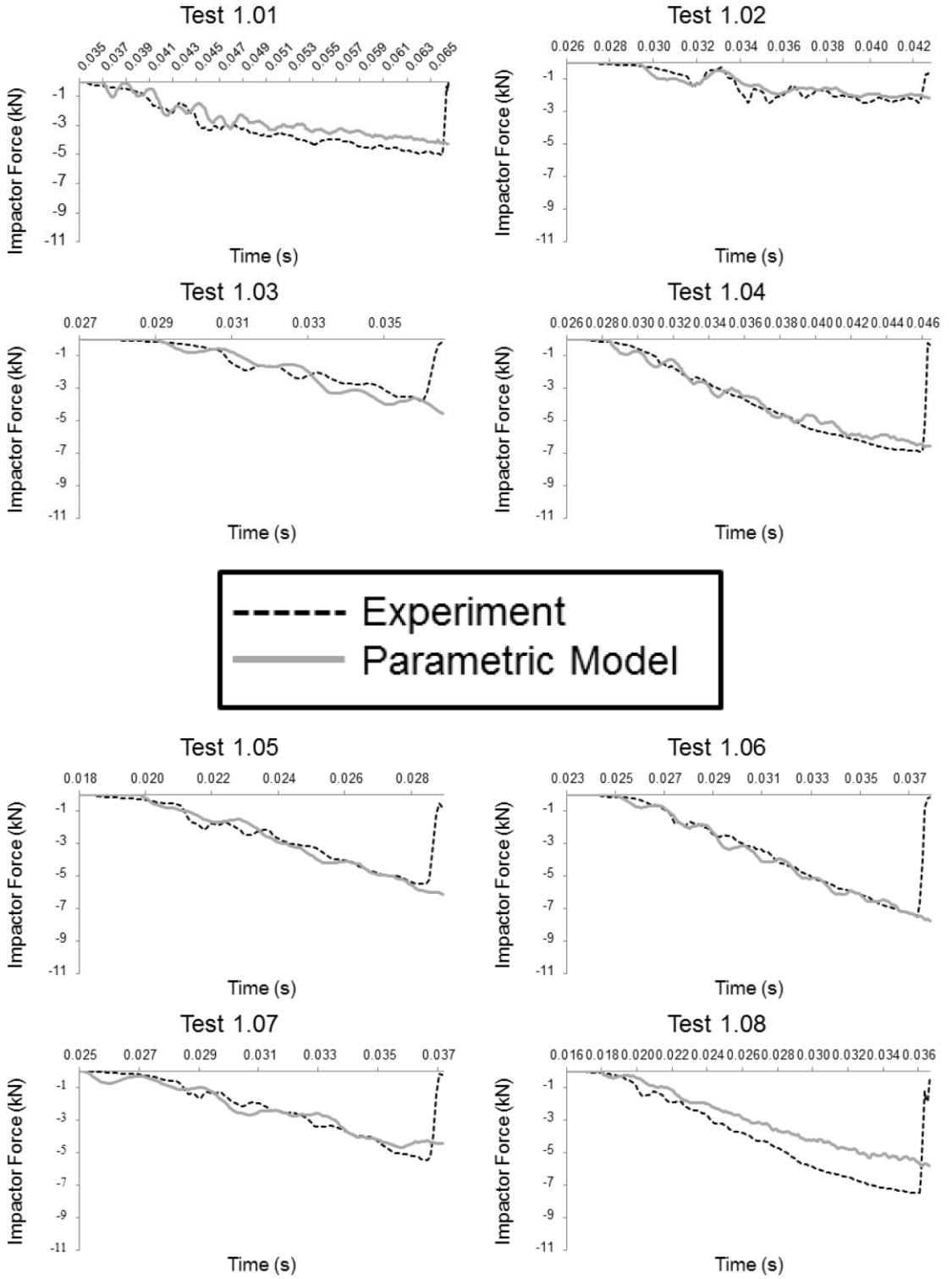
Table C-2. Percent differences between impactor forces for experimentally measured and parametric simulations at time of failure

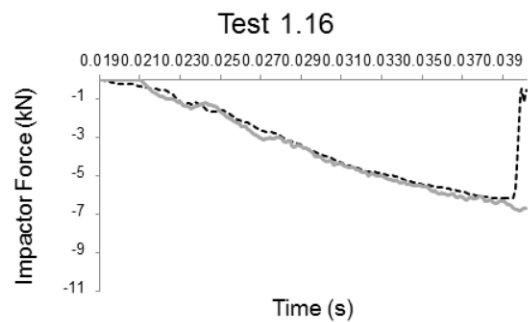
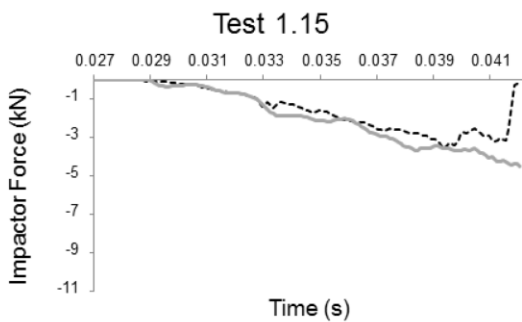
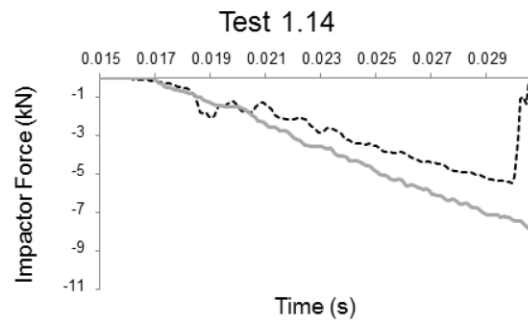
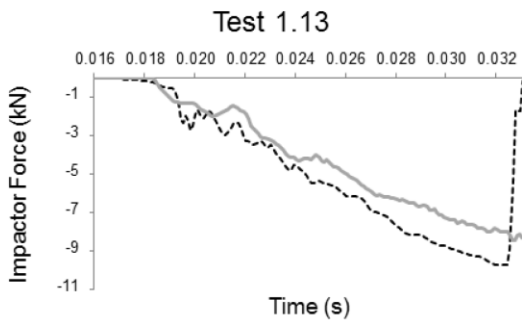
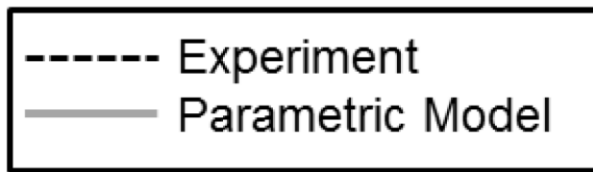
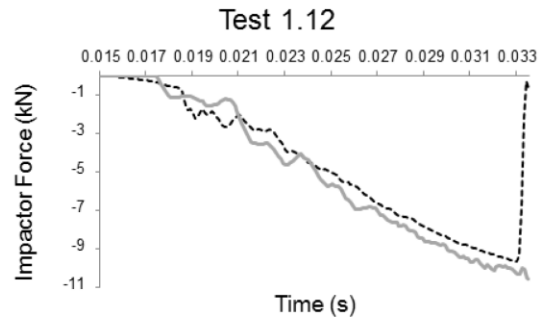
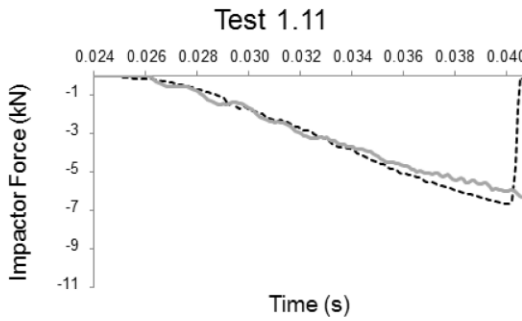
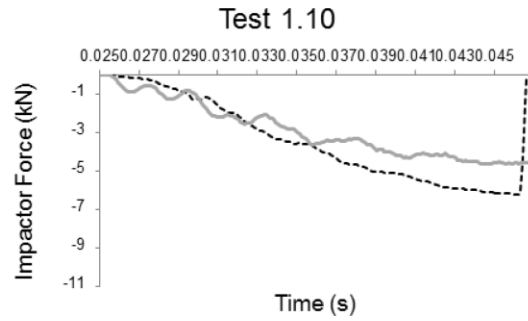
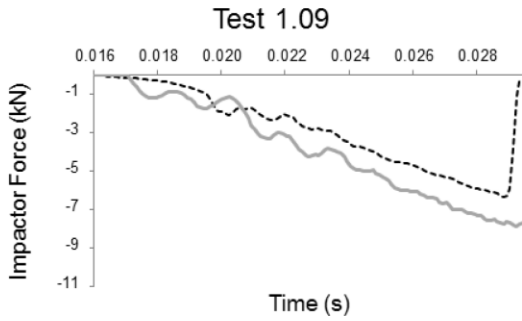
Test ID	Subject ID	Femur Side	Gender	Test Force (kN)	Parametric Force (kN)	Percent Difference	Absolute Percent Difference
1.01	373	L	M	-5.00	-4.26	-15	15
1.02	373	R	M	-2.48	-2.18	-12	12
1.03	374	L	M	-3.78	-4.58	21	21
1.04	374	R	M	-6.88	-6.59	-4	4
1.05	375	L	M	-5.48	-6.14	12	12
1.06	375	R	M	-7.40	-7.71	4	4
1.07	376	L	M	-5.44	-4.67	-14	14
1.08	376	R	M	-7.47	-5.80	-22	22
1.09	377	R	M	-6.31	-7.87	25	25
1.10	378	L	M	-6.23	-4.65	-25	25
1.11	378	R	M	-6.66	-6.30	-5	5
1.12	379	L	M	-9.66	-10.53	9	9
1.13	379	R	M	-9.70	-8.44	-13	13
1.14	380	L	M	-5.47	-7.81	43	43
1.15	380	R	M	-3.58	-4.48	25	25
1.16	381	L	M	-6.18	-6.79	10	10
1.17	381	R	M	-6.30	-7.64	21	21
1.18	382	L	F	-5.21	-6.71	29	29
1.19	382	R	F	-2.56	-2.78	8	8
1.20	383	L	F	-5.07	-4.54	-10	10
1.21	383	R	F	-6.48	-5.53	-15	15
1.22	387	L	F	-4.30	-5.77	34	34
1.23	387	R	F	-3.97	-5.91	49	49
1.26	389	L	F	-7.09	-5.67	-20	20
1.27	389	R	F	-6.69	-5.99	-10	10
Mean				-5.8	-6.0	5	18
SD				1.8	1.8	21	12

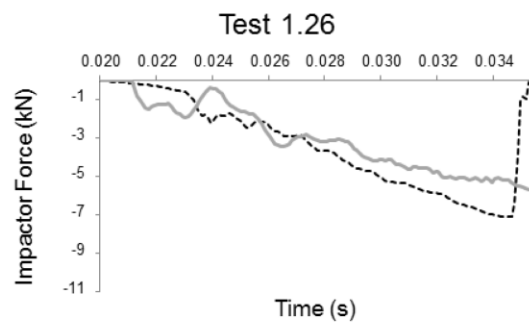
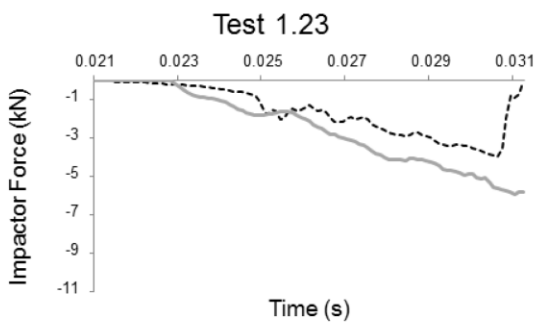
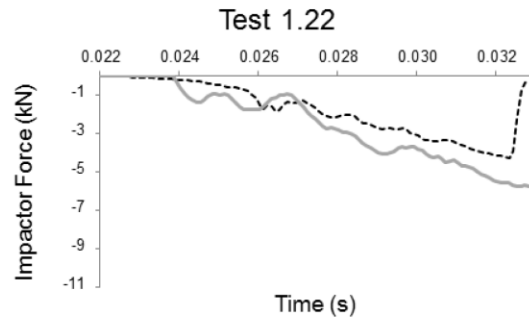
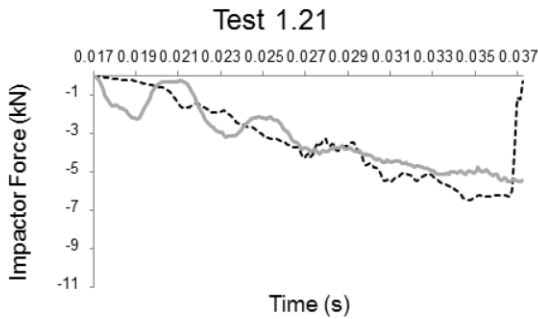
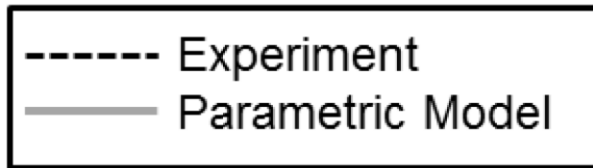
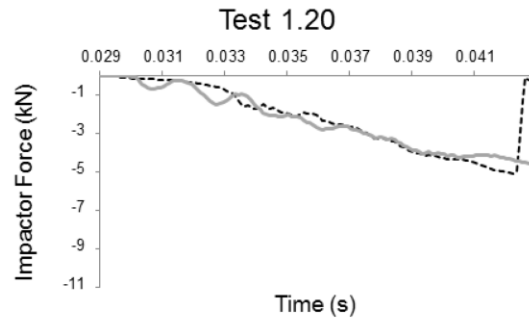
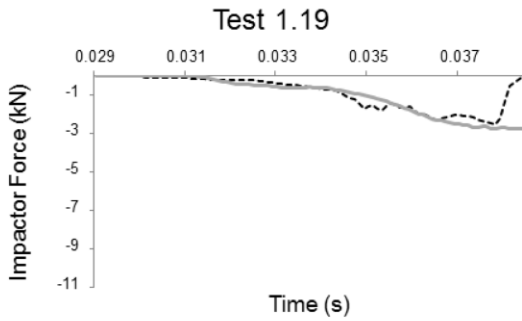
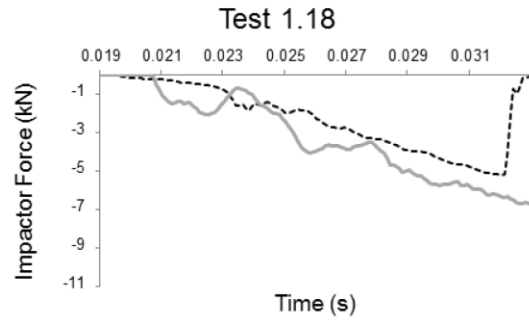
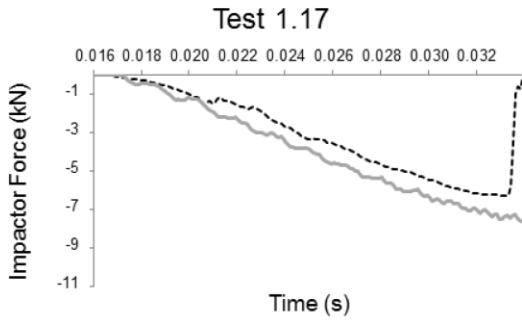
Table C-3. Percent differences between slope values for experimentally measured and parametric simulations from time of contact until time of failure

Test ID	Subject ID	Femur Side	Gender	Test Slope (kN/s)	Parametric Slope (kN/s)	Percent Difference	Absolute Percent Difference
1.01	373	L	M	-173	-138	-20	20
1.02	373	R	M	-225	-174	-23	23
1.03	374	L	M	-516	-611	18	18
1.04	374	R	M	-450	-393	-13	13
1.05	375	L	M	-615	-659	7	7
1.06	375	R	M	-643	-634	-1	1
1.07	376	L	M	-534	-464	-13	13
1.08	376	R	M	-469	-353	-25	25
1.09	377	R	M	-560	-688	23	23
1.10	378	L	M	-375	-235	-37	37
1.11	378	R	M	-524	-446	-15	15
1.12	379	L	M	-638	-715	12	12
1.13	379	R	M	-709	-593	-16	16
1.14	380	L	M	-405	-587	45	45
1.15	380	R	M	-331	-393	19	19
1.16	381	L	M	-367	-378	3	3
1.17	381	R	M	-450	-498	11	11
1.18	382	L	F	-476	-526	11	11
1.19	382	R	F	-368	-397	8	8
1.20	383	L	F	-468	-403	-14	14
1.21	383	R	F	-362	-304	-16	16
1.22	387	L	F	-497	-592	19	19
1.23	387	R	F	-486	-665	37	37
1.26	389	L	F	-562	-407	-28	28
1.27	389	R	F	-604	-523	-13	13
Mean				-472	-471	-1	18
SD				128	159	21	10

APPENDIX D







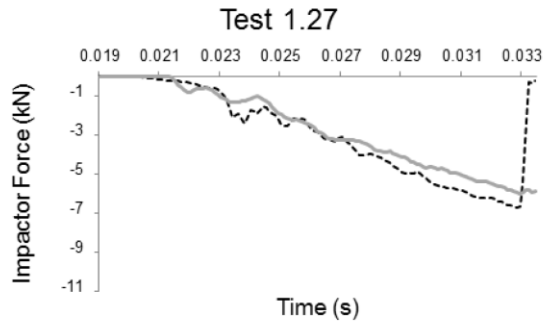






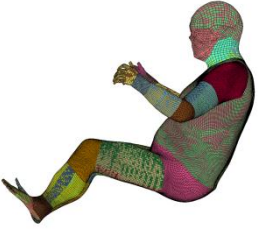




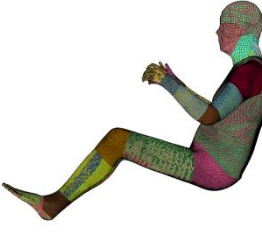





Figure D-1. Impactor force histories for the parametric model simulations compared to the experimentally measured results.

APPENDIX E

Table E-4. Examples of male morphed models

	Stature 1.636 m	Stature 1.763 m	Stature 1.887 m
Age 25, BMI 25			
Age 25, BMI 30			
Age 25, BMI 35			
Age 50, BMI 25			
Age 50, BMI 30			























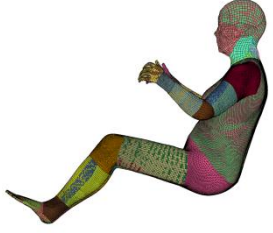
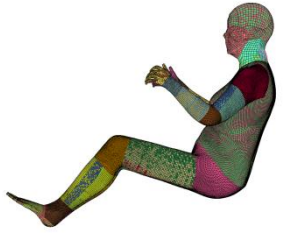

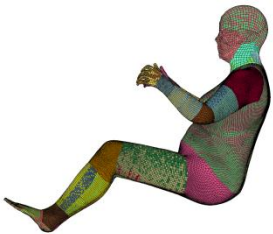













Age 50, BMI 35			
Age 75, BMI 25			
Age 75, BMI 30			
Age 75, BMI 35			

Table E-5. Examples of female morphed models

	Stature 1.507 m	Stature 1.622 m	Stature 1.731 m
Age 25, BMI 25			
Age 25, BMI 30			
Age 25, BMI 35			
Age 50, BMI 25			
Age 50, BMI 30			

Age 50, BMI 35			
Age 75, BMI 25			
Age 75, BMI 30			
Age 75, BMI 35			

APPENDIX F

Table F-6. List of subject characteristics

Female Models				Male Models			
Female Test ID	Age (years)	BMI (kg/m ²)	Stature (m)	Male Test ID	Age (years)	BMI (kg/m ²)	Stature (m)
F1	25	25	1.507	M1	25	25	1.636
F2	25	25	1.622	M2	25	25	1.763
F3	25	25	1.731	M3	25	25	1.887
F4	25	30	1.507	M4	25	30	1.636
F5	25	30	1.622	M5	25	30	1.763
F6	25	30	1.731	M6	25	30	1.887
F7	25	35	1.507	M7	25	35	1.636
F8	25	35	1.622	M8	25	35	1.763
F9	25	35	1.731	M9	25	35	1.887
F10	50	25	1.507	M10	50	25	1.636
F11	50	25	1.622	M11	50	25	1.763
F12	50	25	1.731	M12	50	25	1.887
F13	50	30	1.507	M13	50	30	1.636
F14	50	30	1.622	M14	50	30	1.763
F15	50	30	1.731	M15	50	30	1.887
F16	50	35	1.507	M16	50	35	1.636
F17	50	35	1.622	M17	50	35	1.763
F18	50	35	1.731	M18	50	35	1.887
F19	75	25	1.507	M19	75	25	1.636
F20	75	25	1.622	M20	75	25	1.763
F21	75	25	1.731	M21	75	25	1.887
F22	75	30	1.507	M22	75	30	1.636
F23	75	30	1.622	M23	75	30	1.763
F24	75	30	1.731	M24	75	30	1.887
F25	75	35	1.507	M25	75	35	1.636
F26	75	35	1.622	M26	75	35	1.763
F27	75	35	1.731	M27	75	35	1.887

APPENDIX G

Table G-7. Percent differences between peak impactor forces for experimentally measured test results and parametric, scaled, midsize, specimen-specific, and specimen-specific with yield stress fit femur simulations at time of failure

					Parametric Models		Scaled Models		Midsize Models		Specimen-specific Models		Yield Stress Fit Models	
Test ID	Subject ID	Femur Side	Sex	Test Force (kN)	Force (kN)	% Diff.	Force (kN)	% Diff.	Force (kN)	% Diff.	Force (kN)	% Diff.	Force (kN)	% Diff.
1.01	373	L	M	-5.00	-4.26	-15	-4.50	-10	-4.24	-15	-3.28	-34	-3.28	-34
1.02	373	R	M	-2.48	-2.18	-12	-1.36	-45	-1.27	-49	-1.79	-28	-2.21	-11
1.03	374	L	M	-3.78	-4.58	21	-3.21	-15	-3.62	-4	-2.89	-23	-2.89	-23
1.04	374	R	M	-6.88	-6.59	-4	-4.43	-36	-4.38	-36	-7.21	5	-6.59	-4
1.05	375	L	M	-5.48	-6.14	12	-4.32	-21	-4.08	-26	-6.09	11	-6.07	11
1.06	375	R	M	-7.40	-7.71	4	-5.45	-26	-5.47	-26	-7.26	-2	-7.71	4
1.07	376	L	M	-5.44	-4.67	-14	-5.33	-2	-4.11	-24	-4.30	-21	-3.71	-32
1.08	376	R	M	-7.47	-5.80	-22	-6.68	-11	-4.35	-42	-5.50	-26	-4.86	-35
1.09	377	R	M	-6.31	-7.87	25	-6.12	-3	-5.84	-7	-7.54	19	-8.16	29
1.10	378	L	M	-6.23	-4.65	-25	-5.32	-15	-4.16	-33	-3.40	-45	-3.62	-42
1.11	378	R	M	-6.66	-6.30	-5	-6.08	-9	-5.32	-20	-5.67	-15	-6.74	1
1.12	379	L	M	-9.66	-10.53	9	-6.61	-32	-6.65	-31	-11.91	23	-10.89	13
1.13	379	R	M	-9.70	-8.44	-13	-6.03	-38	-4.65	-52	-8.88	-8	-8.08	-17
1.14	380	L	M	-5.47	-7.81	43	-5.79	6	-4.88	-11	-4.61	-16	-4.66	-15
1.15	380	R	M	-3.58	-4.48	25	-2.81	-21	-2.46	-31	-2.23	-38	-4.84	35
1.16	381	L	M	-6.18	-6.79	10	-5.65	-8	-5.44	-12	-5.18	-16	-5.26	-15
1.17	381	R	M	-6.30	-7.64	21	-6.11	-3	-5.68	-10	-5.78	-8	-7.72	22
1.18	382	L	F	-5.21	-6.71	29	-4.53	-13	-5.01	-4	-5.31	2	-5.41	4
1.19	382	R	F	-2.56	-2.78	8	-1.89	-26	-2.09	-19	-2.25	-12	-3.30	29
1.20	383	L	F	-5.07	-4.54	-10	-3.95	-22	-4.86	-4	-3.07	-40	-3.16	-38
1.21	383	R	F	-6.48	-5.53	-15	-4.89	-25	-5.66	-13	-4.21	-35	-6.66	3
1.22	387	L	F	-4.30	-5.77	34	-4.34	1	-4.70	9	-4.25	-1	-4.02	-6
1.23	387	R	F	-3.97	-5.91	49	-2.88	-28	-3.41	-14	-2.92	-27	-5.70	44
1.26	389	L	F	-7.09	-5.67	-20	-4.78	-33	-5.47	-23	-6.03	-15	-5.83	-18
1.27	389	R	F	-6.69	-5.99	-10	-5.40	-19	-5.76	-14	-6.13	-8	-6.00	-10
Mean				-5.8	-6.0	5	-4.7	-18	-4.5	-20	-5.1	-14	-5.5	-4
SD				1.8	1.8	21	1.4	13	1.3	15	2.3	18	2.0	24

Table G-8. Absolute percent differences between peak impactor forces for experimentally measured test results and parametric, scaled, midsize, specimen-specific, and specimen-specific with yield stress fit femur simulations at time of failure

Test ID	Subject ID	Femur Side	Sex	Test Force (kN)	Parametric Models		Scaled Models		Midsize Models		Specimen-specific Models		Yield Stress Fit Models	
					Force (kN)	% Diff.	Force (kN)	% Diff.	Force (kN)	% Diff.	Force (kN)	% Diff.	Force (kN)	% Diff.
1.01	373	L	M	-5.00	-4.26	15	-4.50	10	-4.24	15	-3.28	34	-3.28	34
1.02	373	R	M	-2.48	-2.18	12	-1.36	45	-1.27	49	-1.79	28	-2.21	11
1.03	374	L	M	-3.78	-4.58	21	-3.21	15	-3.62	4	-2.89	23	-2.89	23
1.04	374	R	M	-6.88	-6.59	4	-4.43	36	-4.38	36	-7.21	5	-6.59	4
1.05	375	L	M	-5.48	-6.14	12	-4.32	21	-4.08	26	-6.09	11	-6.07	11
1.06	375	R	M	-7.40	-7.71	4	-5.45	26	-5.47	26	-7.26	2	-7.71	4
1.07	376	L	M	-5.44	-4.67	14	-5.33	2	-4.11	24	-4.30	21	-3.71	32
1.08	376	R	M	-7.47	-5.80	22	-6.68	11	-4.35	42	-5.50	26	-4.86	35
1.09	377	R	M	-6.31	-7.87	25	-6.12	3	-5.84	7	-7.54	19	-8.16	29
1.10	378	L	M	-6.23	-4.65	25	-5.32	15	-4.16	33	-3.40	45	-3.62	42
1.11	378	R	M	-6.66	-6.30	5	-6.08	9	-5.32	20	-5.67	15	-6.74	1
1.12	379	L	M	-9.66	-10.53	9	-6.61	32	-6.65	31	-11.91	23	-10.89	13
1.13	379	R	M	-9.70	-8.44	13	-6.03	38	-4.65	52	-8.88	8	-8.08	17
1.14	380	L	M	-5.47	-7.81	43	-5.79	6	-4.88	11	-4.61	16	-4.66	15
1.15	380	R	M	-3.58	-4.48	25	-2.81	21	-2.46	31	-2.23	38	-4.84	35
1.16	381	L	M	-6.18	-6.79	10	-5.65	8	-5.44	12	-5.18	16	-5.26	15
1.17	381	R	M	-6.30	-7.64	21	-6.11	3	-5.68	10	-5.78	8	-7.72	22
1.18	382	L	F	-5.21	-6.71	29	-4.53	13	-5.01	4	-5.31	2	-5.41	4
1.19	382	R	F	-2.56	-2.78	8	-1.89	26	-2.09	19	-2.25	12	-3.30	29
1.20	383	L	F	-5.07	-4.54	10	-3.95	22	-4.86	4	-3.07	40	-3.16	38
1.21	383	R	F	-6.48	-5.53	15	-4.89	25	-5.66	13	-4.21	35	-6.66	3
1.22	387	L	F	-4.30	-5.77	34	-4.34	1	-4.70	9	-4.25	1	-4.02	6
1.23	387	R	F	-3.97	-5.91	49	-2.88	28	-3.41	14	-2.92	27	-5.70	44
1.26	389	L	F	-7.09	-5.67	20	-4.78	33	-5.47	23	-6.03	15	-5.83	18
1.27	389	R	F	-6.69	-5.99	10	-5.40	19	-5.76	14	-6.13	8	-6.00	10
Mean				-5.8	-6.0	18	-4.7	19	-4.5	21	-5.1	19	-5.5	20
SD				1.8	1.8	12	1.4	1	1.3	14	2.3	13	2.0	13

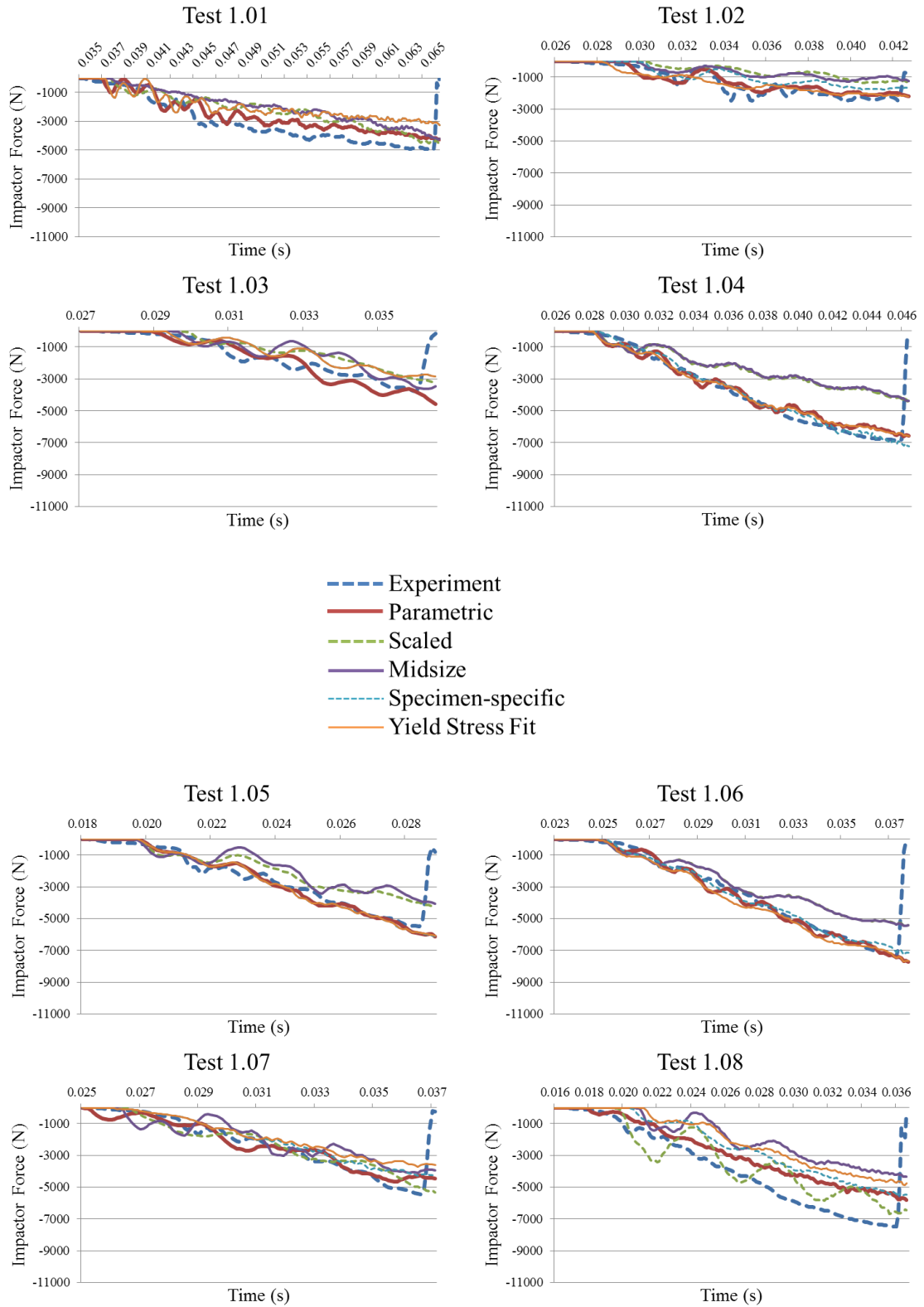
Table G-9. Percent differences between slope values for experimentally measured test results and parametric, scaled, midsize, specimen-specific, and specimen-specific with yield stress fit femur simulations from time of contact until time of failure

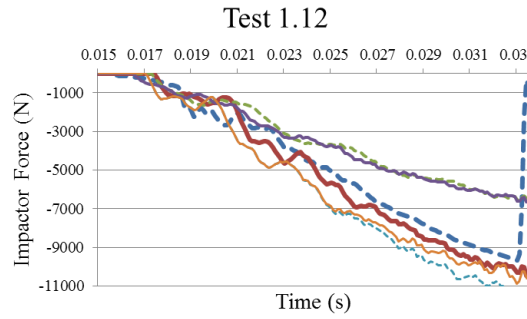
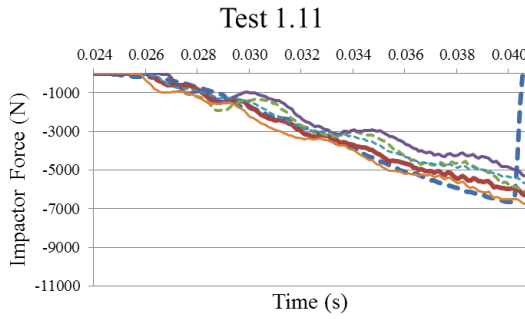
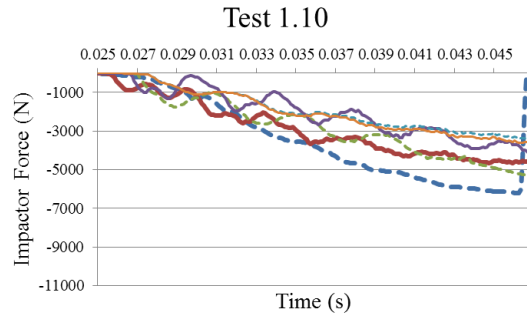
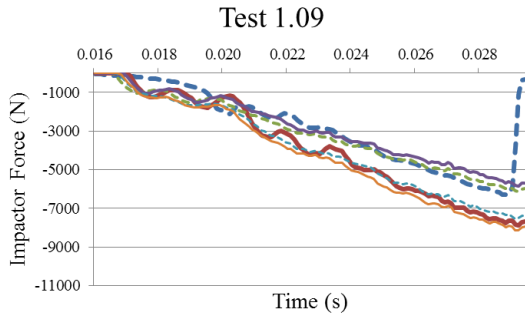
Test ID	Subject ID	Femur Side	Sex	Test Slope (kN/s)	Parametric Models		Scaled Models		Midsize Models		Specimen-specific Models		Yield Stress Fit Models	
					Slope (kN/s)	% Diff.	Slope (kN/s)	% Diff.	Slope (kN/s)	% Diff.	Slope (kN/s)	% Diff.	Slope (kN/s)	% Diff.
1.01	373	L	M	-173	-138	-20	-124	-28	-125	-28	-92	-47	-92	-47
1.02	373	R	M	-225	-174	-23	-81	-64	-93	-59	-156	-31	-190	-16
1.03	374	L	M	-516	-611	18	-404	-22	-413	-20	-406	-21	-406	-21
1.04	374	R	M	-450	-393	-13	-215	-52	-212	-53	-441	-2	-390	-13
1.05	375	L	M	-615	-659	7	-421	-32	-387	-37	-674	10	-674	10
1.06	375	R	M	-643	-634	-1	-442	-31	-442	-31	-606	-6	-624	-3
1.07	376	L	M	-534	-464	-13	-386	-28	-360	-33	-458	-14	-388	-27
1.08	376	R	M	-469	-353	-25	-332	-29	-269	-43	-362	-23	-330	-30
1.09	377	R	M	-560	-688	23	-479	-15	-459	-18	-620	11	-681	22
1.10	378	L	M	-375	-235	-37	-226	-40	-190	-49	-173	-54	-187	-50
1.11	378	R	M	-524	-446	-15	-373	-29	-346	-34	-398	-24	-450	-14
1.12	379	L	M	-638	-715	12	-412	-35	-415	-35	-776	22	-713	12
1.13	379	R	M	-709	-593	-16	-436	-39	-348	-51	-659	-7	-579	-18
1.14	380	L	M	-405	-587	45	-389	-4	-350	-14	-347	-14	-348	-14
1.15	380	R	M	-331	-393	19	-227	-31	-166	-50	-147	-56	-380	15
1.16	381	L	M	-367	-378	3	-289	-21	-289	-21	-284	-23	-286	-22
1.17	381	R	M	-450	-498	11	-414	-8	-380	-16	-380	-16	-498	11
1.18	382	L	F	-476	-526	11	-345	-27	-370	-22	-404	-15	-407	-15
1.19	382	R	F	-368	-397	8	-216	-41	-245	-33	-291	-21	-436	18
1.20	383	L	F	-468	-403	-14	-308	-34	-335	-28	-257	-45	-264	-44
1.21	383	R	F	-362	-304	-16	-264	-27	-298	-18	-213	-41	-389	7
1.22	387	L	F	-497	-592	19	-429	-14	-480	-4	-436	-12	-425	-14
1.23	387	R	F	-486	-665	37	-274	-44	-367	-25	-335	-31	-652	34
1.26	389	L	F	-562	-407	-28	-336	-40	-371	-34	-438	-22	-431	-23
1.27	389	R	F	-604	-523	-13	-445	-26	-466	-23	-518	-14	-509	-16
Mean				-472	-471	-1	-331	-31	-327	-31	-395	-20	-429	-10
SD				128	159	21	105	13	106	14	177	19	162	22

Table G-10. Absolute percent differences between slope values for experimentally measured test results and parametric, scaled, midsize, specimen-specific, and specimen-specific with yield stress fit femur simulations from time of contact until time of failure

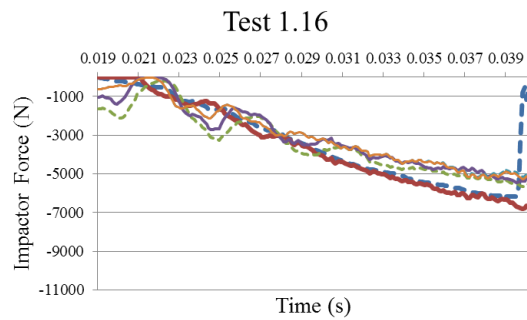
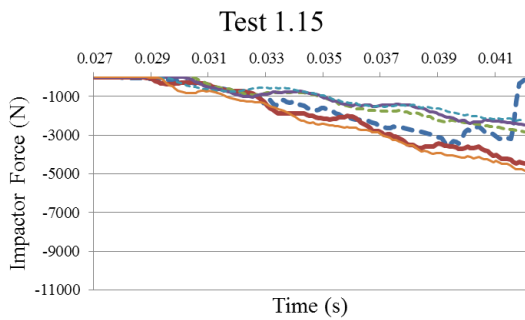
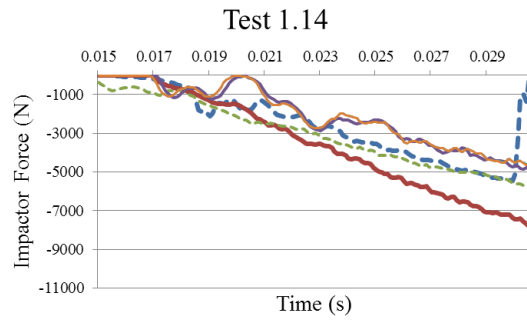
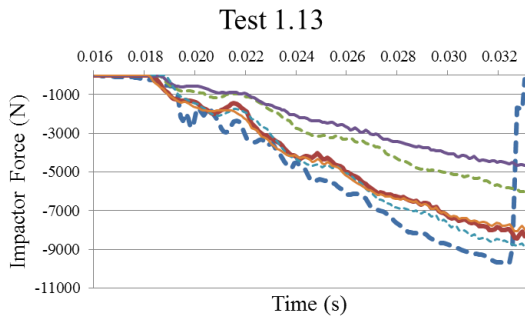
Test ID	Subject ID	Femur Side	Sex	Test Slope (kN/s)	Parametric Models		Scaled Models		Midsize Models		Specimen-specific Models		Yield Stress Fit Models	
					Slope (kN/s)	% Diff.	Slope (kN/s)	% Diff.	Slope (kN/s)	% Diff.	Slope (kN/s)	% Diff.	Slope (kN/s)	% Diff.
1.01	373	L	M	-173	-138	20	-124	28	-125	28	-92	47	-92	47
1.02	373	R	M	-225	-174	23	-81	64	-93	59	-156	31	-190	16
1.03	374	L	M	-516	-611	18	-404	22	-413	20	-406	21	-406	21
1.04	374	R	M	-450	-393	13	-215	52	-212	53	-441	2	-390	13
1.05	375	L	M	-615	-659	7	-421	32	-387	37	-674	10	-674	10
1.06	375	R	M	-643	-634	1	-442	31	-442	31	-606	6	-624	3
1.07	376	L	M	-534	-464	13	-386	28	-360	33	-458	14	-388	27
1.08	376	R	M	-469	-353	25	-332	29	-269	43	-362	23	-330	30
1.09	377	R	M	-560	-688	23	-479	15	-459	18	-620	11	-681	22
1.10	378	L	M	-375	-235	37	-226	40	-190	49	-173	54	-187	50
1.11	378	R	M	-524	-446	15	-373	29	-346	34	-398	24	-450	14
1.12	379	L	M	-638	-715	12	-412	35	-415	35	-776	22	-713	12
1.13	379	R	M	-709	-593	16	-436	39	-348	51	-659	7	-579	18
1.14	380	L	M	-405	-587	45	-389	4	-350	14	-347	14	-348	14
1.15	380	R	M	-331	-393	19	-227	31	-166	50	-147	56	-380	15
1.16	381	L	M	-367	-378	3	-289	21	-289	21	-284	23	-286	22
1.17	381	R	M	-450	-498	11	-414	8	-380	16	-380	16	-498	11
1.18	382	L	F	-476	-526	11	-345	27	-370	22	-404	15	-407	15
1.19	382	R	F	-368	-397	8	-216	41	-245	33	-291	21	-436	18
1.20	383	L	F	-468	-403	14	-308	34	-335	28	-257	45	-264	44
1.21	383	R	F	-362	-304	16	-264	27	-298	18	-213	41	-389	7
1.22	387	L	F	-497	-592	19	-429	14	-480	4	-436	12	-425	14
1.23	387	R	F	-486	-665	37	-274	44	-367	25	-335	31	-652	34
1.26	389	L	F	-562	-407	28	-336	40	-371	34	-438	22	-431	23
1.27	389	R	F	-604	-523	13	-445	26	-466	23	-518	14	-509	16
Mean				-472	-471	18	-331	31	-327	31	-395	23	-429	21
SD				128	159	10	105	13	106	14	177	15	162	12

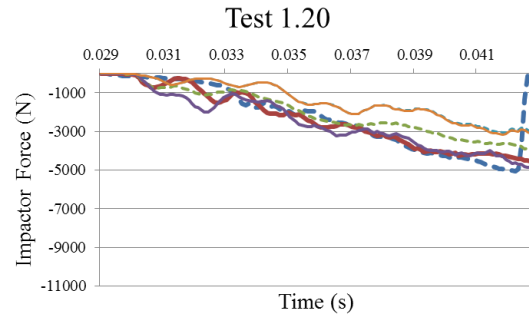
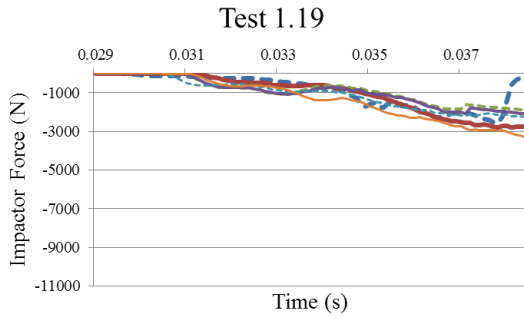
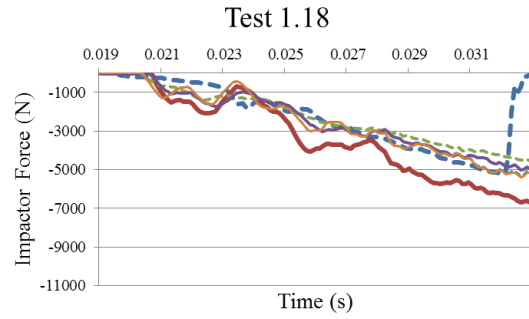
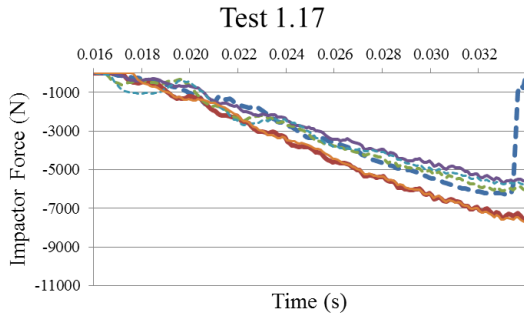
APPENDIX H



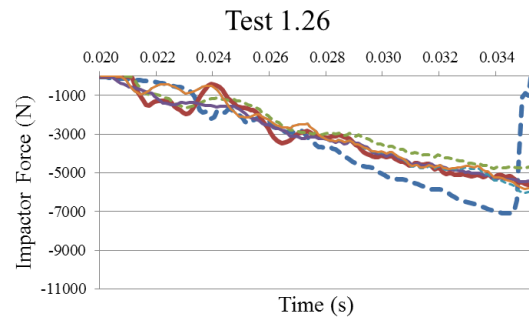
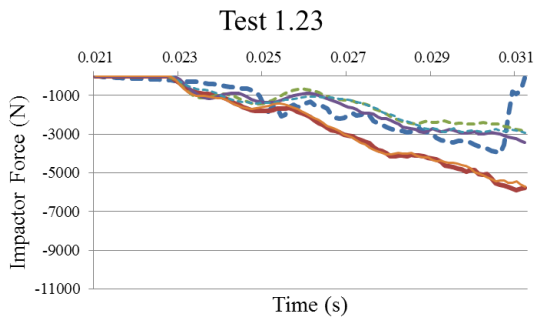
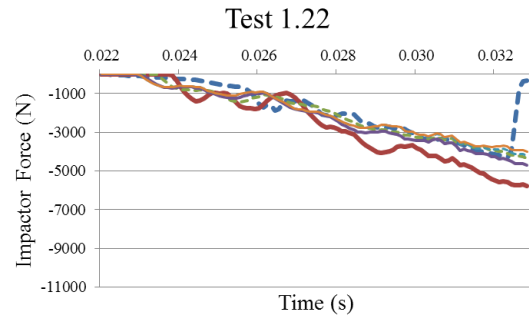
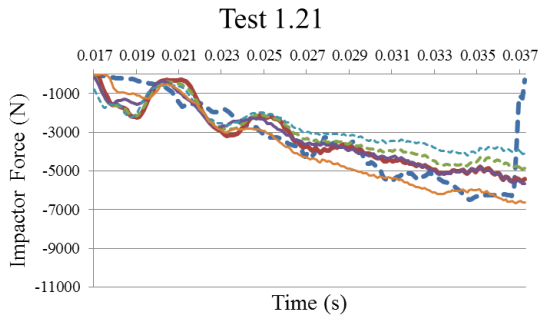


- Experiment
- Parametric
- - - Scaled
- Midsize
- · - · Specimen-specific
- Yield Stress Fit





- Experiment
- Parametric
- - - Scaled
- Midsized
- · · Specimen-specific
- Yield Stress Fit



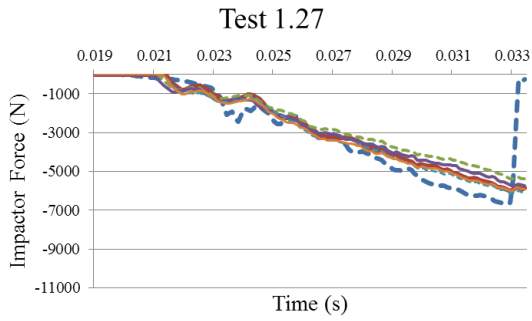


Figure H-2. Time histories of impactor forces for the parametric model simulations, scaled THUMS 4, midsized THUMS 4, specimen-specific, and specimen-specific with yield stress fit simulations compared to the experimentally measured test results.

References

- Akaike, H., 1974. A new look at the statistical model identification. *IEEE Transactions on Automatic Control* AC19, 716-723.
- Beason, D.P., Dakin, G.J., Lopez, R.R., Alonso, J.E., Bandak, F.A. and Eberhardt, A.W., 2003. Bone mineral density correlates with fracture load in experimental side impacts of the pelvis. *Journal of Biomechanics* 36, 219-227.
- Bennink, H.E., Korbeeck, J.M., Janssen, B.J. and ter Haar Romeny, B.M., 2006. Warping a neuro-anatomy atlas on 3D MRI data with radial basis functions. *Proc. International Conference on Biomedical Engineering* 3, 214-218.
- Besnault, B., Lavaste, F., Guillemot, H., Robin, S. and Le Coz, J.Y., 1998. A parametric finite element model of the human pelvis. *Proc. Stapp Car Crash Conference* 42, P-337.
- Blincoe, L., Seay, A., Zaloshnja, E., Miller, T., Romano, E., Luchter, S. and Spicer, R., 2002. The economic impact of motor vehicle crashes 2000. *NHTSA Technical Report*.
- Bredbenner, T.L., Mason, R.L., Havill, L.M., Orwoll E.S., and Nicoletta, D. P., 2014. Fracture risk predictions based on statistical shape and density modeling of the proximal femur. *Journal of Bone and Mineral Research* 29, 2090-2100.
- Bryan, R., Mohan, P.S., Hopkins, A., Galloway, F., Taylor, M. and Nair, P.B., 2010. Statistical modelling of the whole human femur incorporating geometric and material properties. *Medical Engineering & Physics* 32, 57-65.
- Bryan, R., Nair, P.B. and Taylor, M., 2009. Use of a statistical model of the whole femur in a large scale, multi-model study of femoral neck fracture risk. *Journal of Biomechanics* 42, 2171-2176.

- Burstein, A.H., Reilly, D.T. and Martens, M., 1976. Aging of bone tissue: mechanical properties. *Journal of Bone and Joint Surgery* 58, 82-86.
- Carr, J.C., Beatson, R.K., Cherrie, J.B., Mitchell, T.J., Fright, W.R., McCallum, B.C. and Evans, T.R., 2001. Reconstruction and representation of 3D objects with radial basis functions. *Proc. Annual Conference on Computer Graphics and Interactive Techniques* 28, 67-76.
- Carter, P.M., Flannagan, C.A.C., Reed, M.P., Cunningham, R.M. and Rupp, J.D., 2014. Comparing the effects of age, BMI and gender on severe injury (AIS 3+) in motor-vehicle crashes. *Accident Analysis and Prevention* 72, 146-160.
- Chang, C.-Y., Rupp, J.D., Reed, M.P., Hughes, R.E., and Schneider, L.W., 2009. Prediction of the effect of lower-extremity muscle forces on knee, thigh, and hip injuries in frontal motor vehicle crashes. *Proc. Stapp Car Crash Conference* 53, 291-328.
- Chong, M., Sochor, M.M., Ipaktchi, K., Brede, C., Poster, C. and Wang, S.C., 2007. The interaction of 'occupant factors' on the lower extremity fractures in frontal collision of motor vehicle crashes based on a level I trauma center. *The Journal of Trauma* 62, 720-729.
- Clarke, B., 2008. Normal bone anatomy and physiology. *Clinical Journal of the American Society of Nephrology* CJASN 3 Suppl 3, S131-139.
- Crandall, J.R., Martin, P.G., Bass, C.R., Pilkey, W.D., Dischinger, P.C., Burgess, A.R., O'Quinn, T.D., and Schmidhauser, C.B., 1996. Foot and ankle injury: the roles of driver anthropometry, footwear and pedal controls. *Proc. Association for the Advancement of Automotive Medicine* 40, 1-18.
- Dischinger, P.C., Kerns, T.J. and Kufera, J.A., 1995. Lower extremity fractures in motor vehicle collisions: the role of driver gender and height. *Accident Analysis and Prevention* 27, 601-606.
- Dokko, Y., Ito, O. and Ohashi, K., 2009. Development of human lower limb and pelvis FE models for adult and the elderly. *SAE International*.

Eppinger, R.H., Marcus, J.H., and Morgan, R.M., 1984. Development of dummy and injury index for NHTSA's thoracic side impact protection research program. *Proc. SAE Government/Industry Meeting* 983-1011.

Gayzik, F.S., Yu, M.M., Danelson, K.A., Slice, D.E. and Stitzel, J.D., 2008. Quantification of age-related shape change of the human rib cage through geometric morphometrics. *Journal of Biomechanics* 41, 1545-1554.

Heaney, R.P., 2003. Is the paradigm shifting? *Bone* 33, 457-46.

Hu, J., Rupp, J.D. and Reed, M.P., 2012. Focusing on vulnerable populations in crashes: recent advances in finite element human models for injury biomechanics research. *Journal of Automotive Safety and Energy* 3, 295-307.

Hwang, E., Wang, Y., Reed, M.P., Rupp, J.D. and Hu, J., 2014. Parametric human body modeling: development and application of new methods for rapid development of diverse human models for crash simulation. *UMTRI Report*.

Ivarsson, B.J., Genovese, D., Crandall, J.R., Bolton, J.R., Untaroiu, C.D. and Bose, D., 2009. The tolerance of the femoral shaft in combined axial compression and bending loading. *Proc. Stapp Car Crash Conference* 53, 251-290.

Iwamoto, M., Hasegawa, J., Miki, K., Furuu, K. and Watanabe, I., 2002. Development of a finite element model of the total human model for safety (THUMS) and application to injury reconstruction. *Proc. International Conference on the Biomechanics of Impacts*.

Joliffe, I.T., 2002. *Principal component analysis*. Springer, ed.

Keaveny, T.M., Hoffmann, P.F., Singh, M., Palermo, L., Bilezikian, J.P., Greenspan, S.L., and Black, D.M., 2008. Femoral bone strength and its relation to cortical and trabecular changes after treatment with PTH, alendronate, and their combination as assessed by finite element analysis of quantitative CT scans. *Journal of Bone and Mineral Research* 23, 1974-1982.

Kent, R.W., Forman, J.L. and Bostrom, O., 2010. Is there really a "cushion effect"? a biomechanical investigation of crash injury mechanisms in the obese. *Obesity* 18, 749-753.

Kent, R.W., Lee, S.H., Darvish, K., Wang, S.C., Poster, C.S., Lange, A.W., Brede, C., Lange, D. and Matsuoka, F., 2005. Structural and material changes in the aging thorax and their role in crash protection for older occupants. *Proc. Stapp Car Crash Conference* 49, 231-249.

Kent, R., Patrie, J., Poteau, F., Matsuoka, F., and Mullen, C., 2003. Development of an age dependent thoracic injury criterion for frontal impact restraint loading. *Paper No. 72*.

Keyak, J.H. and Falkinstein, Y., 2003. Comparison of in situ and in vitro CT scan-based finite element model predictions of proximal femoral fracture load. *Medical Engineering & Physics* 25, 781-787.

Kim, Y.S., Choi, H.H., Cho, Y.N., Park, Y.J., Lee, J.B., Yang, K.H., and King, A.I., 2005. Numerical investigations of interactions between the knee-thigh-hip complex with vehicle interior structures. *Proc. Stapp Car Crash Conference* 49, 85-115.

Kimpara, H., Lee, J.B., Yang, K.H., and King, A.I., 2010. Effects of body weight, height, and rib cage area moment of inertia on blunt chest impact response. *Traffic Injury Prevention* 11, 207-214.

Kimpara, H., Lee, J.B., Yang, K.H., King, A.I., Iwamoto, M., Watanabe, I. and Miki, K., 2005. Development of a three dimensional finite element chest model for the 5th percentile female. *Proc. Stapp Car Crash Conference* 49, 251-269.

Klein, K.F., Hu, J., Reed, M.P., Hoff, C.N. and Rupp, J.D., 2015. Development and validation of statistical models of femur geometry for use with parametric finite element models. *Annals of Biomedical Engineering*.

Kuppa, S. and Fessahaie, O., 2003. An overview of knee-thigh-hip injuries in frontal crashes in the united states. *Proc. of the International Technical Conference on the Enhanced Safety of Vehicles* 18.

Kurazume, R., Nakamura, K., Okada, T., Sato, Y., Sugano, N., Koyama, T., Iwashita, Y. and Hasegawa, T., 2009. 3D reconstruction of a femoral shape using a parametric model and two 2D fluoroscopic images. *Computer Vision and Image Understanding* 113, 202-211.

- Li, Z., Hu, J., Reed, M.P., Rupp, J.D., Hoff, C.N., Zhang, J. and Cheng, B., 2011. Development, validation, and application of a parametric pediatric head finite element model for impact simulations. *Annals of Biomedical Engineering* 39, 2984-2997.
- Lu, Y.C., Kemper, A.R., Gayzik, F.S., Untaroiu, C.D. and Beillas, P., 2013. Statistical modeling of human liver incorporating the variations in shape, size, and material properties. *Proc. Stapp Car Crash Conference* 57, 285-311.
- Lu, Y.C. and Untaroiu, C.D., 2013. Statistical shape analysis of clavicular cortical bone with applications to the development of mean and boundary shape models. *Computer Methods and Programs in Biomedicine* 111, 613-628.
- Maltese, M.R., Eppinger, R.H., Rhule, H.H. and Donnelly, B.R., 2002. Response corridors of human surrogates in lateral impacts. *Proc. Stapp Car Crash Conference* 46, 321-351.
- Manary, M.A., Reed, M.P., Flannagan, C.A.C. and Schneider, L.W., 1998. ATD positioning based on driver posture and position. *Proc. Stapp Car Crash Conference* 42, P-337.
- Moran, S.G., McGwin, G., Jr., Metzger, J.S., Alonso, J.E. and Rue, L.W., 3rd, 2003. Relationship between age and lower extremity fractures in frontal motor vehicle collisions. *The Journal of Trauma* 54, 261-265.
- Nalla, R.K., Kruzic, J.J., Kinney, J.H. and Ritchie, R.O., 2004. Effect of aging on the toughness of human cortical bone: evaluation by R-curves. *Bone* 35, 1240-1246.
- Nicolella, D.P. and Bredbenner, T.L., 2012. Development of a parametric finite element model of the proximal femur using statistical shape and density modeling. *Computer Methods in Biomechanics and Biomedical Engineering* 15, 101-110.
- Read, K.M., Kufera, J.A., Dischinger, P.C., Kerns, T.J., Ho, S.M., Burgess, A.R. and Burch, C.A., 2004. Life-altering outcomes after lower extremity injury sustained in motor vehicle crashes. *The Journal of Trauma: Injury, Infection, and Critical Care* 57, 815-823.
- Reed, M.P., Ebert, S.M., and Hallman, J.J., 2013. Effects of driver characteristics on seat belt fit. *Proc. Stapp Car Crash Conference* 57, 43-57.

- Reed, M.P., Ebert-Hamilton, S.M., and Rupp, J.D., 2012. Effects of obesity on seat belt fit. *Traffic Injury Prevention* 13, 364-372.
- Reed, M.P., Sochor, M.M., Rupp, J.D., Klinich, K.D., and Manary, M.A., 2009. Anthropometric specification of child crash dummy pelves through statistical analysis of skeletal geometry. *Journal of Biomechanics* 42, 1143-1145.
- Reed, M.P. and Parkinson, M.B., 2008. Modeling variability in torso shape for chair and seat design. *Proc. of the ASME Design Engineering Technical Conferences*, 1-9.
- Reed, M.P., 1998. Statistical and biomechanical prediction of automobile driving posture. University of Michigan.
- Ridella, S.A., Beyersmith, A. and Poland, K., 2011. Factors associated with age-related differences in crash injury types, causation, and mechanisms. *Proc. of Emerging Issues in Safe and Sustainable Mobility for Older Persons TRB ANB60 Fall 2011 Conference*, Washington, D.C.
- Riggs, B.L., Melton III, L.J., Robb, R.A., Camp, J.J., Atkinson, E.J., Peterson, J.M., Rouleau, P.A., McCollough, C.H., Bouxsein, M.L. and Khosla, S., 2004. Population-based study of age and sex differences in bone volumetric density, size, geometry, and structure at different skeletal sites. *Journal of Bone and Mineral Research* 19, 1945-1954.
- Robin, S., 2001. HUMOS: human model for safety– a joint effort towards the development of refined human-like car occupants models. *Proc. International Technical Conference on the Enhanced Safety of Vehicles* 17.
- Ruan, J.S., El-Jawahri, R., Barbat, S., Rouhana, S.W. and Prasad, P., 2008. Impact response and biomechanical analysis of the knee-thigh-hip complex in frontal impacts. *Proc. Stapp Car Crash Conference* 52, 505-526.
- Rudd, R.W., 2009. Updated analysis of lower extremity injury risk in frontal crashes in the united states. *Proc. International Technical Conference on the Enhanced Safety of Vehicles* 21.
- Rupp, J.D. and Flannagan, C.A.C., 2011. Effects of occupant age on AIS 3+ injury outcome determined from analyses of fused NASS/CIREN data. *SAE 2011 Government/Industry Meeting*, Washington, D.C.

Rupp, J.D., Miller, C.S., Reed, M.P., Madura, N.H., Klinich, K.D. and Schneider, L.W., 2008. Characterization of knee-thigh-hip response in frontal impacts using biomechanical testing and computational simulations. *Proc. Stapp Car Crash Conference* 52, 421-474.

Scarboro, M., McCullough, C. and Sarda, P., 2005. Crash injuries and long term consequences: the CIREN experience. *Proc. International Technical Conference on the Enhanced Safety of Vehicles* 19.

Schneider, L.W., Robbins, D.H., Flug, M.A., and Snyder, R.G., 1983. Development of anthropometrically based design specifications for an advanced adult anthropomorphic dummy family. *UMTRI Report 83-53-1*. Volumes 1-3.

Shi, X., Cao, L., Reed, M.P., Rupp, J.D., Hoff, C.N. and Hu, J., 2014. A statistical human rib cage geometry model accounting for variations by age, sex, stature and body mass index. *Journal of Biomechanics* 14, 2277-2285.

Shi, X., Cao, L., Reed, M.P., Rupp, J.D. and Hu, J., 2015. Effects of obesity on occupant responses in frontal crashes: a simulation analysis using human body models. *Computer Methods in Biomechanics and Biomedical Engineering* 18, 1280-1292.

Silvestri, C. and Ray, M.H., 2009. Development of a finite element model of the knee-thigh-hip of a 50th percentile male including ligaments and muscles. *International Journal of Crashworthiness* 14, 215-229.

Slice, D.E., 2007. Geometric morphometrics. *Annual Review of Anthropology* 36, 261-281.

Torigian, M.S., 2011. GHBM Mid-Size Male Model 2011 Status and Future Plan.

Toyota Motor Corporation, 2011. THUMS AM50 pedestrian/occupant model academic version 4.0.

Turkovich, M.J., 2010. The effects of obesity on occupant injury risk in frontal impact: a computer modeling approach. University of Pittsburgh.

van Rooij, L., van Hoof, J., McCann, M.J., Ridella, S.A., Rupp, J.D., Barbir, A., van der Made, R. and Slaats, P., 2004. A finite element lower extremity and pelvis model for predicting bone injuries due to knee bolster loading. *SAE International*.

Varellis, J., Campbell, J.Q. and Tannous, R.E., 2004. Development and validation of a finite element model of the THOR lower extremity. *SAE Technical Paper*.

Vavalle, N.A., Schoell, S.L., Weaver, A.A., Stitzel, J.D. and Gayzik, F.S., 2014. Application of radial basis function methods in the development of a 95th percentile male seated FEA model. *Proc. Stapp Car Crash Conference* 58, 361-384.

Veizin, P. and Verreist, J.P., 2005. Development of a set of numerical human models for safety. *Proc. International Technical Conference on the Enhanced Safety of Vehicles* 19.

Wang, S.C., Brede, C., Lange, D., Poster, G.S., Lange, A.W., Kohoyda-Inglis, C., Sochor, M.M., Ipaktchi, K. and Rowe, S.A., 2004. Gender differences in hip anatomy: possible implications for injury tolerance in frontal collisions. *Proc. Association for the Advancement of Automotive Medicine* 48, 287-301.

Weisstein, E.W., 2013. Singular value decomposition. From MathWorld--A Wolfram Web Resource. <http://mathworld.wolfram.com/SingularValueDecomposition.html>.

Yaeger, S. and Flores, D., 2013. Automotive consortium strives to make future vehicles safer by licensing free advanced human body model to universities. Detroit, MI.

Yoganandan, N.,M., Arun, W.J. and Pintar F.A., 2014. Normalizing and scaling of data to derive human response corridors from impact tests. *Journal of Biomechanics* 47, 1749-1756.